

Incoherent Short Pulse Scattering from Penetrable Geophysical Media

by

Robert John Adams

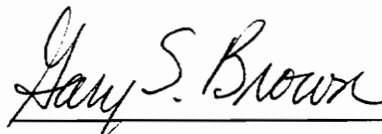
Thesis submitted to the Faculty of the Bradley Department of Electrical
Engineering at Virginia Polytechnic Institute and State University in partial
fulfillment of the requirements for the degree of

Master of Science

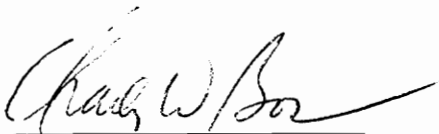
in

Electrical Engineering

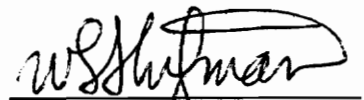
APPROVED:



Dr. G. S. Brown, Chairman



Dr. C. W. Bostian



Dr. W. L. Stutzman

LD
5655
V885
1995
A336
C.2

INCOHERENT SHORT PULSE SCATTERING FROM PENETRABLE GEOPHYSICAL MEDIA

by

Robert John Adams

Dr. Gary S. Brown, Chairman

Bradley Department of Electrical Engineering

(ABSTRACT)

A new model for incoherent short pulse scattering from penetrable geophysical media is developed. The model is obtained by assuming that the surface and volume scattered components of the total scattered waveform only minimally interact. A well-known form is used for the surface scattered component of the backscattered waveform while a new form is derived for the volume scattered component of the total scattered waveform.

The new volume scattered waveform model is derived from the scalar equation of transfer. This development illustrates the inherent assumptions of the new model as well as previous models. This leads to a reconciliation of parameter estimates obtained using short pulse scattering models and those obtained using other techniques. In addition, the new model represents a generalization of previous volume scattered waveform models in that it incorporates the effects on the average scattered waveform due to surface roughness and layering in the electromagnetic properties of the scattering medium. Previous models are shown to be slightly incorrect special cases of the new model. Finally, the volume scattered waveform model developed herein is demonstrated to be numerically efficient in general, providing a time savings factor of up to 500 relative to a previous model.

The scattered waveform model is subsequently used to analyze scattering data obtained over the Greenland ice sheet by the University of Massachusetts at Amherst's 13.5 GHz Advanced Aircraft Flight Experiment (AAFE) altimeter and NASA's 36 GHz Multimode Aircraft Radar Altimeter (MARA). These altimeters operated simultaneously from the same P-3 aircraft platform in September of 1991 and thus provide a dual frequency look at the scattering properties of the ice sheet. In addition, the large section of the ice sheet from which the scattering data is obtained provides an opportunity to

evaluate the radar altimeter's ability to distinguish between the various regions of the ice sheet. The results of this analysis suggest that the altimeter provides a useful means for monitoring both short and long term variations in the near surface region of the ice sheet while simultaneously providing precise estimates of the ice sheet elevation.

Acknowledgments

I would like to thank Dr. C. W. Bostian and Dr. W. L. Stutzman for their time spent serving on my committee.

I am indebted to my advisor Dr. G. S. Brown for his support, guidance and patience during my pursuit of the Master of Science Degree. I am thankful to Dr. Brown for providing me an opportunity to become a member of the ElectroMagnetic Interactions Laboratory (EMIL) in January of 1994 in spite of my limited knowledge in the area of electromagnetic fields. Your high standards and example of excellence are appreciated.

Special thanks to former EMIL member Dr. Michael H. Newkirk who is now with the Millimeter Wave Sensors Branch of the U. S. Army Research Laboratory in Adelphi, Maryland. His patience and guidance throughout the work discussed in this thesis were invaluable. This work would not have been possible without his help. In particular, I would like to point out that a large portion of the computer code used to compute the backscattered waveforms discussed in this report was written by Dr. Newkirk.

I would like to thank Doug Vandemark of the NASA Goddard Space Flight Center - Wallops Flight Facility. His patient assistance and advice in the manipulation of the MARA and AOL data sets analyzed in this thesis is greatly appreciated. Without his help the comparison of modeled and measured scattered waveforms would not have been possible.

Finally and most of all, I am grateful to my wife Mary. Your love and friendship are the greatest blessings in my life and your support of my continued education in spite of the sacrifices involved is deeply appreciated.

The work discussed in this thesis was supported by NASA under grant NAG5-659 and by the Office of Naval Research Electromagnetics and Sea Ice Initiative under grant N00014-93-1-0123.

Table of Contents

Abstract..... ii

Acknowledgments..... iv

Table of Contents..... v

List of Tables..... vii

List of Figures..... viii

1 Introduction and Literature Review..... 1

 1.1 Outline of Research..... 7

2 The Average Incoherent Scattered Waveform Model..... 9

 2.1 The Surface Scattered Waveform Model..... 10

 2.2 Previous Volume Scattered Waveform Models..... 14

 2.3 A New Volume Scattered Waveform Model..... 15

 2.3.1 The Equation of Transfer: A First-Order Solution..... 17

 2.3.2 Scattering from Vertically Distributed Media..... 23

 2.3.3 The Received Incoherent Waveform..... 26

 2.3.4 Scattering from Volumes with Homogeneous Statistics: A Comparison
 with Previous Models..... 31

 2.3.5 Capabilities and Limitations..... 43

 2.4 The Combined Incoherent Scattered Waveform Model..... 43

3 Analysis of Multifrequency Altimeter Data..... 45

 3.1 The Greenland Ice Sheet..... 46

 3.2 The Altimeter Systems..... 51

 3.3 Scattered Waveform Retracking..... 54

 3.4 Parameter Estimation..... 73

 3.4.1 Analysis of North- vs. South-Bound MARA Parameter Estimates..... 76

3.4.2 Analysis of Day-to-Day Variations in MARA Parameter Estimates..... 87

3.4.3 Two Frequency Comparison: MARA and AAFE..... 95

3.4.4 Parameter Estimation: Capabilities and Limitations..... 110

3.5 Range Estimate Performance..... 111

4 Conclusions..... 116

5 References..... 118

Appendix A: Scattering Model Assumptions..... 121

Vita..... 126

List of Tables

Table 2.1	CPU time ratio comparisons.....	39
Table 3.1	Comparison MARA and AAFE system parameters.....	52

List of Figures

Figure 2.1 Geometry used to derive the flat surface impulse response. “A” is the altimeter location and r_o is the antenna boresight axis. dA is the differential surface area. For the volume model, the differential surface area dA is replaced by the differential volume element dV 13

Figure 2.2 Cross section of the geometry used to develop average volume scattered waveform model..... 19

Figure 2.3 Volume scattered waveform model for the MARA system with $k_e = 0.20$ Np/m..... 34

Figure 2.4 Volume scattered waveform model for the MARA system with $k_e = 4.0$ Np/m..... 35

Figure 2.5 Volume scattered waveform model for the AAFE system with $k_e = 0.20$ Np/m..... 36

Figure 2.6 Volume scattered waveform model for the AAFE system with $k_e = 4.0$ Np/m..... 37

Figure 2.7 Difference in parameter estimates obtained using the original and new volume scattering models to analyze MARA data obtained on September 20, 1991..... 41

Figure 2.8 Parameter estimates for MARA data obtained on September 20, 1991 over the Greenland ice sheet..... 42

Figure 3.1 Illustration of the various diagenetic facies of the ice sheet..... 47

Figure 3.2 Map of Southern Greenland showing the flight line for the example data and the: (A) dry snow, (B) percolation, and (C) soaked and ablation regions.... 48

Figure 3.3 Relative peak power measured by the four beams of the MARA system on September 20, 1991..... 53

Figure 3.4 Elevation versus latitude and longitude along the flight line shown in Figure 3.2..... 55

Figure 3.5 Individual scattered MARA waveforms as tracked by the onboard tracker (a) and as they actually arrived at the altimeter (b). The corresponding range

	words for these pulses are all different in (a) and have been adjusted such that they are all equal in (b).....	56
Figure 3.6	Example of the effect of a pointing angle change on the average scattered MARA waveform. The range displacement has been removed so only the waveform shapes are compared.....	59
Figure 3.7	Model MARA waveforms for radar platform heights of 500 and 500.333 meters above the mean surface. The only difference is in the location of the waveform in the range window.....	60
Figure 3.8	Non-aligned and centroid aligned sub-averaged waveforms.....	63
Figure 3.9	Block diagram indicating waveform averaging procedure used for MARA data.....	64
Figure 3.10	rms surface roughness estimates obtained using various alignment techniques. The threshold aligned data were aligned at the half-power point on the leading edge of the sub-average waveforms.....	65
Figure 3.11	Extinction coefficient estimates obtained using various alignment techniques. The threshold aligned data were aligned at the half-power point on the leading edge of the sub-average waveforms.....	66
Figure 3.12	Volume/surface ratio estimates obtained using various alignment techniques. The threshold aligned data were aligned at the half-power point on the leading edge of the sub-average waveforms.....	67
Figure 3.13	rms roughness for centroid aligned sub-average waveforms. The sub-average waveforms were obtained using 10 and 20 individual MARA pulses. Respective groups of 10 and 5 of these sub-average waveforms were averaged to obtain the data points in these figures. Each point is thus the average of 100 raw waveforms.....	68
Figure 3.14	Extinction coefficient for centroid aligned sub-average waveforms. The sub-average waveforms were obtained using 10 and 20 individual MARA pulses. Respective groups of 10 and 5 of these sub-average waveforms were averaged to obtain the data points in these figures. Each point is thus the average of 100 raw waveforms.....	69

Figure 3.15	Volume/surface ratio for centroid aligned sub-average waveforms. The sub-average waveforms were obtained using 10 and 20 individual MARA pulses. Respective groups of 10 and 5 of these sub-average waveforms were averaged to obtain the data points in these figures. Each point is thus the average of 100 raw waveforms.....	70
Figure 3.16	The rms surface roughness vs. latitude on September 19, 1991.....	77
Figure 3.17	Extinction coefficient vs. latitude on September 19, 1991.....	78
Figure 3.18	Volume/Surface ratio vs. latitude on September 19, 1991.....	79
Figure 3.19	Fit-error vs. latitude on September 19, 1991.....	80
Figure 3.20	Examples of model fits to averaged MARA waveforms obtained from three different sections of the flight line shown in Figure 3.2.....	82
Figure 3.21	Average scattered waveforms recorded by MARA over the percolation zone. "Bumps" on the trailing edge indicate scattering from strong subsurface inhomogeneities.....	86
Figure 3.22	MARA rms surface roughness estimates on the north-bound leg of the flight line on September 18, 19 and 20, 1991.....	88
Figure 3.23	MARA extinction coefficient estimates on the north-bound leg of the flight line on September 18, 19 and 20, 1991.....	89
Figure 3.24	MARA volume/surface ratio estimates on the north-bound leg of the flight line on September 18, 19 and 20, 1991.....	90
Figure 3.25	MARA fit-error on the north-bound leg of the flight line on September 18, 19 and 20, 1991.....	91
Figure 3.26	Modeled surface and volume waveforms. As the extinction coefficient becomes larger the surface and volume scattered waveforms become more similar.....	93
Figure 3.27	Comparison of best-fit model waveforms on September 18 and September 20.....	94

Figure 3.28 Comparison of average scattered waveforms. These waveforms were obtained by averaging all data from 67.7°–69° on each of the three days considered.....	96
Figure 3.29 Parameter estimates for data obtained by the AAFE system on September 18, 1991 over the Greenland ice sheet.....	97
Figure 3.30 Comparison of rms surface roughness estimates derived from data obtained by the MARA and AAFE altimeters on September 18, 1991.....	98
Figure 3.31 Comparison of extinction coefficient estimates derived from data obtained by the MARA and AAFE altimeters on September 18, 1991.....	99
Figure 3.32 Comparison of volume/surface ratio estimates derived from data obtained by the MARA and AAFE altimeters on September 18, 1991.....	100
Figure 3.33 Comparison of fit-error values obtained by fitting the composite scattering model to data obtained by the MARA and AAFE altimeters on September 18, 1991.....	101
Figure 3.34 Averaged MARA and AAFE waveforms at 71.43°. The effect of strong subsurface scatterers is clear in the AAFE waveform but is not apparent in the MARA waveform.....	103
Figure 3.35 Peak power observed along the flight line for the MARA and AAFE altimeters.....	106
Figure 3.36 AAFE scattered waveforms from 70.16°–70.74°.....	108
Figure 3.37 Difference between MARA and AOL elevation estimates ($z_{MARA} - z_{AOL}$) along the flight line on September 20, 1991.....	115
Figure A.1 Those scattering effects which are included in the new model discussed in this report are indicated by solid lines (the small circular scatterers are assumed to be close to one another on the scale of a pulsewidth). An illustration of the type of long range scattering not included in the new model is indicated by the dashed line.....	124

Chapter 1

Introduction and Literature Review

Radar altimetry was first suggested as a technique for remote sensing the topography and sea state of the world's oceans from space in the mid 1960's [9]. The utility of the short-pulse altimeter as a space-borne remote sensing tool was demonstrated in the early 1970's aboard NASA's manned Skylab mission. Although only capable of determining the mean sea level to within $\pm 1-2$ m, the Skylab experiment served as a proof-of-concept mission and demonstrated the ability of altimeters to measure various oceanographic characteristics including rms wave height and wind speed [20]. More recently the Topex altimeter has performed remarkably, achieving elevation measurements with a 2 cm precision and accuracy over a calm sea from a mean orbital altitude of 1334 km [19].

The success of the altimeter in monitoring the world's oceans is well documented. This success, as well as the availability of archived altimeter data¹, has led to the recent development of techniques for studying altimeter data measured over the Greenland and Antarctic ice sheets [10,26]. Just as the development of satellite-based altimetry techniques in the early 1970's was largely driven by the need for accurate, large scale data on the earth's oceans, application of altimetry techniques to the ice sheets has been similarly driven by the need for large scale data in order to obtain a better understanding of the role of the ice sheets in the world's climate. There is enough water stored in the Greenland and Antarctic ice sheets to raise the world's sea level by 70 meters. Thus, a small change in the quantity of water stored in these glaciers would be significant. For example, it is postulated that the collapse of the west antarctic ice shelf during the last ice age was responsible for raising the world-wide sea level six meters during that period. Global climate models predict that evidence of global climatic variations will first be evident in the polar ice sheets [28].

¹The orbital latitudinal range of the Seasat ($\pm 72^\circ$), GEOS-3 ($\pm 65^\circ$) and Geosat ($\pm 72^\circ$) satellites have provided altimeter data over significant regions of the arctic and antarctic ice sheets.

Although other remote sensing tools have been used to monitor these regions, altimeters provide a unique method for observing the ice sheets. Unlike other microwave instruments (such as scatterometers, radiometers and synthetic aperture radars) which rely on variations in pointing angle, frequency and/or polarization to determine the near surface properties of the ice sheets, the altimeter provides such information by transmitting a short pulse and recording the time dependent backscattered waveform. Using a knowledge of the scattering physics involved it is possible to determine the subsurface properties of the ice sheet from the variation of the average backscattered waveform with time. The time dependent form of the mean incoherent scattered waveform also provides the altimeter with the ability to directly measure the relative contributions of surface and volume scattering effects [26]. This information is not easily obtained from other remote sensing instruments. Furthermore, the ability of the radar altimeter to provide precise range-to-surface estimates over the ice sheets under all weather conditions is unmatched by other sensors.

Precise elevation estimates obtained by altimeter systems over the world's oceans typically exceed the pulsewidth-limited resolution of the respective altimeters. This is accomplished in part by using a variant of the Brown surface scattering model [5] to properly interpolate between points on the mean scattered waveform in determining which point on the waveform corresponds to the mean scattering surface. In addition to using a knowledge of the scattering physics to provide accurate ranging information, the scattering model is also used to extract information on the physical characteristics of the sea surface from the average incoherent backscattered waveform.

Unlike the fairly well understood case of scattering from the sea surface, electromagnetic scattering from the ice sheets is complicated by several factors. Foremost among these is that microwave radiation can significantly penetrate the ice sheets. This gives rise to surface *and* volume scattering contributions to the average backscattered waveform. In addition, the relative contributions of the surface and volume components of the total scattered waveform vary significantly with location across the ice sheets. This is in contrast to the case of scattering from the sea surface where volume scattering effects are negligible.

For these reasons, direct application of surface scattering models used over the electromagnetically impenetrable ocean to the problem of analyzing altimeter returns obtained over the ice sheets can result in elevation errors on the order of several meters [26]. However, the need to monitor the earth's environment requires that altitude changes on the order of ± 0.1 meter-per-year be measurable in the arctic and antarctic regions [28].

To this end, several authors have investigated the development of more appropriate short-pulse scattering models by including the effects of volume scattering on the average scattered waveform. In addition to providing more precise and repeatable elevation estimates, these models also provide important information on the geophysical and electromagnetic properties of the ice sheets. This additional information can be useful in monitoring spatially and temporally variable geophysical processes that are manifested in the near-surface region of the ice pack. These models are also applicable to sea ice although there is usually much less volume scattering contribution.

The first short-pulse scattering model to incorporate the effect of volume scattering on the backscattered waveform was developed by *Ridley and Partington* [26]. This model is an approximation to the actual volume scattering process and is derived using a simplified energy balance technique. Short-pulse volume scattering models developed by subsequent authors for altimeter applications are essentially simplifications or extensions of this model. In this and subsequent incoherent models, the average incoherent scattered power waveform $\langle P(t) \rangle$ is assumed to consist of the sum of an average surface scattered component and an average volume scattered component,

$$\langle P(t) \rangle = \langle S(t) \rangle + \langle V(t) \rangle \quad (1-1)$$

where $\langle S(t) \rangle$ and $\langle V(t) \rangle$ are the components of $\langle P(t) \rangle$ due to surface and volume scattering effects, respectively. The form used for the average surface scattered waveform in (1-1) is the well known Brown model [5]. Thus, the primary effort in developing a model which can be applied to altimeter returns obtained over penetrable geophysical media such as the ice sheets lies in determining an appropriate form for the average volume scattered power waveform $\langle V(t) \rangle$.

In addition to assuming that the volume scattering effects can be determined independent of the surface scattering effects as indicated by (1-1), *Ridley and Partington* model the volume scattered waveform as arising from the scattering of a rectangularly shaped incident pulse by a semi-infinite homogeneous distribution of small scatterers bounded by a flat interface. In this model the volume scattering process is characterized by two parameters. The first of these is the extinction coefficient (k_e) which accounts for absorption and scattering losses experienced by the incident pulse as it propagates within the scattering volume. The second parameter is the backscattering cross section per-unit-volume (σ_b). This parameter is used to determine how much energy is scattered back toward the radar from each point in the scattering volume. Using this model to analyze

data recorded by the Seasat altimeter over the Antarctic ice sheet, *Ridley and Partington* have demonstrated that penetration depths in excess of eight meters occur over regions of the Antarctic ice sheet. *Ridley and Partington* have also shown that elevation estimates derived by applying only the surface scattering model to altimeter data sets obtained over the ice sheets can result in elevation errors of up to 3.3 meters. This result represents the first quantitative evidence that volume scattering effects can significantly affect altimeter derived elevation estimates of the ice sheets.

The volume scattered component $\langle V(t) \rangle$ of the backscattered waveform model developed by *Ridley and Partington* requires the numerical evaluation of an integral over the scattering volume. The model also uses the unrealistic assumption of a rectangular transmitted pulse shape. Using the same fundamental scattering assumptions as *Ridley and Partington*, *Davis and Moore* [10] removed both of these limitations. Using a Gaussian form for the transmitted pulse envelope and making simplifying assumptions appropriate for nadir-directed spaceborne radar altimetry applications, *Davis and Moore* derived a closed form analytical expression for the volume scattered waveform as a function of time. Combining this result with the closed form surface scattering model as suggested by equation (1-1), a closed form expression was obtained for the total average scattered waveform model. *Davis* [11] demonstrated the improved modeling capabilities of the two component model relative to the surface scattered model alone by evaluating the models' ability to retrack altimeter waveforms obtained over the Greenland and Antarctic ice sheets.

Davis and Zwally [12] subsequently used this closed form expression for the combined surface and volume scattering model to analyze altimeter returns obtained over the Antarctic and Greenland ice sheets by the Seasat and Geosat altimeters. The electromagnetic parameter estimates derived by fitting the model to the measured data were shown to be strongly correlated with known seasonal and geographical variations in the ice sheet properties. Penetration depths ranging from 2.1 to 10 meters were obtained from satellite-borne altimeter data obtained over the Greenland and Antarctic ice sheets. These values are similar to those previously determined by *Ridley and Partington* [26] for the Antarctic ice sheet. These estimates were also corroborated by measurements of the penetration depth made by *Davis and Poznyak* [13] using a surface based 10 GHz pulsed radar system in East Antarctica.

By applying the closed form expression for the combined surface and volume model to ice sheet returns previously analyzed using only a surface scattering model, *Davis* [14] has

demonstrated that average annual growth rate estimates for the Greenland ice sheet determined using only the surface scattering model overestimated the actual growth rate of the glacier by 64 percent. The original estimate of the average annual growth rate for the ice sheet derived from altimeter data using the surface scattering model was determined by *Zwally* to be $+0.23$ m/year [35]. The revised estimate obtained by *Davis* using the combined surface and volume scattering model was $+0.14$ m/year.

Ferraro [15] used the aircraft based, pulsewidth limited Advanced Aircraft Flight Experiment (AAFE) altimeter to study the effect of volume scattering on the average backscattered waveform obtained over the Greenland ice sheet. Using 13.5 GHz data obtained from an altimeter operating at approximately the same frequency as the Seasat and Geosat altimeters (13.9 GHz) from an altitude of less than 1 km, *Ferraro* demonstrated the effects of subsurface inhomogeneities on backscattered waveforms for a pulsewidth-limited altimeter. It was shown that the assumption of a homogeneous volume of scatterers made in deriving the previous scattering models is not valid for significant regions of the Greenland ice sheet. *Ferraro* also put forth the first attempt to model altimeter waveforms scattered from the strongly inhomogeneous percolation region of the ice sheet where the homogeneous scattering models developed by *Ridley and Partington* and *Davis and Moore* are not valid. This was accomplished by modifying the scattering model to incorporate the effects of variations in the subsurface density and particle-size distribution determined from localized *in situ* measurements of the ice sheet. Although reasonable results were obtained for the single example presented by *Ferraro*, the technique used to include the nonhomogeneous scattering effects requires significant computational time for evaluation.

The volume scattered waveform models developed by *Ridley and Partington* and *Davis and Moore* are only valid for nadir-directed satellite borne altimeter applications. *Newkirk* [22] formally extended these models to account for the scattering observed by an arbitrarily pointed radar altimeter system. The scattering model developed by *Newkirk* incorporates the effects of off-nadir pointing angles, a nonsymmetric antenna power pattern, beamwidth limited operation, an arbitrary platform height above the mean scattering surface and an arbitrary transmitted pulse envelope. Combining this volume scattered waveform model with a similarly developed surface scattering model [21], *Newkirk* analyzed data recorded by NASA's Multimode Airborne Radar Altimeter (MARA) which operated over the Greenland ice sheet in the summer of 1991. By fitting the model to recorded waveforms, *Newkirk* identified latitudinal variations in the 36 GHz electromagnetic properties of the ice sheet. The observed variations were found to be

qualitatively similar to those determined using the 13.9 GHz Seasat and Geosat altimeter data sets [12] and the 13.5 GHz AAFE data set [15].

Finally, an alternative volume scattered waveform model has been developed by *LeVine, et. al.* [18]. Unlike the volume scattering models discussed above which are somewhat heuristic in their development, this model is derived directly from the scalar wave equation. However, several simplifying approximations are made in its development. Foremost among these is a sparse medium assumption which precludes the application of the model to scattering data obtained from media such as snow and ice where multiple scattering effects are important. For this reason this approach to modeling the volume scattering process is not pursued here.

The research discussed in this document represents an extension of the work done by others using a scattering model of the type represented by equation (1-1) to study scattering from arbitrary geophysical terrain. While much work has already been done in this area, the models discussed above leave significant room for additional work. For example, the assumptions inherent in these models are not readily apparent from their development. This leads to uncertainties in the meaning of the parameters contained in these models. In particular, it is not clear what the extinction coefficient included in these models actually means and how it is related to values of the extinction coefficient determined by others using different remote sensing techniques.

The models discussed above are also restricted in that they assume that the scattering medium can be modeled as a *homogeneous* distribution of scatterers bounded by a *flat* interface. Both of these assumptions are nonphysical representations of the actual scattering problem. The assumption of a flat interface between free-space and the scattering medium causes these scattering models to approach an incorrect limit as the volume scattering process becomes limited to regions near the rough interface (i.e., when the penetration depth becomes small). In addition, the assumption of a homogeneously distributed volume of small scatterers has been demonstrated to be invalid over significant regions of the Greenland ice sheet [15]. The homogeneous scattering medium assumption also precludes the direct application of these scattering models to other media such as foliage and sea ice which are known to exhibit layering in their physical structures. A model which incorporates these effects would provide a useful tool for monitoring and identifying these types of media.

Finally, the only model currently available which can be used to analyze data obtained from narrow-beam altimeters operating at aircraft altitudes is the model developed by

Newkirk [22]. In using this model to analyze scattering data obtained over the Greenland ice sheet, it has been found that in some cases the model takes a significant amount of CPU time to evaluate. Thus, for a new scattering model to be practically useful it must also be numerically inexpensive to evaluate.

In an effort to address these problems a significant part of the research discussed in this report is directed towards the development of an improved volume scattering model. In addition to developing such a model, it is also necessary to evaluate the usefulness of the model. This is accomplished here in two ways. First, the new model is compared to previously developed scattered waveform models. The model is also evaluated by using it to analyze a significant amount of scattering data obtained in 1991 over the Greenland ice sheet. In addition to providing an assessment of the scattering model, this process also provides useful information on the near-surface properties of the ice sheet as well as an initial assessment of the ability of the airborne radar altimeter to monitor the world's ice sheets.

1.1 Outline of Research

The work discussed herein is divided into four chapters. Chapter 1 consists of the preceding introduction and literature review and the current outline.

Chapter 2 of this document discusses the development of a new volume scattered waveform model from the scalar equation of transfer. The new scattering model is subsequently compared to previous models and the impact of the new model on parameter estimates derived from altimeter data obtained over the Greenland ice sheet is presented. A two-component model capable of modeling scattering over regions where surface and volume scattering effects are both significant is obtained by combining the new volume scattered waveform model with a previously developed surface scattering model.

Chapter 3 of this document presents a comparison of parameter estimates derived using the newly developed scattering model to analyze two altimeter data sets obtained over the Greenland ice sheet. The scattering data analyzed have been obtained from archives of data recorded by the 13.5 GHz pulsewidth-limited AAFE altimeter and the 36 GHz beamwidth-limited MARA altimeter which operated simultaneously from the same aircraft platform in September of 1991. The two-frequency nature of this data set provides a unique opportunity to evaluate both altimeter systems as well as the two component scattering model. In this chapter, the process used to average raw scattered waveforms recorded by the MARA altimeter is presented and the "brute force" fitting

scheme used to obtain parameter estimates from the average backscattered waveforms is discussed. The parameter estimates derived using this technique for the two different frequency altimeters are analyzed and compared. The altimeter systems' ability to identify the various facies of the ice sheet is also evaluated. Finally, the ability of the altimeter systems to precisely measure the range-to-surface is evaluated through an intercomparison of the two radar systems with a laser profilometer which operated simultaneously with the radars over the ice sheet.

Chapter 4 details the conclusions of this research effort. Potential areas for future work are also identified in this section.

Chapter 2

The Average Incoherent Scattered Waveform Model

An appropriate scattering model is required to extract useful information from altimeter returns obtained over geophysical media. The model must incorporate the effects of the radar system, the radar platform, and the scattering medium on the scattered waveform. The relevant radar system parameters include the operating frequency of the radar, the transmitted pulse amplitude and shape, the antenna's radiation pattern, and the antenna's pointing angle relative to the radar platform. The important radar platform parameters are the height of the platform above the mean scattering surface and its angular orientation relative to the mean scattering surface (the Doppler shift due to the radar platform's velocity is neglected).

The relevant parameters used to define the scattering medium depend on the type of model used. The waveform model considered in this report was given in equation (1-1) and is repeated here for convenience,

$$\langle P(t) \rangle = \langle S(t) \rangle + \langle V(t) \rangle \quad (2-1)$$

In this equation, $\langle P(t) \rangle$ is the average incoherent scattered power waveform measured by the altimeter. $\langle S(t) \rangle$ is the average surface scattered waveform and $\langle V(t) \rangle$ is the average volume scattered waveform.

The decomposition of the average incoherent scattered power waveform $\langle P(t) \rangle$ into surface and volume components is motivated by both physical and analytical considerations. It is well-known that the surface and volume scattered components of $\langle P(t) \rangle$ are intimately related through the boundary conditions at the free-space/scattering-medium interface. However, for the work considered here, the surface and volume scattered components of the total waveform are assumed to be related only through the power reflection and transmission coefficients of the interface.

This decomposition of the average scattered waveform into surface and volume scattered components provides a significant analytical simplification in developing the average scattered waveform model. Since a well-known form for the average surface scattered model $\langle S(t) \rangle$ is available [21], it is only necessary to determine an appropriate form for $\langle V(t) \rangle$ to obtain the total scattered waveform. The development of a new form for $\langle V(t) \rangle$ comprises one of the principle objectives of this research. Before proceeding with this development, however, a brief review of the surface scattered waveform model will be presented.

2.1 The Surface Scattered Waveform Model

The surface scattered waveform model is theoretically based on the quasi-specular scattering model which was rigorously formulated in the 1960's. Using a stationary phase technique to evaluate the surface integral for the field scattered from a randomly rough surface obtained using the Kirchhoff approximation, *Kodis* [17] demonstrated that the scattered field in the high frequency limit is the sum of the field scattered from all specular points on the surface. Provided that the surface is sufficiently rough and that the illuminated region of the surface is sufficiently large so that a large number of specular points are illuminated, the mean scattered field is zero. However, ignoring antenna beamwidth effects, the backscattered power in this case is directly proportional to the illuminated surface area.

This linear variation in the backscattered power with the illuminated surface area is used directly in radar altimetry applications to develop the surface scattering model. Assuming that there are a sufficiently large number of specular scattering facets (independent of the illumination area) *Brown* [7] allows the summation developed by *Kodis* to approach an integral. This integral defines the surface scattered waveform averaged over the surface slopes, $\langle S(t) \rangle$, as

$$\langle S(t) \rangle = \frac{\lambda_o^2}{(4\pi)^3} \int_{S_r} \frac{P_t(t - \frac{2r}{c_o}) G^2(\theta, \phi)}{r^4} \sigma^o(x, y) dA \quad (2-2)$$

In this equation, S_r is the illuminated rough surface, $P_t(t)$ is the point target response of the radar as a function of time t , $G(\theta, \phi)$ is the one-way normalized antenna power pattern, $\sigma^o(x, y)$ is the scattering cross section per-unit-area on the rough surface at the point (x, y) , r is the distance from the altimeter to a specular scattering facet and c_o is the speed of light in air.

Assuming that the surface height and slope are independent random variables, and that the specular point probability density function (pdf) is symmetric about the mean scattering surface, the average surface scattered waveform is obtained from (2-2) as a convolution of three terms [7]

$$\langle S(t) \rangle = P_t(t) \otimes p_{sp}(\zeta) \otimes P_{FS}(t) \quad (2-3)$$

where \otimes denotes a convolution. The convolution is simply defined as

$$h(t) = f(t) \otimes g(t) = \int_{-\infty}^{\infty} f(\tau)g(t - \tau)d\tau \quad (2-4)$$

The convolution of multiple terms is obtained through the repeated application of this definition.

In equation (2-3) p_{sp} is the specular point pdf of the rough surface, ζ is the height of the specular point on the rough surface above the mean flat surface, and P_{FS} is the flat surface impulse response. P_{FS} contains all the effects on the average backscattered waveform due to radar system parameters, pointing angle, height, and variation of the backscattered cross section with incidence angle. In applying the model represented by (2-3) it is often further assumed that the specular point pdf and the surface height pdf are equivalent. In this case the specular point pdf p_{sp} can be replaced by the height pdf p_ζ .

For an arbitrary altimeter system, the flat surface impulse response P_{FS} in (2-3) has the form

$$P_{FS}(t) = \frac{\lambda_o^2}{(4\pi)^3} \int_{S_f} \frac{\delta(t - \frac{2r}{c_o})}{r^4} G^2(\theta, \phi) \sigma^o(\theta, \phi) dA \quad (2-5)$$

where $\delta(t)$ is the Dirac delta-function and S_f is the mean flat surface illuminated by the radar. The evaluation of this surface integral represents the primary computational limit in evaluating the surface scattered waveform model (the convolutions in (2-3) can be rapidly evaluated using the fast-Fourier-transform technique [21]). To remove this limitation *Brown* [5] developed a closed form for P_{FS} valid for nadir-directed satellite applications by assuming σ^o to be approximately constant over the illuminated area and assuming a symmetric Gaussian form for $G(\theta, \phi)$. Assuming Gaussian forms for the point target response P_t and the specular point pdf p_{sp} , *Brown* also presented a closed form result for

the average surface scattered waveform $\langle S(t) \rangle$. This closed form expression for the average surface scattered waveform model is widely used in radar altimetry applications.

Recently the technique of multiple-beam radar altimetry has been proposed for use in measuring large scale, time varying phenomena on the surface of the ocean which are not measurable by nadir-directed altimeter systems [24]. Due to the use of beamwidth rather than pulsewidth limited operation, the closed form for the flat surface impulse response P_{FS} developed by *Brown* is not valid and has been reconsidered. A new form of the flat surface impulse response has been developed by *Newkirk and Brown* [21]. This form of the flat surface impulse response is valid for an arbitrary pointing angle and includes the effects of an asymmetric antenna pattern on the surface scattered waveform. The analytical form of P_{FS} for an arbitrary altimeter platform is [21]

$$P_{FS}(\tau) = \frac{4G_o^2\lambda^2 c_o \sigma^o(\theta)}{(4\pi)^3 (c_o \tau + 2h)^3} \int_0^{2\pi} \exp \left\{ -\frac{4}{\gamma} \left[1 + \frac{\beta \rho^2 \sin^2 \phi}{\rho^2 - 2\rho \rho_o \cos \phi + \rho_o^2} \right] \right. \\ \left. \cdot \left[1 - \frac{(\cos \xi + \epsilon \sin \xi \cos \phi)^2}{1 + \epsilon^2} \right] \right\} d\phi, \quad \tau \geq 0, \quad (2-6)$$

where h is the height of the altimeter above the mean scattering surface and

$$\epsilon = \sqrt{c_o \tau / h}, \quad \rho = \sqrt{c_o \tau h}, \quad \rho_o = h \tan \xi \quad (2-7)$$

In these equations, $\tau = t - 2h/c_o$. The relationships between these variables are illustrated in Figure 2.1. The parameters γ and β are related to the antenna beamwidth through [21]

$$\gamma = \frac{2\sin^2(\theta_s/2)}{\ln 2} \quad (2-8)$$

$$\beta = \frac{\gamma \ln 2}{2\sin^2(\theta_{xs}/2)} - 1 \quad (2-9)$$

The parameters θ_s and θ_{xs} are the scan and cross-scan beamwidths which can be thought of as the E- and H-plane beamwidths of the antenna [21]. When the two beamwidths are identical β reduces to zero.

For the work presented in this report, equation (2-6) is used to evaluate the flat surface impulse response. The various asymptotic approximations which reduce the time

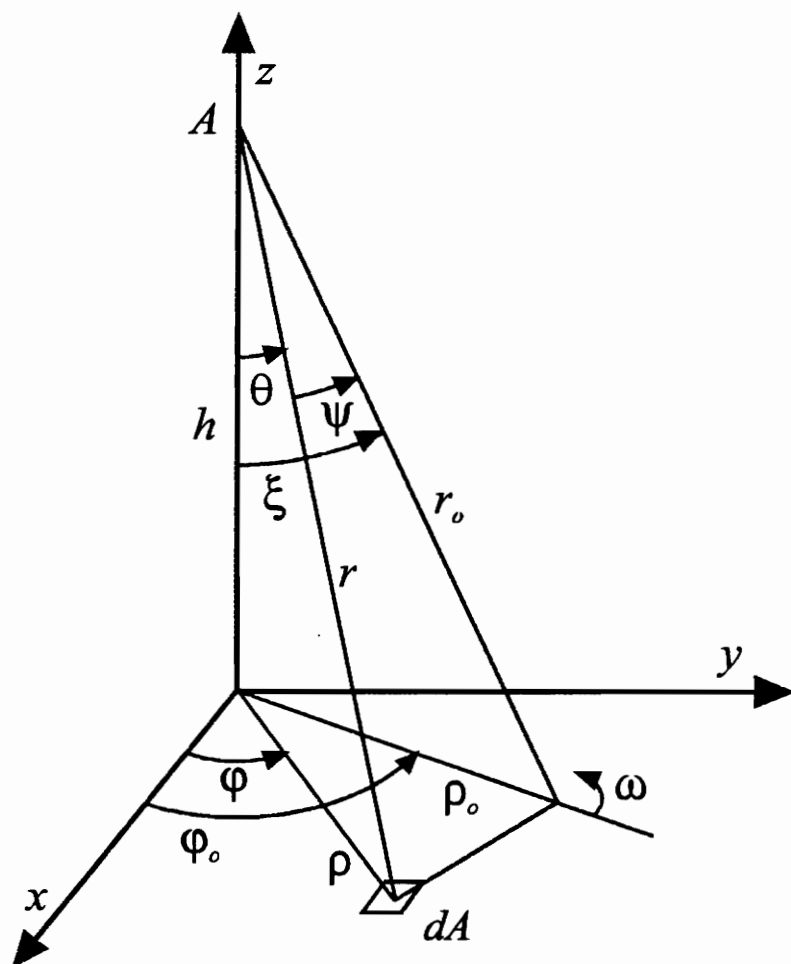


Figure 2.1. Geometry used to derive the surface and volume scattered impulse responses. “A” is the altimeter location and r_o is the antenna boresight axis. dA is the differential surface area. For the volume model, the differential surface area dA is replaced by the differential volume element dV . From [22].

required to evaluate this integral are also used for the work discussed herein [21]. The effects of the point target response and surface height pdf on the scattered waveform are incorporated by using a fast-Fourier-transform technique to perform numerically the convolutions in (2-3). Examples of surface scattered waveforms evaluated using the above model can be found in [21] and [22].

2.2 Previous Volume Scattered Waveform Models

Having a model for evaluating the surface scattered waveform, it is now necessary to determine an appropriate form for the average volume scattered waveform $\langle V(t) \rangle$ in equation (2-1). Several authors have developed volume scattered waveform models of the type required [26, 10, 22]. As mentioned in Chapter 1, while these models have been used to analyze altimeter data obtained over the world's ice sheets with varying degrees of success, there remains much room for improvement. In order to provide a basis for the development of a new scattering model of the type required by equation (2-1), a brief review of the average volume scattered waveform model developed by *Newkirk* [22] will be presented. This model is used as a point of comparison because other models ([10, 26]) are special cases of it.

The starting point used to develop the volume scattered waveform model is a generalized form of the radar equation. In a time-dependent differential form this equation is written

$$dV(t) = \frac{\lambda_o^2}{(4\pi)^3} \frac{P_t(t - t_o)G^2(\theta, \phi)}{r^4} \sigma_b e^{-2k_e \delta} dv \quad (2-10)$$

where $dV(t)$ is the differential power scattered back to the transceiver from the differential volume element dv , P_t is the transmitted pulse envelope, t_o is an appropriate delay time, σ_b is the backscattering cross section per-unit-volume at a point in the scattering medium, k_e is the effective extinction coefficient of the medium and δ is the one-way propagation distance within the scattering medium to the differential volume element dv (the medium is assumed to be homogeneously distributed).

While this expression can be explicitly integrated to determine the scattered waveform model, advantage is taken of the fact that the process represented by (2-10) is linear and

time invariant². This allows the scattered waveform $V(t)$ to be written as the convolution of the transmitted pulse envelope $P_t(t)$ with the volume scattered impulse response $V_{IR}(t)$. With \otimes denoting the convolutional operator, this result is symbolically expressed as

$$V(t) = P_t(t) \otimes V_{IR}(t) \quad (2-11)$$

The primary advantage to writing the volume scattered waveform in this form is that, in determining V_{IR} , P_t in equation (2-10) can be replaced by a delta-function. This allows the integrated form of (2-10) to be written in terms of an integral over the surface illuminated by the incident delta-function pulse rather than the volume integral required for the case of a finite-width incident pulse. Inserting a delta function into (2-10), assuming that the free-space/scattering-medium interface is planar, and integrating out the radial dependence, the volume scattered impulse response in spherical coordinates has the form [22]

$$V_{IR}(\tau) = \frac{2G_o^2 \lambda^2 \sigma_b c_s}{(4\pi)^3 (c_s \tau + 2h)^2} \int_0^{\theta_u} T_b^2(\theta) \sin\theta \exp\{-k_e[c_s \tau - 2hc_r(\sec\theta - 1)]\} \\ \cdot \int_0^{2\pi} \exp\left\{-\frac{4}{\gamma} \left[1 + \beta \left(\frac{\tan^2\theta \sin^2\phi}{\tan^2\xi - 2\tan\xi \tan\theta \cos\phi + \tan^2\theta}\right)\right]\right\} \\ \cdot [1 - \cos^2\xi \cos^2\theta [1 + \tan\xi \tan\theta \cos\phi]^2] d\phi d\theta, \quad \tau \geq 0, \quad (2-12)$$

where

$T_b(\theta)$	Fresnel power transmission coefficient of the scattering medium
σ_b	backscattering cross section per-unit-volume
k_e	effective extinction coefficient of the medium
c_s	speed of light in medium
c_r	relative speed of light within the medium = c_s/c_o .

Also, $\theta_u = \cos^{-1}\left(\frac{1}{c_o\tau/2h+1}\right)$ and the remaining parameters are defined in (2-7) through (2-9). Figure 2.1 provides the geometry associated with equation (2-12). This equation represents the scattering from the portion of the volume medium illuminated by a spherical shell of vanishingly small thickness. Only that part of the shell in the scattering medium will produce backscattered energy.

²It is assumed that σ_b and k_e do not vary over the bandwidth of the transmitted pulse and can be replaced by their value at $f_o = c_o/\lambda_o$.

Notice that although the radial dependence has been integrated out, equation (2-12) for the volume scattered impulse response still requires the evaluation of a two-dimensional integral. It has been found that the numerical evaluation of this integral can require a significant amount of CPU time. This restricts the usefulness of the general form of the volume scattering model in analyzing realistic data sets. This restriction is removed in the following section where it will be shown that the volume scattered impulse response V_{IR} can in general be decomposed into the convolution of three independent terms.

2.3 A New Volume Scattered Waveform Model

Equations (2-11) and (2-12) of the previous section represent the generalized form of the volume scattered waveform model as used by previous authors. Although various forms of this model have been developed by several authors, all of these models include specific restrictions which limit the types of realistic problems to which they can be applied. For example, previous waveform models assume that the interface between free-space and the scattering volume is flat. This causes these models to approach an incorrect limit as the volume scattering process becomes confined to regions very near the rough free-space/scattering-medium interface (i.e., when the penetration depth of the scattering medium is small).

In addition, these models assume that the volume distribution of scatterers is homogeneous. *Ferraro* [15] and *Newkirk* [22] have demonstrated that this assumption is invalid over a significant portion of the Greenland ice sheet using two significantly different altimeter systems. It is also expected that the homogeneous assumption inherent in these models precludes their application to other geophysical media (such as foliage or sea ice) which are characterized by a nonhomogeneous distribution of scatterers.

Furthermore, unlike the surface scattered waveform model which is based on the well understood quasi-specular model for rough surface scattering, it is not entirely clear what assumptions have been made in developing these volume scattered waveform models from the generalized radar equation (c.f. (2-10)). This leads to confusion regarding the meaning of the parameters in the scattering models and how they are related to similar parameters derived using other techniques. Finally, the only model valid for off-nadir and aircraft based applications is the generalized scattering model developed by *Newkirk* [22]. It has been found that this model is in general computationally expensive to evaluate. This limits the model's utility in analyzing realistic data sets.

In an effort to resolve these issues, a newly developed volume scattered waveform model will be presented. The new scattering model is derived from the well-known scalar equation of transfer. This process leads to several important results. First, we discover the approximations inherent to the current and previous volume scattering models which have not been presented in the literature. This leads to a reconciliation of altimeter derived estimates of the scattering properties of dry snow and those determined using other techniques.

In addition, it is determined that the effects of surface roughness and a vertical variation in the mean scattering properties of the random medium on the scattered waveform can be incorporated in a numerically efficient manner. The flat interface, homogeneous scattering models of previous authors are found to be somewhat incorrect special cases of the new model. Finally, the new model is valid for a general altimeter platform and is significantly faster than the similarly valid model developed by *Newkirk* [22]. In some instances the relative computational savings of the new volume scattered waveform model approach a factor of 500.

2.3.1 The Equation of Transfer: A First-Order Solution

The new volume scattered waveform model is derived by assuming that the volume scattering process is incoherent. That is, we assume that the field scattered back to the receiver from a small volume element is statistically independent of the field scattered by neighboring volume elements. This allows us to neglect the phase of the reflected field and add power levels in determining the scattered waveform. Furthermore, we also assume that the scattering within the volume itself is an incoherent process which is insensitive to polarization so that the scalar equation of transfer applies [30],

$$dI(\hat{r}; r, \theta, \phi, t) = [-k_e(r, \theta, \phi)I(\hat{r}; r, \theta, \phi, t) + J_a(\hat{r}; r, \theta, \phi, t) + J_s(\hat{r}; r, \theta, \phi, t)]ds \quad (2-13)$$

where

$$J_s(\hat{r}; r, \theta, \phi, t) = \frac{k_s(r, \theta, \phi)}{4\pi} \int \int_{4\pi} \psi(\hat{r}, \hat{r}_i; r, \theta, \phi, t) I(\hat{r}_i; r, \theta, \phi, t) d\Omega_i \quad (2-14)$$

$$k_e(r, \theta, \phi) = k_a(r, \theta, \phi) + k_s(r, \theta, \phi) \quad (2-15)$$

In these equations

$I(\hat{r}; r, \theta, \phi, t)$	intensity scattered in the \hat{r} -direction at the point (r, θ, ϕ) and time t ,
$J_a(\hat{r}; r, \theta, \phi, t)$	absorption source term; the intensity re-radiated into the \hat{r} -direction due to the physical temperature at the point (r, θ, ϕ) and time t ,
$J_s(\hat{r}; r, \theta, \phi, t)$	scattering source term; the intensity scattered from all directions into the \hat{r} -direction at the point (r, θ, ϕ) and time t ,
$\psi(\hat{r}, \hat{r}_i)$	scattering phase function; determines the amount of energy scattered from the \hat{r}_i -direction into the \hat{r} -direction,
$k_a(r, \theta, \phi)$	absorption cross section per-unit-volume,
$k_s(r, \theta, \phi)$	scattering cross section per-unit-volume,
$k_e(r, \theta, \phi)$	extinction cross section per-unit-volume,
ds	differential path length.

A cross section of the problem geometry is shown in Figure 2.2. The geometry indicated in this figure will be used in the following development of the volume scattered waveform model.

Equation (2-13) is usually written without the indicated time dependence and used to analyze steady-state scattering problems. However, it is assumed that the bandwidth of the transmitted pulse is small compared to the carrier frequency so that the equation of transfer can be written with the indicated time dependence. In addition, equation (2-13) is only valid for the propagation of plane waves in random media. To analyze spherical waves, an additional term which accounts for losses incurred due to the spreading of the pulse front must be included. In this case (2-13) becomes

$$dI(\hat{r}; r, \theta, \phi, t) = [-k_e(r, \theta, \phi)I(\hat{r}; r, \theta, \phi, t) + J_a(\hat{r}; r, \theta, \phi, t) + J_s(\hat{r}; r, \theta, \phi, t) - \frac{2}{r}I(\hat{r}; r, \theta, \phi, t)] ds \quad (2-16)$$

where we have assumed that the mean spherical nature of the incident pulse is not significantly distorted in the transmission across the rough interface. In practice, this spreading loss will be minimal due to the small penetration depth of the scattering medium.

Although we have significantly simplified the scattering problem by assuming that the scalar equation of transfer applies, equation (2-16) is still not easily solved and must be manipulated into a more usable form. To this end, (2-16) is solved in three steps. The *downwelling* intensity (i.e., the component of I in the $+\hat{r}$ -direction) will first be determined by assuming that the downwelling component is not coupled to the *upwelling* component (the $-\hat{r}$ -directed part of I). Having determined $I(+\hat{r})$ in this manner, it will then be used as a part of the scattering source term in the equation of transfer to determine the first-order upwelling intensity. Finally, by integrating and averaging the upwelling

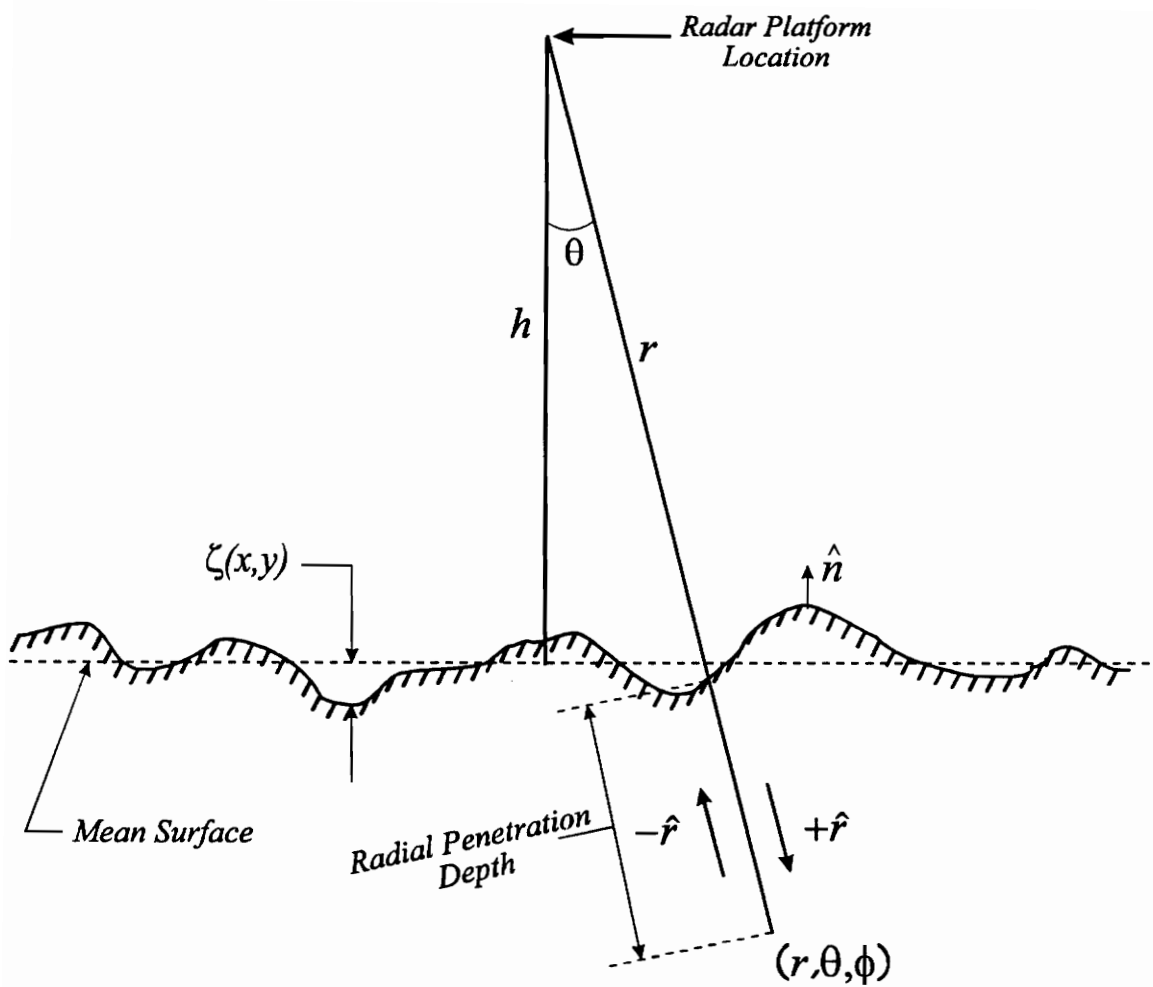


Figure 2.2. Cross section of the geometry used to develop average volume scattered waveform model.

intensity over the rough interface, the received power will be determined as a function of time.

The downwelling intensity

We begin by considering the downwelling intensity $I(+\hat{r}; r, \theta, \phi, t)$. To solve equation (2-13) we must determine the scattering source term $J_s(+\hat{r}; r, \theta, \phi, t)$. As indicated in (2-14), J_s is typically a complicated function of position and direction which defines the coupling between propagation directions at a point in the medium. For the present application a simplified form of this equation will be used. Assuming that long range scattering effects can be neglected, J_s can be approximated as,

$$J_s(\hat{r}; r, \theta, \phi, t) \approx \sigma_f(r, \theta, \phi) I(\hat{r}; r, \theta, \phi, t). \quad (2-17)$$

where σ_f is the *effective forward scattering cross section per-unit-volume*. The assumptions inherent to this approximation for both sparse and dense media are discussed in Appendix A.

Using (2-17) in (2-16) and neglecting the absorption source term³, we have

$$\begin{aligned} dI(\hat{r}; r, \theta, \phi, t) &= \left[-k_e(r, \theta, \phi) + \sigma_f(r, \theta, \phi) - \frac{2}{r} \right] I(\hat{r}; r, \theta, \phi, t) dr \\ &\equiv \left[-\tilde{k}_e(r, \theta, \phi) - \frac{2}{r} \right] I(\hat{r}; r, \theta, \phi, t) dr \end{aligned} \quad (2-18)$$

where \tilde{k}_e is called the *effective extinction coefficient* and differs from k_e in that it includes the effective forward scattering cross section. This distinction is important to remember in comparing parameter estimates obtained using the current model with those derived using other techniques.

The initial condition for the differential equation (2-18) occurs at the interface $r = (h - \zeta)\sec\theta$,

$$I(\hat{r}; (h - \zeta)\sec\theta, \theta, \phi, t) = I_o\left(t - \frac{(h - \zeta)\sec\theta}{c_o}\right) \quad (2-19)$$

where $I_o(t)$ is the incident intensity and $\zeta(x, y)$ is the random surface height at the point where the incident ray intersects the rough interface. Integrating (2-18) along the radial

³ $J_s \gg J_a$ here. J_a is only important for passive remote sensing applications where the only contribution to I is from thermal effects.

direction and applying (2-19), the downwelling intensity at a radial distance r into the medium is

$$\begin{aligned}
 I(\hat{r}; r, \theta, \phi, t) &= I_o \left[t - \int_{(h-\zeta)\sec\theta}^r \frac{d\chi}{c_s(\chi, \theta, \phi)} - \frac{(h-\zeta)\sec\theta}{c_o} \right] \\
 &\cdot \exp \left\{ - \int_0^r \tilde{k}_e(\chi, \theta, \phi) d\chi \right\} \frac{[(h-\zeta)\sec\theta]^2}{r^2} \\
 &\approx I_o \left[t - \int_{(h-\zeta)\sec\theta}^r \frac{d\chi}{c_s(\chi, \theta, \phi)} - \frac{(h-\zeta)\sec\theta}{c_o} \right] \exp \left\{ - \int_0^r \tilde{k}_e(\chi, \theta, \phi) d\chi \right\}
 \end{aligned} \tag{2-20}$$

where it has been assumed that the penetration depth in the scattering medium is small compared to the distance to the radar,

$$\frac{[(h-\zeta)\sec\theta]^2}{r^2} \approx 1 \tag{2-21}$$

In (2-20) c_o is the speed of light in free space and $c_s(r, \theta, \phi)$ is the variable speed of light within the scattering volume. The integral in the argument of I_o determines the time of propagation along the radial direction from the rough surface to a point in the scattering volume.

Upwelling Intensity

The appropriate equation of transfer for the upwelling intensity is

$$dI(\hat{r}; r, \theta, \phi, t) = [k_e(r, \theta, \phi)I(\hat{r}; r, \theta, \phi, t) - J_s(-\hat{r}; r, \theta, \phi, t)] dr \tag{2-22}$$

where spherical spreading losses have been neglected. There is a sign change in (2-22) relative to (2-16) because dr is negative here and $ds = |dr| = -dr$.

We proceed to solve (2-22) as before by first obtaining an approximation for the scattering source term J_s in the upwelling direction. In addition to the effective forward scattering contribution given by (2-17), there is another contribution to the upwelling intensity due to the backscattered downwelling intensity

$$J_s(-\hat{r}; r, \theta, \phi, t) \approx \sigma_f(r, \theta, \phi)I(-\hat{r}; r, \theta, \phi, t) + \sigma_b(r, \theta, \phi)I(\hat{r}; r, \theta, \phi, t) \tag{2-23}$$

where σ_b is the *effective backscattering cross section per-unit-volume*. Appendix A contains a discussion of the assumptions inherent to this approximation for both sparse and dense media.

Using this approximation the equation of transfer for the first-order upwelling intensity becomes

$$dI(-\hat{r}; r, \theta, \phi, t) = \left[\tilde{k}_e(r, \theta, \phi) I(-\hat{r}; r, \theta, \phi, t) - \sigma_b(r, \theta, \phi) I(\hat{r}; r, \theta, \phi, t) \right] dr \quad (2-24)$$

where the downwelling intensity now serves as the source term for the upwelling intensity. Multiplying by the appropriate integrating factor and imposing the condition of no sources below the interface, the upwelling intensity at a point in the volume is

$$\begin{aligned} I(-\hat{r}; r, \theta, \phi, t) = & \exp \left\{ \int_{(h-\zeta)\sec\theta}^r \tilde{k}_e(\chi, \theta, \phi) d\chi \right\} \\ & \cdot \int_{(h-\zeta)\sec\theta}^{\infty} \left[\sigma_b(\alpha, \theta, \phi) \exp \left\{ - \int_{(h-\zeta)\sec\theta}^{\alpha} 2\tilde{k}_e(\chi, \theta, \phi) d\chi \right\} \right. \\ & \cdot \left. I_o \left(t - \int_{(h-\zeta)\sec\theta}^{\alpha} c_s^{-1}(\chi, \theta, \phi) d\chi - \int_r^{\alpha} c_s^{-1}(\chi, \theta, \phi) d\chi - \frac{(h-\zeta)\sec\theta}{c_o} \right) \right] d\alpha. \end{aligned} \quad (2-25)$$

The desired upwelling intensity at the surface is obtained by evaluating (2-25) at $r = (h - \zeta)\sec\theta$,

$$\begin{aligned} I(-\hat{r}; r, \theta, \phi, t) = & \int_{-\infty}^{\infty} E(\alpha, \theta, \phi) \\ & \cdot I_o \left(t - \int_{(h-\zeta)\sec\theta}^{\alpha} 2c_s^{-1}(\chi, \theta, \phi) d\chi - \frac{(h-\zeta)\sec\theta}{c_o} \right) d\alpha, \end{aligned} \quad (2-26)$$

where the new function $E(r, \theta, \phi)$ is defined by

$$E(r, \theta, \phi) = \sigma_b(r, \theta, \phi) \exp \left\{ - \int_{(h-\zeta)\sec\theta}^r 2\tilde{k}_e(\chi, \theta, \phi) d\chi \right\} u(r - (h - \zeta)\sec\theta) \quad (2-27)$$

and $u(\cdot)$ is the unit-step or Heaviside function.

Equation (2-26) is the general result for the first-order upwelling intensity scattered by a random volume bounded by a rough interface. The validity of this expression depends on the validity of the assumptions from which it was derived. In particular, the assumed forms for the scattering source terms in (2-17) and (2-23) require that there are no significant wide angle scattering effects in the volume (see Appendix A). In the case of vertically distributed media discussed below, this also implies that the effects of multiple scattering between layers on the upwelling intensity can be neglected. When this assumption is not valid, it is possible to use the current development to include additional scattering effects.

2.3.2 Scattering from Vertically Distributed Media

Equations (2-26) and (2-27) express the average upwelling intensity in terms of integrals over the scattering volume. To be useful in analyzing measured data, it is necessary to recast these equations in a more numerically efficient form. It will be shown that for volumes in which the scattering parameters are functions only of the depth of penetration along the radius from the altimeter to a point in the medium, the average scattered waveform can be expressed in terms of a series of convolutions. This expression can then be quickly evaluated using the fast-Fourier-transform technique. When this medium is illuminated by a narrow beam radar, it will also be shown that this convolutional model is valid for the more physically realistic problem of scattering from vertically distributed media.

Radially Distributed Media

We begin by assuming that the effective extinction and scattering coefficients, as well as the velocity of propagation within the medium, are functions only of the depth of penetration along the radius from the altimeter to a point in the scattering volume,

$$\begin{aligned}
\tilde{k}_e(r, \theta, \phi) &= \tilde{k}_e(r - (h - \zeta)\sec\theta) \\
\sigma_b(r, \theta, \phi) &= \sigma_b(r - (h - \zeta)\sec\theta) \\
c_s(r, \theta, \phi) &= c_s(r - (h - \zeta)\sec\theta)
\end{aligned} \tag{2-28}$$

This radial depth of penetration is illustrated in Figure 2.2. In this case, equation (2-26) can be written

$$\begin{aligned}
I(-\hat{r}; (h - \zeta)\sec\theta, t) &= \int_{-\infty}^{\infty} E(\alpha - (h - \zeta)\sec\theta) \\
&\cdot I_o\left(t - g(\alpha - (h - \zeta)\sec\theta) - \frac{(h - \zeta)\sec\theta}{c_o}\right) d\alpha, \tag{2-29}
\end{aligned}$$

where

$$g(r - (h - \zeta)\sec\theta) \equiv 2 \int_0^{r - (h - \zeta)\sec\theta} c_s^{-1}(\chi) d\chi \tag{2-30}$$

and two appropriate changes of variables have been made to obtain (2-29) from equations (2-26) and (2-27). The new function g determines the round-trip propagation time from the surface to a point in the volume.

In a realistic problem, the function $g(x)$ will be a continuous and monotonically increasing function of x (since c_s will be non-zero and positive at all points in the volume). Thus, the inverse function g^{-1} exists. Using g^{-1} , (2-29) can be rewritten

$$\begin{aligned}
I(-\hat{r}; (h - \zeta)\sec\theta, t) &= \int_{-\infty}^{\infty} E(g^{-1}(g(\alpha - (h - \zeta)\sec\theta))) \\
&\cdot I_o\left(t - g(\alpha - (h - \zeta)\sec\theta) - \frac{(h - \zeta)\sec\theta}{c_o}\right) d\alpha, \tag{2-31}
\end{aligned}$$

which is a non-linear convolution. Performing the change of variables

$$\begin{aligned}
z &= g(\alpha - (h - \zeta)\sec\theta) \\
dz &= g'(\alpha - (h - \zeta)\sec\theta) d\alpha \\
&= g'(g^{-1}(z)) dz
\end{aligned} \tag{2-32}$$

equation (2-31) becomes

$$\begin{aligned}
I(-\hat{r}; (h - \zeta)\sec\theta, t) &= \int_{-\infty}^{\infty} \frac{E(g^{-1}(z))}{g'(g^{-1}(z))} I_o\left(t - z - \frac{(h - \zeta)\sec\theta}{c_o}\right) dz \\
&\equiv \widetilde{E}\left(t - \frac{(h - \zeta)\sec\theta}{c_o}\right) \otimes I_o\left(t - \frac{(h - \zeta)\sec\theta}{c_o}\right),
\end{aligned} \tag{2-33}$$

where the symbol \otimes denotes a convolution and the function \widetilde{E} is defined by the relation

$$\widetilde{E}(x) \equiv \frac{E(g^{-1}(x))}{g'(x)} \tag{2-34}$$

The ability to actually obtain an explicit form for \widetilde{E} will depend on the functional dependence of c_s .

Vertically Distributed Media

In deriving the convolutional form for the upwelling intensity, (2-33), it was assumed that the parameters defining the scattering from the random volume were a function only of the depth of penetration along the radius from the altimeter to a point in the scattering volume (cf. (2-28) and Figure 2.2). In general, this is not a realistic approximation since geophysical media are not distributed in this manner. A more realistic functional dependence for these parameters is a dependence on the vertical depth below the rough interface.

Provided that the illuminating radar has a sufficiently narrow beamwidth, the approximation

$$\cos\theta \approx \cos\theta_o \tag{2-35}$$

can be made where θ is the local elevation angle and θ_o is the elevation angle along the antenna boresight. Because of the small beamwidth of the antenna, contributions to the backscattered intensity from angles where this approximation is not good will be small. Using this approximation in equation (2-28) the functional dependence of the scattering medium parameters can be written as

$$\begin{aligned}
\widetilde{k}_e(r, \theta, \phi) &= \widetilde{k}_e(r - (h - \zeta)\sec\theta) \approx \widetilde{k}_e((\cos\theta_o)^{-1}(r\cos\theta - (h - \zeta))) \\
\sigma_b(r, \theta, \phi) &= \sigma_b(r - (h - \zeta)\sec\theta) \approx \sigma_b((\cos\theta_o)^{-1}(r\cos\theta - (h - \zeta))) \\
c_s(r, \theta, \phi) &= c_s(r - (h - \zeta)\sec\theta) \approx c_s((\cos\theta_o)^{-1}(r\cos\theta - (h - \zeta)))
\end{aligned} \tag{2-36}$$

where the argument $(\cos\theta_o)^{-1}(r\cos\theta - (h - \zeta))$ represents the vertical distance below the

rough interface. Assuming this functional dependence for the medium scattering parameters, a convolutional model will be developed in Section 2.3.3.

The determination of how narrow the antenna beamwidth must be for (2-36) to be satisfied depends on the actual variation in these scattering parameters with depth below the interface. For a medium in which these parameters vary rapidly with depth, small errors in the approximation

$$r - (h - \zeta)\sec\theta \approx (\cos\theta_o)^{-1}(r\cos\theta - (h - \zeta)) \quad (2-37)$$

will lead to large errors in the approximation (2-36). To reduce these errors a very narrow beamwidth antenna must be used. Conversely, in the case of a homogeneous medium, the scattering parameters are independent of location within the volume and an arbitrarily wide beamwidth antenna may be chosen (provided that the other assumptions of the model are also satisfied).

2.3.3 The Received Incoherent Waveform

Now that an expression for the average, first-order upwelling intensity at the rough free-space/scattering-medium interface is available, it is necessary to integrate and average this expression over the rough interface to obtain the received waveform. To this end, we first express the transmitted intensity just below the interface, I_o , in terms of the pulse transmitted by the radar, $P_t(t)$. In the high frequency limit, ignoring refraction and shadowing effects, I_o is determined as

$$I_o(t) = - \frac{P_t(t) T(\theta) G(\theta, \phi)}{4\pi r^2} \hat{r} \cdot \hat{n}, \quad (2-38)$$

$$\hat{n} = \frac{-\zeta_x \hat{x} - \zeta_y \hat{y} + \hat{z}}{\sqrt{\zeta_x^2 + \zeta_y^2 + 1}}$$

where

$T(\theta)$	Fresnel power transmission coefficient for an angle of incidence θ (the effects of local surface slopes have been neglected),
$G(\theta, \phi)$	Transceiver antenna's unnormalized power pattern pointed in the direction (θ_o, ϕ_o) ,
\hat{n}	upward directed unit-vector perpendicular to the scattering volume interface,
\hat{r}	radial unit-vector pointing from the transceiver to the point of incidence on the rough surface,
ζ_x, ζ_y	surface slopes in the \hat{x} - and \hat{y} -directions.

In (2-38), the dot product term is introduced to account for the spreading of the incident spherical wavefront as it intersects the non-spherical surface. Substituting (2-38) in (2-33), the average upwelling intensity on the rough interface at time t is

$$I(-\hat{r}; (h - \zeta)\sec\theta, t) = \tilde{E} \left(t - \frac{(h - \zeta)\sec\theta}{c_o} \right) \otimes P_t \left(t - \frac{(h - \zeta)\sec\theta}{c_o} \right) \cdot \frac{T(\theta) G(\theta, \phi)}{4\pi r^2} \hat{r} \cdot \hat{n} \quad (2-39)$$

The received waveform is obtained by integrating this radially directed intensity, delayed by the time of propagation from the surface to the receiver, over the rough interface

$$V(t) = \frac{\lambda^2}{(4\pi)^2} \int_{S_r} \frac{T(\theta) G(\theta, \phi)}{r^2} I \left(-\hat{r}; (h - \zeta)\sec\theta, t - \frac{(h - \zeta)\sec\theta}{c_o} \right) dS, \quad (2-40)$$

where it has been assumed that P_t has infinite support in time so that the integral (2-40) can be performed over the entire rough interface S_r . Using the identity ([27], p. 1039)

$$dS = \frac{|\nabla\zeta|}{|\nabla\zeta \cdot \hat{z}|} dA = |-\zeta_x \hat{x} - \zeta_y \hat{y} + \hat{z}| dA \quad (2-41)$$

where dA is the differential surface element on the planar surface perpendicular to \hat{z} , equation (2-40) can be converted to an integral over the mean flat surface S_f

$$V(t) = \frac{\lambda^2}{(4\pi)^2} \int_{S_f} \frac{T(\theta) G(\theta, \phi)}{r^2} I \left(-\hat{r}; (h - \zeta)\sec\theta, t - \frac{(h - \zeta)\sec\theta}{c_o} \right) |-\zeta_x \hat{x} - \zeta_y \hat{y} + \hat{z}| dA \quad (2-42)$$

Using (2-39) in (2-42), the received waveform is finally

$$V(t) = \frac{\lambda^2}{(4\pi)^3} \int_{S_f} \frac{T^2(\theta) G^2(\theta, \phi)}{r^4} \tilde{E} \left(t - \frac{2(h - \zeta)\sec\theta}{c_o} \right) \otimes P_t \left(t - \frac{2(h - \zeta)\sec\theta}{c_o} \right) \hat{r} \cdot (-\zeta_x \hat{x} - \zeta_y \hat{y} + \hat{z}) dA \quad (2-43)$$

Equation (2-43) is an expression for the random received power conditioned on the random surface variables ζ , ζ_x and ζ_y . The average volume scattered waveform is obtained by averaging over these random surface quantities. By averaging (2-43) in this

manner it will be shown that the average volume scattered waveform can be expressed as a convolution of the function \tilde{E} with a scaled form of the surface scattered waveform model defined in equation (2-3) of Section 2.1.

Averaging (2-43) over a rough surface [7]

Assuming that the surface slopes ζ_x and ζ_y are zero-mean random variables which are independent of the random surface height ζ , the average of (2-43) with respect to the surface slopes is

$$\begin{aligned} \langle V(t) \rangle_{\nabla\zeta} &= \frac{\lambda^2}{(4\pi)^3} \int_{S_f} \tilde{E} \left(t - \frac{2(h-\zeta)\sec\theta}{c_o} \right) \otimes P_t \left(t - \frac{2(h-\zeta)\sec\theta}{c_o} \right) \\ &\quad \cdot \frac{T^2(\theta) G^2(\theta, \phi)}{r^4} \cos\theta dA \end{aligned} \quad (2-44)$$

where $\hat{r} \cdot \hat{z} = \cos\theta$ was used. Averaging this with respect to the random variable ζ and assuming $r \approx h\sec\theta$ in the denominator we have

$$\begin{aligned} \langle V(t) \rangle_{\nabla\zeta, \zeta} &= \frac{\lambda^2}{h^4(4\pi)^3} \int_{S_f} \int_{-\infty}^{\infty} \tilde{E} \left(t - \frac{2(h-\zeta)\sec\theta}{c_o} \right) \otimes P_t \left(t - \frac{2(h-\zeta)\sec\theta}{c_o} \right) \\ &\quad \cdot p_\zeta(\zeta) d\zeta T^2(\theta) G^2(\theta, \phi) \cos^5\theta dA \end{aligned} \quad (2-45)$$

where p_ζ is the surface height probability density function (pdf) and the order of the integrations has been interchanged.

The inner integral of (2-45) is a θ -dependent convolution; however, for radar altimetry applications, the beamwidth of the antenna is usually less than a few degrees. This allows the approximation $\sec\theta \approx \sec\theta_o$ to be made in (2-45). The ζ -integral is then a negative convolution (i.e., a correlation) which is independent of the other variables in the problem. Assuming the height pdf is symmetric about the mean surface we have

$$\begin{aligned} \langle V(t) \rangle_{\nabla\zeta, \zeta} &= \frac{\lambda^2}{h^4(4\pi)^3} \int_{S_f} \tilde{E} \left(t - \frac{2h\sec\theta}{c_o} \right) \otimes P_t \left(t - \frac{2h\sec\theta}{c_o} \right) \\ &\quad \otimes \tilde{p}_\zeta \left(t - \frac{2h\sec\theta}{c_o} \right) T^2(\theta) G^2(\theta, \phi) \cos^5\theta dA, \end{aligned} \quad (2-46)$$

where the new function \tilde{p}_ζ is related to the corresponding function of (2-45) through the relation

$$\tilde{p}_\zeta(t) = \frac{c_o}{2\sec\theta_o} p_\zeta\left(\frac{c_o t}{2\sec\theta_o}\right) \quad (2-47)$$

Expressing the differential surface element of (2-46) in cylindrical coordinates and making the change of variables $rdr = \rho d\rho$, $r = h\sec\theta$ gives

$$\begin{aligned} \langle V(t) \rangle_{\nabla\zeta,\zeta} &= \frac{\lambda^2}{(4\pi)^3} \int_{S_f} \tilde{E}\left(t - \frac{2r}{c_o}\right) \otimes P_t\left(t - \frac{2r}{c_o}\right) \\ &\quad \otimes \tilde{p}_\zeta\left(t - \frac{2r}{c_o}\right) T^2(\theta) G^2(\theta, \phi) \frac{h}{r^4} dr d\phi \end{aligned} \quad (2-48)$$

Using the sifting property of the Dirac delta-function, equation (2-48) is equivalently expressed

$$\begin{aligned} \langle V(t) \rangle_{\nabla\zeta,\zeta} &= \frac{\lambda^2}{(4\pi)^3} \int \int_{-\infty}^{\infty} \tilde{E}(t - \chi) \otimes P_t(t - \chi) \otimes \tilde{p}_\zeta(t - \chi) \\ &\quad \cdot \delta\left(\chi - \frac{2r}{c_o}\right) d\chi T^2(\theta) G^2(\theta, \phi) \frac{h}{r^4} dr d\phi \end{aligned} \quad (2-49)$$

Interchanging the order of the integrations and recognizing the χ -integral of equation (2-49) to be another convolution integral we have finally

$$\langle V(t) \rangle = P_t(t) \otimes P_{FS}(t) \otimes \tilde{p}_\zeta(t) \otimes \tilde{E}(t) \quad (2-50)$$

where the function P_{FS} is called the *flat surface impulse response* (FSIR) and is defined here as

$$P_{FS}(t) = \frac{\lambda^2}{(4\pi)^3} \int_{S_f} \delta\left(t - \frac{2r}{c_o}\right) T^2(\theta) G^2(\theta, \phi) \frac{h}{r^4} dr d\phi. \quad (2-51)$$

We can demonstrate that this expression for the FSIR is similar to the forms of this function which have appeared in the literature ([5,21]) by transforming back to cylindrical coordinates using the substitution

$$\begin{aligned} r &= \sqrt{\rho^2 + h^2} \\ dr &= \frac{\rho d\rho}{\sqrt{\rho^2 + h^2}} \end{aligned} \quad (2-52)$$

in equation (2-51). This yields

$$P_{FS}(t) = \frac{\lambda^2}{(4\pi)^3} \int_{S_f} \delta\left(t - \frac{2r}{c_o}\right) \frac{T^2(\theta) G^2(\theta, \phi)}{r^4} \cos \theta dA \quad (2-53)$$

This expression for the flat surface impulse response differs from the flat surface impulse response used by previous authors ([5,21]) in that an additional $\cos \theta$ term appears inside the integral. This additional factor has arisen in the current development because we have included the effects of the spreading of the incident spherical pulse as it intersects the rough interface. For near-nadir applications this correction is minor. For narrow beamwidth radars, the additional factor essentially scales the received power (relative to previous models) by the cosine of the incidence angle.

An additional difference between the above expression for the FSIR and that used by others [5,21] is that the average backscattering cross section of the surface is replaced by the square of the Fresnel transmission coefficient of the free-space/scattering-medium interface. Since the beamwidths of altimeter systems are typically very small, both the backscattering cross section and the transmission coefficient are constant over the region of integration and can be moved outside the integral operator. Thus this difference only results in a constant difference between the current expression for P_{FS} and that used for the surface model.

Replacing the tilde-functions in (2-50) by the corresponding original functions we have the final result,

$$\begin{aligned} V(t) &= P_t(t) \otimes P_{FS}(t) \otimes \frac{c_o p_\zeta\left(\frac{c_o t}{2 \sec \theta_o}\right)}{2 \sec \theta_o} \otimes \frac{E(g^{-1}(t))}{g'(t)} \\ &\equiv \hat{S}(t) \otimes \frac{E(g^{-1}(t))}{g'(t)} \end{aligned} \quad (2-54)$$

where \hat{S} is a scaled version of the surface model and it has been assumed that the specular point pdf and the height pdf are equivalent at the level of the approximation of the current model. The angular brackets indicating an average process have been dropped in (2-54) and it is understood that this model is an average waveform model.

The arguments for all of the functions in equation (2-54) is the time t elapsed since the transmission of the incident pulse. The functions P_t , p_ζ and E occur near $t = 0$. The delay due to propagation to and from the mean scattering surface is accounted for in the FSIR, P_{FS} . This can be seen from equation (2-53) where the argument of the delta-function is delayed by $2r/c_o$.

Except for the additional $\cos \theta$ factor in the integral for the FSIR, $\hat{S}(t)$ in (2-54) has exactly the same functional form as the average surface scattered waveform model $S(t)$ discussed in Section 2.1. As discussed above, the only difference in these functions for a narrow beamwidth radar systems is that, in the case of the surface model, $S(t)$ is scaled in amplitude by the backscattering cross section of the surface instead of the square of the transmission coefficient. The analogous backscattering cross section per-unit-volume of the scattering medium is included in (2-54) through the function E .

2.3.4 Scattering from Volumes with Homogeneous Statistics: A Comparison with Previous Models

Having developed a new model for the average incoherent volume scattered waveform, it is now necessary to validate the model. Such a validation can be partially obtained through a comparison with the previously developed volume scattered waveform model presented in Section 2.2 of this report [22]. This model has been chosen as a point of comparison because other comparable short pulse scattering models [10, 26] represent special cases of the more general model discussed in Section 2.2.

As mentioned previously, the volume scattered waveform model of [22] assumes that the interface between free space and the scattering medium is flat and that the statistics of the scattering volume are homogeneous. This leads to an average volume scattered waveform model of the form (2-11) which is repeated here for convenience,

$$V(\tau) = V_{IR}(\tau) \otimes P_t(\tau) \quad (2-11)$$

where the impulse response V_{IR} has been defined in equation (2-12). Imposing these same assumptions (i.e., a flat interface and a homogeneously distributed scattering volume) on the newly developed scattering model requires the following forms for the functions p_ζ and E in equation (2-54)

$$\begin{aligned} p_\zeta\left(\frac{c_o t}{2 \sec \theta_o}\right) &\Rightarrow \delta\left(\frac{c_o t}{2 \sec \theta_o}\right) \\ \frac{E(g^{-1}(t))}{g'(t)} &\Rightarrow \frac{c_s \sigma_b}{2} \exp(-k_e c_s t) u(t) \end{aligned} \quad (2-55)$$

Thus, for scattering from a half space of homogeneously distributed scatterers bounded by a flat interface, the new model has the functional form

$$\langle V(t) \rangle = P_t(t) \otimes P_{FS}(t) \otimes \left\{ \frac{c_s \sigma_b}{2} \exp(-k_e c_s t) u(t) \right\} \quad (2-56)$$

That this is the same form for the average volume scattered waveform as that derived by

Newkirk [22] is demonstrated by explicitly writing out the convolution of the last two terms in this expression,

$$P_{FS}(t) \otimes \left\{ \frac{c_s \sigma_b}{2} \exp(-k_e c_s t) \right\} = \frac{c_s \sigma_b}{2} \int_{-\infty}^{\infty} P_{FS}(t - \tau) e^{-k_e c_s \tau} u(\tau) d\tau \quad (2-57)$$

Inserting equation (2-53) for P_{FS} into this equation and interchanging the orders of the integrations produces

$$P_{FS}(t) \otimes \left\{ \frac{c_s \sigma_b}{2} \exp(-k_e c_s t) \right\} = \frac{c_s \sigma_b \lambda^2}{2(4\pi)^3} \int_{S_f} \int_{-\infty}^{\infty} \delta\left(t - \tau - \frac{2r}{c_o}\right) \cdot e^{-k_e c_s \tau} u(\tau) d\tau \frac{T^2(\theta) G^2(\theta, \phi)}{r^4} \cos \theta dA \quad (2-58)$$

Upon making the substitution

$$\tau = \frac{2(r - r_i)}{c_s}, \quad d\tau = \frac{2}{c_s} dr \quad (2-59)$$

equation (2-58) becomes

$$P_{FS}(t) \otimes \left\{ \frac{c_s \sigma_b}{2} \exp(-k_e c_s t) \right\} = \frac{\sigma_b \lambda^2}{(4\pi)^3} \int_{V_f} \delta\left(t - \frac{2r}{c_o} - \frac{2(r - r_i)}{c_s}\right) \cdot e^{-2k_e(r - r_i)} u(r - r_i) \frac{T^2(\theta) G^2(\theta, \phi)}{r^4} \cos \theta dV \quad (2-60)$$

where r_i is the distance from the radar to the flat free-space/scattering-medium interface ($r_i = h \sec \theta$). Also notice that the differential $d\tau$ has been combined with the differential surface area dA in (2-60) to form the differential volume element dV .

Except for the additional $\cos \theta$ term in the integrand, equation (2-60) is identical to the equation for the volume scattered impulse response (VSIR) presented in [22]. Thus, comparing equations (2-11) and (2-56) of this report we see that the flat, homogeneous volume scattered impulse response V_{IR} developed in [22] can be represented as a convolution of the flat surface impulse response with a decaying exponential,

$$V_{IR}(t) = P_{FS}(t) \otimes \left\{ \frac{c_s \sigma_b}{2} \exp(-k_e c_s t) \right\} \quad (2-61)$$

As discussed below, this decomposition of the volume scattered impulse response into two terms provides a significant computational savings in computing the average volume scattered waveform model.

Waveform Shape

The effects of a randomly rough interface on the volume scattered waveform can be obtained by convolving (2-61) with the height pdf p_ζ . Figures 2.3-2.6 demonstrate the effect of this additional term relative to the flat-interface volume scattering model represented by equation (2-11) for two different radar platforms⁴. The radar system parameters used in Figures 2.3 and 2.4 correspond to the MARA altimeter system discussed in [22]. The system parameters used in Figures 2.5 and 2.6 are for the AAFE altimeter system discussed in [15]. Table 3.1 lists the important system parameters for these two altimeters. These altimeter systems are, respectively, beamwidth- and pulsewidth-limited systems and thus demonstrate the result of including rough interface effects in the volume scattering model for two significantly different systems.

As demonstrated in these figures, when the extinction coefficient is small (Figures 2.3 and 2.5, $k_e = 0.2$ Np/meter) the effect of including the roughness in the volume scattering model is not significant. However, as the effective scattering volume becomes confined to regions nearer the rough interface, the effect of the rough interface on the volume scattered waveform becomes more significant. This is demonstrated for an extinction coefficient of $k_e = 4.0$ Np/meter in Figures 2.4 and 2.6 for the MARA and AAFE systems, respectively. Including the surface roughness effectively spreads the volume scattering response out in time relative to the flat interface model. This is to be expected since the rough interface model is just the convolution of the flat interface model with the surface height pdf.

Computational Speed

One of the most important aspects of any scattering model is its ability to aid in the extraction of useful information from measured data. Since such analyses are generally performed using digital computers, it is important that a scattering model be computationally efficient. In analyzing short-pulse scattering from satellite altitudes,

⁴A Gaussian pdf with standard deviation σ_h has been used to calculate these and all other waveforms in this report.

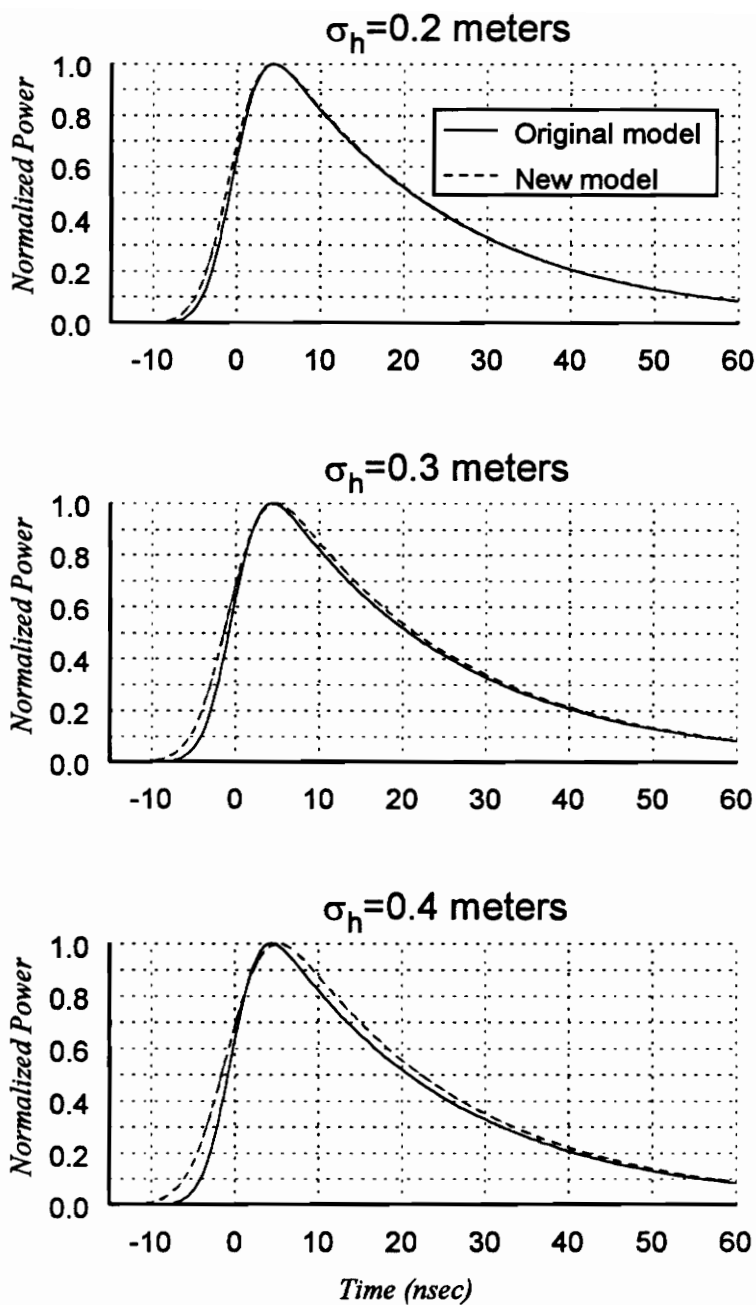


Figure 2.3. Volume scattered waveform model for the MARA system with $k_e = 0.20$ Np/m.

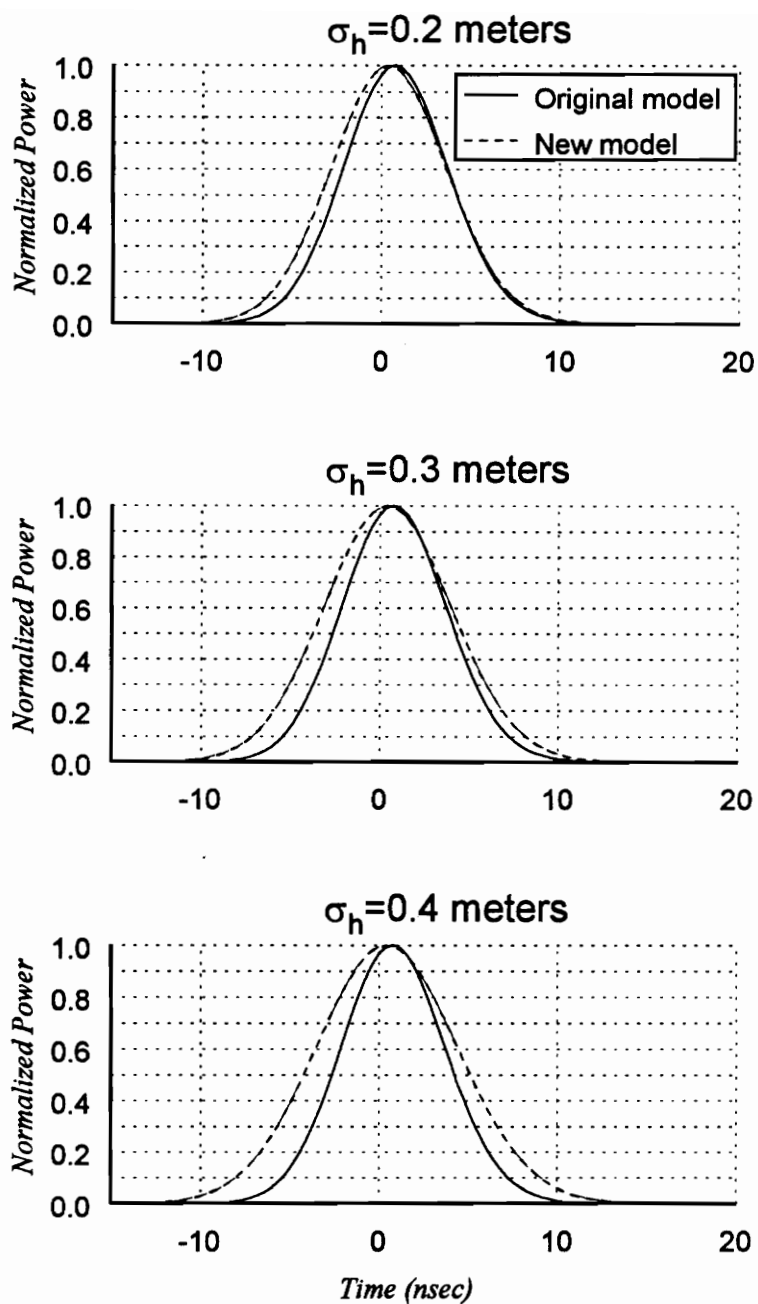


Figure 2.4. Volume scattered waveform model for the MARA system with $k_e = 4.0$ Np/m.

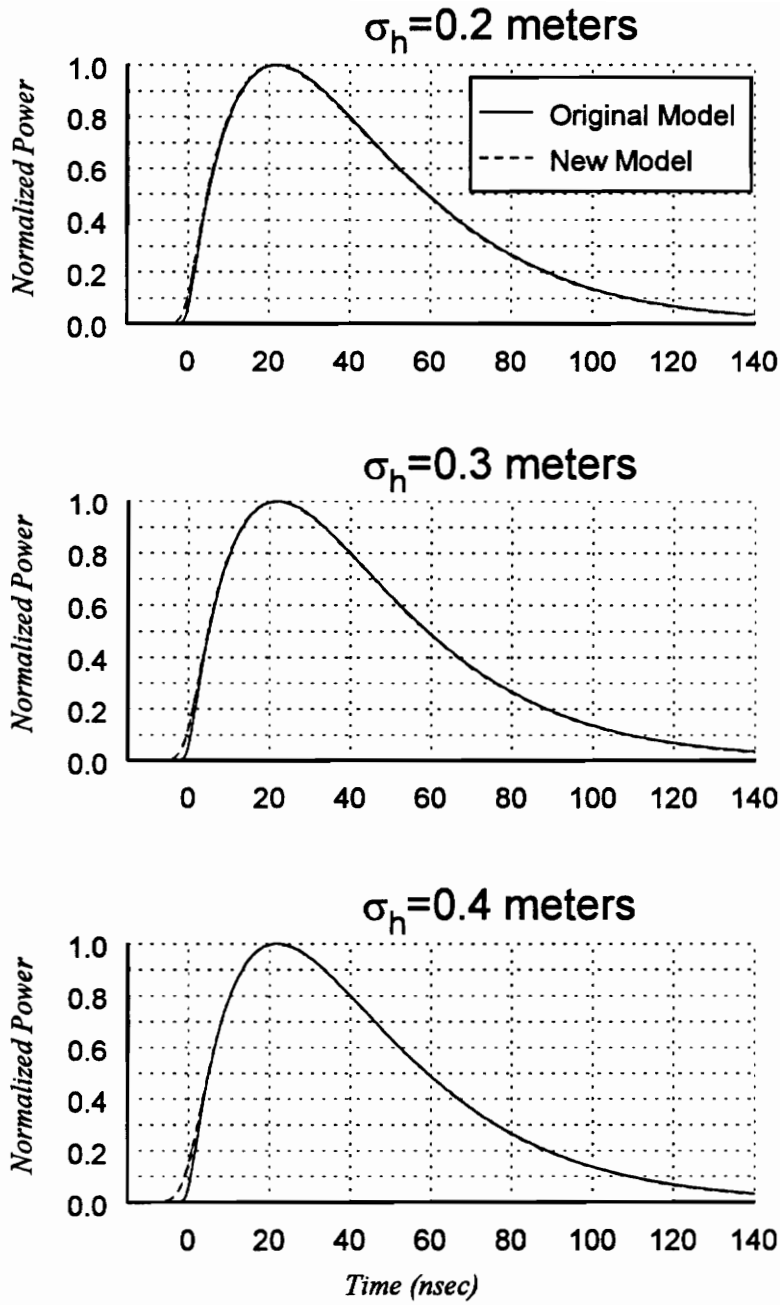


Figure 2.5. Volume scattered waveform model for the AAFE system with $k_e = 0.20$ Np/m.

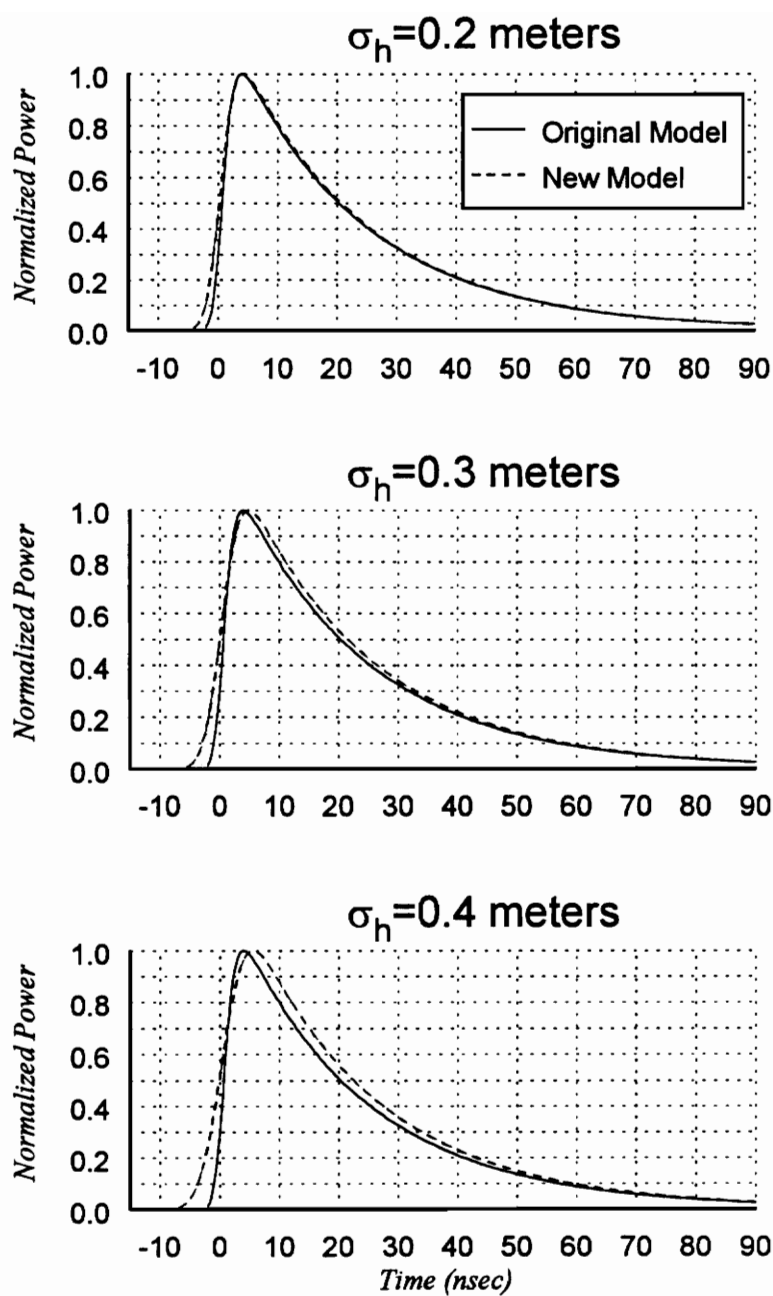


Figure 2.6. Volume scattered waveform model for the AAFE system with $k_e = 4.0$ Np/m.

Davis and Moore [10] have developed a closed form expression for the volume scattered waveform similar to the analytic form for the rough surface scattering model originally developed by *Brown* [5].

However, the assumptions made in deriving this closed form expression for nadir-directed satellite-based altimetry applications are not valid for narrow beamwidth altimetry applications from aircraft platforms. As discussed previously, to this end *Newkirk* [22] has developed a generalized volume scattering model. This model requires the numerical evaluation of a one-dimensional integral in determining the surface scattered waveform and the numerical evaluation of a two-dimensional integral in determining the volume scattered waveform. While certain asymptotic approximations to these integrals are possible under special circumstances, the model is in general numerically time consuming. This places a practical limit on its usefulness in analyzing a large number of radar returns.

However, the new volume scattered waveform model developed from the equations of transfer in this chapter is simply a convolution of the surface scattered waveform model with the new function E which is defined by the average characteristics of the scattering volume. As discussed above, for scattering volumes with homogeneous statistics, the function E is a decaying exponential function (c.f. (2-27)). Using the fast-Fourier-transform technique, this convolution can be performed rapidly once the surface scattered waveform has been determined. Thus, the new volume model requires no additional integrations be performed once the surface model has been obtained. At worst, the surface model only requires the evaluation of a one-dimensional integral which can be rapidly computed [22].

As a point of comparison, the computational speed of the new convolutional volume scattering model is compared to that of the model developed by *Newkirk* [22] for the MARA system. The comparison is made for scattering parameters typical of those evaluated in the brute-force parameter estimation technique discussed in Chapter 3 of this document. Furthermore, since various simplifications occur in the original model depending on the pointing angle of the radar, the comparisons are made versus pointing angle. The results of this comparison are shown in Table 2.1 where the computational savings are seen to approach a factor of 500 for a pointing angle of 3° off nadir for the MARA system⁵. Even for nadir directed applications the new form of the scattering

⁵ The altimeter system parameters used are a height of 500 m, a half-power beamwidth of 0.6° symmetric about the boresight, and a Gaussian transmitted pulse with a 6.5 nsec width. The medium parameters are a Gaussian height pdf with a 30 cm standard deviation and an effective extinction coefficient of 0.20 Np/m.

model provides a time savings factor of more than an order of magnitude. The altimeter system parameters used are a height of 500 m, a half-power beamwidth of 0.6° symmetric about the boresight, and a Gaussian transmitted pulse with a 6.5 nsec width. The medium parameters are a Gaussian height pdf with a 30 cm standard deviation and an effective extinction coefficient of 0.20 Np/m.

The large variation in the ratio of CPU times versus pointing angle in Table 2.1 is due to the various simplifications in *Newkirk's* model which occur for different pointing angles. At nadir *Newkirk's* model reduces to a one dimensional integral for a symmetric antenna pattern. Similarly, for larger pointing angles an asymptotic approximation of the model is made which reduces the two dimensional integral to a one dimensional integral. For the MARA system the transition into this asymptotic region occurs for pointing angles between 3° and 4° . The location of this transition will vary depending on the altimeter system being modeled.

Table 2.1. CPU time ratio comparisons

Pointing Angle	Ratio of CPU Times (Orig. Model)/ (New Model)
0°	12.8
1°	402.7
2°	409.9
3°	493.2
4°	37.6
7°	44.2
10°	46.2
12°	47.0
14°	49.2

Parameter Estimation

An example of the effect of the new model on parameter estimates derived from radar returns recorded by the MARA system over the Greenland ice sheet is shown in Figure 2.7. The three parameters shown in these figures are the rms surface roughness parameter⁶, σ_h , the extinction coefficient, k_e , and the volume-to-surface ratio η . The

⁶A Gaussian pdf with standard deviation σ_h is assumed. Other surface roughness distributions have not been investigated.

parameter η is the ratio of the peak value of the volume component of the scattered waveform to the peak of the surface component as defined in equation (2-63) below.

The three subplots in this figure illustrate the difference between the parameters predicted by the original and new models (original model parameter – new model parameter) for radar returns measured by the MARA system on September 20, 1991 over the Greenland ice sheet. Figure 2.8 shows the actual parameters predicted by the new model. Although the only difference between the scattering models lies in the inclusion of the rms surface roughness σ_h in the new volume model, Figure 2.7 demonstrates that the estimates of all three parameters have changed in using the new model to analyze the recorded data. The latitudinal variations in the parameters shown in these figures will be discussed in Chapter 3 of this report.

Parameter Definitions

Parameter estimates derived in a previous study using a scattering model of the type discussed in this chapter at 36 GHz [22] have led to values of the extinction coefficient for dry snow which differ significantly from those obtained using other techniques (e.g., [30, 31]). However, at 13.5 and 13.9 GHz the values obtained by previous authors (e.g., [12, 15]) using a model of the type discussed in this chapter agree reasonably well with those predicted for dry, small grained snow [30] using other techniques.

The reason for this frequency dependent relationship between the actual extinction coefficient and the effective value is apparent from the development of the new volume scattered waveform model. From equation (2-18) we see that the “extinction coefficient” in the new model is actually an effective value which includes contributions due to localized multiple scattering effects (see Appendix A)

$$\tilde{k}_e = k_e - \sigma_f \quad (2-62)$$

The fact that the effective extinction coefficient obtained at 13.5 and 13.9 GHz using this type of a model are in reasonable agreement with the actual extinction coefficient obtained using other techniques implies that σ_f is small at this frequency for dry snow. Similarly, the significant difference between \tilde{k}_e and k_e at 36 GHz for dry snow suggests that scattering effects are more important at 36 GHz than at 13.5 and 13.9 GHz. These observations are consistent with the statement of *Ulabay et. al.* [30] that, at frequencies above 20 GHz, scattering becomes the dominant component of extinction loss in dry snow.

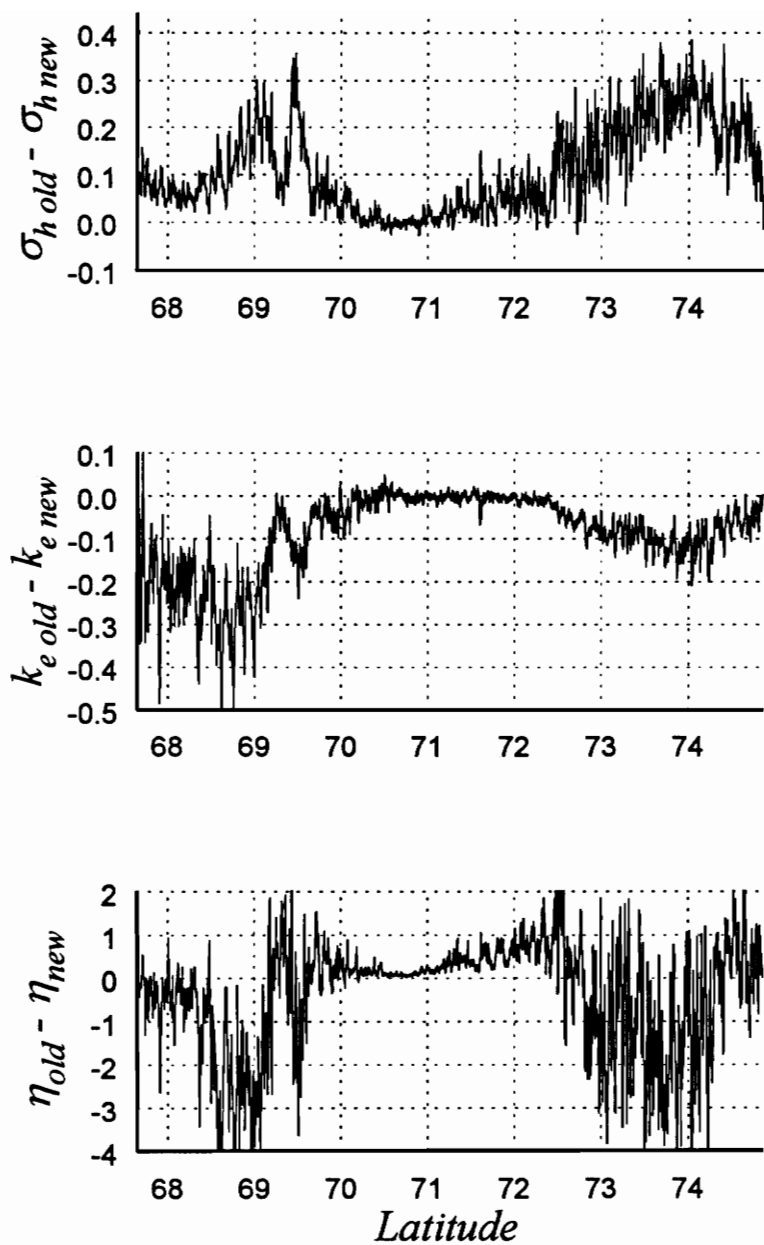


Figure 2.7. Difference in parameter estimates obtained using the original and new volume scattering models to analyze MARA data obtained on September 20, 1991.

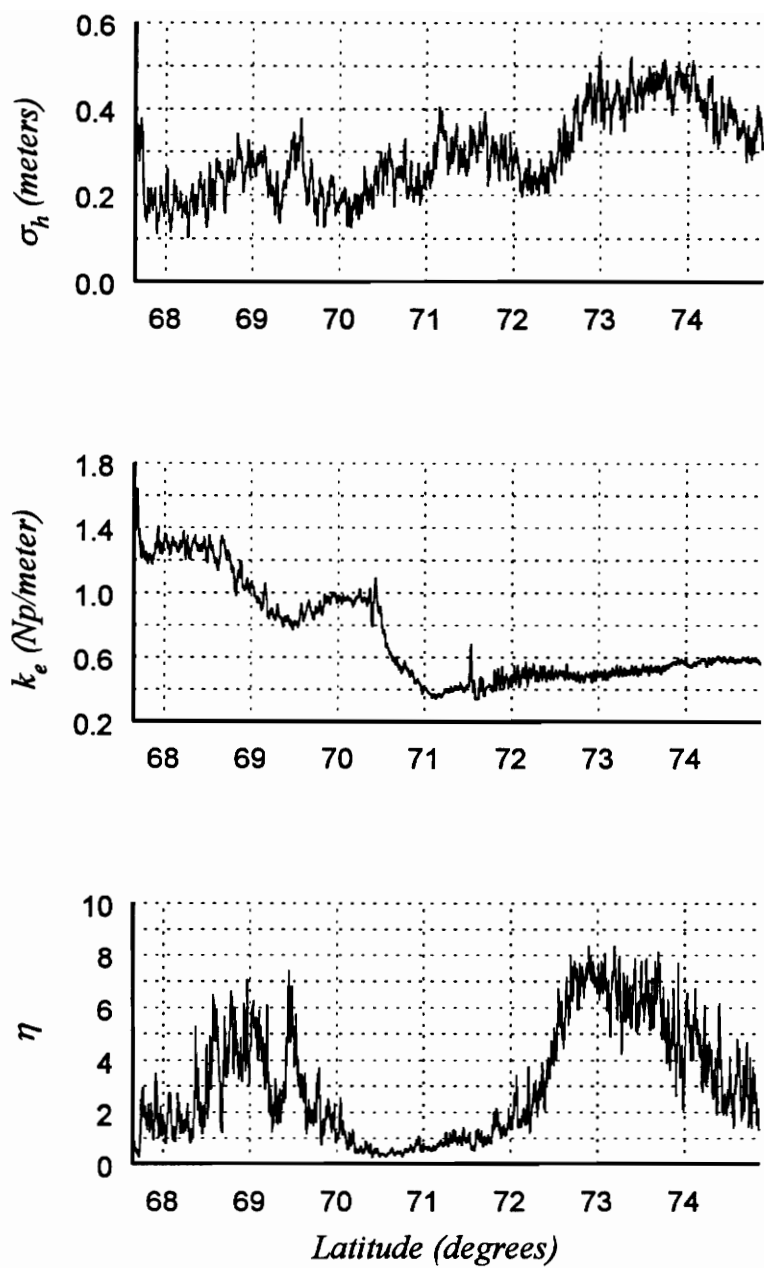


Figure 2.8. Parameter estimates for MARA data obtained on September 20, 1991 over the Greenland ice sheet.

For convenience, the effective extinction coefficient will be referred to simply as the extinction coefficient in the remainder of this document.

2.3.5 Capabilities and Limitations

Equation (2-54) for the new volume scattered waveform model is an expression for the waveform scattered from a rough, vertically distributed medium illuminated by a narrow beamwidth pulsed radar system. In deriving this expression from the equations of transfer it was assumed that the effects of long range, wide angle scattering could be neglected. The effects of multiple scattering between vertically distributed layers has also been neglected (see Appendix A). While it is possible to modify the above development to incorporate such effects, this has not been done here for two reasons. First, such a change to the model cannot be incorporated in a convolutional form. The scattering model would thus require significantly more CPU time to evaluate, removing one of the principle advantages of the new model. In addition, the nonhomogeneous form of the new model has not yet been used to study scattering from nonhomogeneous media and it is unknown whether including higher order scattering effects is necessary.

Future research will investigate the utility of the new model in analyzing scattering from layered media. It is expected that the new model will be useful in the remote sensing of penetrable geophysical media such as snow, sea ice and foliage which are known to exhibit layering in their physical structures.

2.4 The Combined Incoherent Scattered Waveform Model

Having available forms for the average surface and volume scattered waveforms, the form of the total scattered waveform is obtained as suggested by (2-1),

$$\langle P(t) \rangle = \langle S(t) \rangle + \langle V(t) \rangle \quad (2-1)$$

where $\langle S(t) \rangle$ and $\langle V(t) \rangle$ are given by (2-3) and (2-54), respectively. Representing the normalized versions of these average waveforms as $\bar{S}(t)$ and $\bar{V}(t)$ and the corresponding peak values as S_m and V_m , equation (2-1) can be rewritten

$$\begin{aligned} \langle P(t) \rangle &= S_m \bar{S}(t) + V_m \bar{V}(t) \\ &= S_m [\bar{S}(t) + \eta \bar{V}(t)] \end{aligned} \quad (2-63)$$

where $\eta = V_m/S_m$ is the ratio of the peak of the volume scattered waveform to the peak

of the surface scattered waveform. This parameter is called the volume/surface ratio in the remainder of this report.

In analyzing scattering data obtained by the AAFE and MARA altimeters over the Greenland ice sheet (see Chapter 3), only normalized data is available (because the radars were not calibrated prior to operation). The average normalized scattered waveform $\bar{P}(t)$ has the form

$$\bar{P}(t) = \alpha(\eta)[\bar{S}(t) + \eta\bar{V}(t)] \quad (2-64)$$

where $\alpha(\eta)$ is an appropriate normalization constant in the range 1 to $(1+\eta)^{-1}$. The volume/surface ratio η can range from 0 (for the case no volume scattering contributions) to infinity (for the case of no surface scattering). In practice, this range must be limited. For the parameter estimation procedure presented in Chapter 3 this is accomplished by restricting the search space for η to between 0.1 and 10. This range is chosen for this parameter since additional changes to the total waveform model resulting from values of the volume/surface ratio which lie outside this range are small.

Equation (2-64) with equations (2-3) and the homogeneous form of (2-54) are used in Chapter 3 of this document to analyze scattering data obtained by two altimeters which operated over the Greenland ice sheet. The process of fitting this model to scattered waveform data will result in estimates of the three parameters σ_h , k_e and η which describe the scattering from a region of the ice sheet. By comparing these values and the variation of these values with known variations in the physical properties of the ice sheet, an evaluation of the model's ability to model scattering over the ice sheet will be obtained. In addition, this process will also provide useful information on the ice sheet itself and on the ability of the radar altimeter to monitor various aspects of the ice sheet environment.

Chapter 3

Analysis of Multifrequency Altimeter Data

Chapter 1 provided a brief review of past work in modeling incoherent short pulse scattering from random surfaces and volumes. In Chapter 2 a new, more general scattering model was developed which includes these previous models as special cases. Partial validation of the new scattering model was obtained through a comparison with previously developed models. This chapter will continue the validation process by investigating the ability of the new scattering model to extract near surface information from altimeter returns obtained over the Greenland ice sheet. Although the new model is capable of incorporating the effects of a vertical distribution in the average scattering properties of the ice sheet, this ability is not investigated here. Instead the homogeneous form of the new model is applied to the ice sheet data set and the regions in which this form of the model is invalid are identified.

The altimeter data sets studied in this research were obtained by the Multimode Airborne Radar Altimeter (MARA) and the Advanced Aircraft Flight Experiment (AAFE) altimeter systems which operated simultaneously from an aircraft platform over the Greenland ice sheet in September of 1991. MARA is a five-beam, 36 GHz system operated by NASA [24] while the single-beam, 13.5 GHz AAFE system was operated by the University of Massachusetts at Amherst [15]. According to the definitions given in [23], each beam of the MARA system is considered to be *beamwidth-limited*, while the single beam of the AAFE system is *pulsewidth-limited*. The qualitative difference between these systems is that for MARA, the antenna beamwidth controls the extent of the illuminated area on the surface, while for AAFE the transmitted pulsewidth controls the illuminated area. While these different system configurations provide unique views of the ice sheet, a more important factor which causes these systems to “see” the ice sheet differently is their widely separated center frequencies. Due to its significantly lower operating frequency, pulses transmitted by the AAFE system penetrate much farther into

the ice sheet than those transmitted by MARA. This is a manifestation of the well-known frequency dependence of the extinction coefficient for snow [30]. This difference in the depth of penetration for each system means that each will respond differently to the same section of the ice sheet.

In an effort to familiarize the reader with what these altimeters will “see” over the various regions of the ice sheets, Section 3.1 of the current chapter provides a brief discussion of the physical and scattering properties of the different regions of the ice sheet. This is followed by a synopsis of the operational aspects of the two altimeters in Section 3.2. Section 3.3 discusses the important process of obtaining an approximation to the *average* scattered waveform from *individual* return pulses measured by the MARA system.

Sections 3.4 and 3.5 contain the primary results of the current chapter. Section 3.4 details the parameter estimation procedure used to obtain estimates of the scattering parameters defining the ice sheet from the scattering data. The results of this estimation process are subsequently used to evaluate the radar altimeters’ ability to determine the boundaries between the various regions of the ice sheet and to reliably monitor the near surface properties of the ice sheet within each region. Section 3.5 presents an evaluation of the altimeters’ ability to accurately measure the surface elevation of the ice sheet. This final result is obtained through an intercomparison of the elevation estimates derived from the two altimeter systems with similar results obtained from the AOL laser profilometer which operated simultaneously with the radars.

3.1 The Greenland Ice Sheet

The electromagnetic scattering properties of the Greenland ice sheet have been discussed by several authors [12,15,22]. The primary source of information on the physical properties of the ice sheet used by these authors is a 1962 report which is based on pit studies of the ice sheet made by a small group of workers over several years [2]. Although these sources provide good descriptions of both the physical and electromagnetic properties of the various regions of the ice sheet, a brief review is presented here for completeness.

The Greenland ice sheet is divided into four regions based on the physical properties of the near surface region of the ice sheet. These four regions (or *diagenetic facies*) of the ice sheet are called the ablation, soaked, percolation and dry-snow facies (see Figure 3.1). The location of these facies on the ice sheet relative to the radar platform’s flight line is

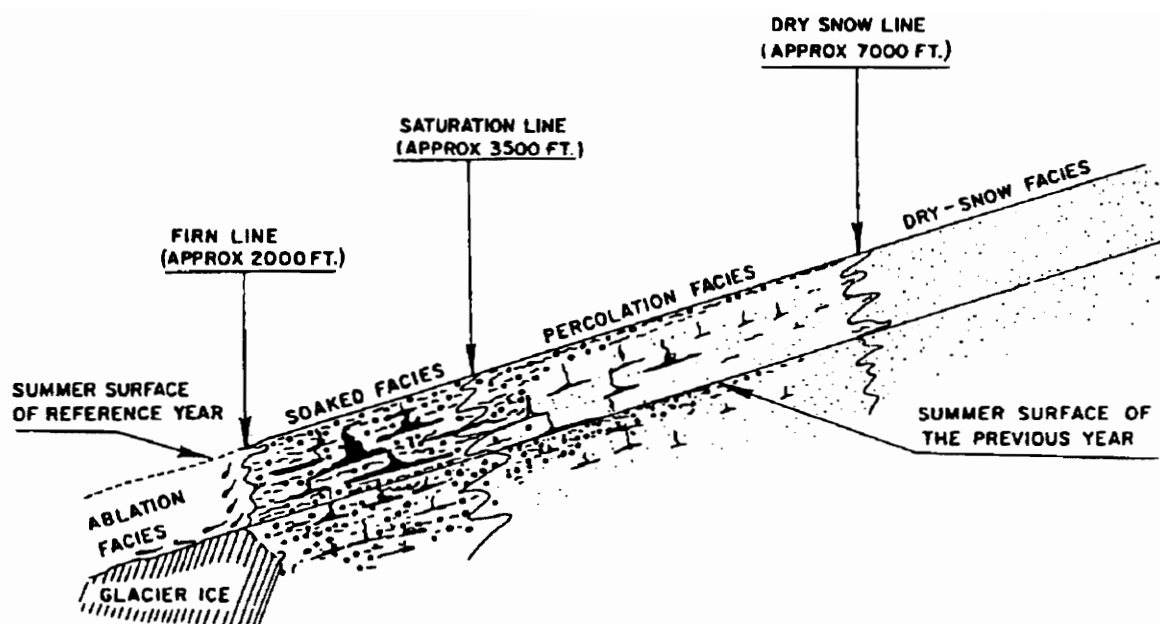


Figure 3.1. Illustration of the various diagenetic facies of the ice sheet. From [2].

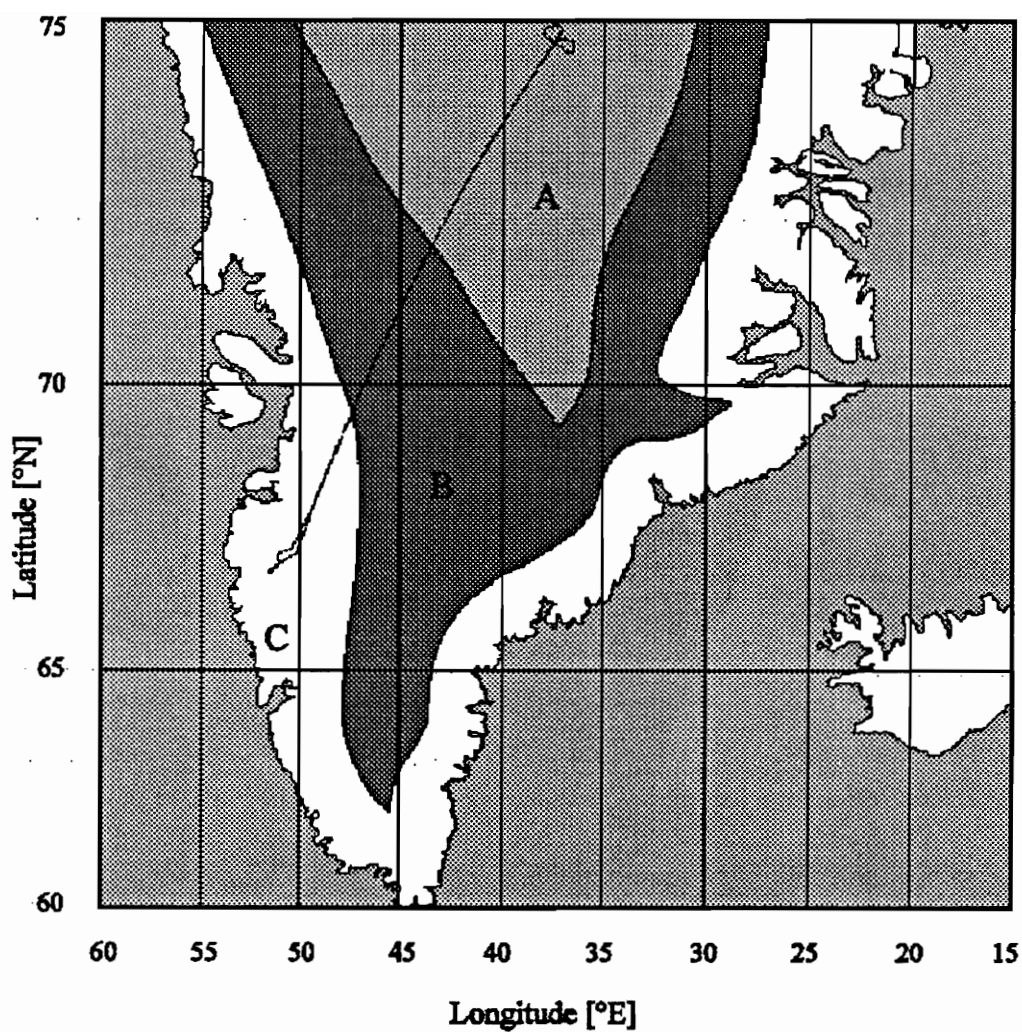


Figure 3.2 Map of Southern Greenland showing the flight line for the example data and the: (A) dry snow, (B) percolation, and (C) soaked and ablation regions. From [22]

illustrated in Figure 3.2. The data set analyzed in this chapter includes scattering data obtained over sections of all four facies of the ice sheet. Since the electromagnetic properties in the near-surface region of the ice sheet vary significantly between the different facies, this data set provides an excellent opportunity to evaluate the validity of the newly developed scattering model under different near surface scattering conditions.

The Ablation Facies

An illustration of the relative location and properties of the four facies of the ice sheet is shown in Figure 3.1. As suggested in the figure, the primary factor in determining the location of the boundaries between the facies is the elevation of the ice sheet. As the elevation of the ice sheet increases the mean seasonal temperature falls, resulting in significantly different climates for different regions of the ice sheet. The *ablation* facies of the ice sheet is seen to extend from the outer edge of the ice sheet to the firn line which separates the ablated and soaked facies. The firn line is the highest elevation to which the annual snow cover recedes during the melt season. Thus, during the melt season, the surface of this region consists largely of wet glacier ice and small surface melt ponds [2].

Due to the presence of large amounts of surface moisture, the scattering in this region of the ice sheet is expected to be dominated by surface scattering effects. Unfortunately, information is not available on the properties of the surface roughness in this region. Such information would be desirable for several reasons. Among these is the fact that it is not clear to what degree the surface scattering model, which is based on the quasi-specular scattering assumption, is valid in this region. In addition, without a knowledge of the scales of the surface roughness in this region it is not known whether the AAFE and MARA altimeters should be expected to measure the same or different surface roughness values. As shown in Table 3.1, the footprint of the MARA system is more than 26 times narrower than the AAFE footprint. Thus, MARA may effectively filter out large scale roughness features which AAFE may respond to. Conversely, if the surface roughness occurs on a small scale relative to the MARA footprint, both systems should provide the same estimate of the surface roughness (provided that quasi-specular model is valid for both systems).

The Soaked Facies

The *soaked* facies becomes wet throughout during the melting season and extends from the firn line to the saturation line. As in the ablation zone, scattering in this region is expected to consist primarily of surface scattering effects due to the presence of large

amounts of surface moisture and/or large snow grain sizes in the near surface region of the ice sheet which result in larger values of the extinction coefficient relative to the colder facies of the ice sheet (the presence of large numbers of freeze/thaw cycles in this facies is known to produce higher density snow with larger average particle sizes than in the percolation and dry snow regions [2]). However, as mentioned above for the ablation zone, the absence of information on the characteristics of the surface of the ice sheet in this region prevents a definitive evaluation of any surface roughness estimates derived from this region of the ice sheet.

The Percolation Facies

The *percolation* facies is subject to localized percolation of melt water from the surface into the snow pack without becoming wet throughout. Percolation can occur in snow and firn which are at subfreezing temperatures with only the pipe-like percolation channels being at the melting point [2]. This process produces a subsurface network of ice lenses, layers and glands which are surrounded by smaller grained, lower density dry snow. The sizes of the ice lenses, layers and glands formed by the percolation channels are generally much larger than the wavelengths of the 36 GHz MARA and 13.5 GHz AAFE systems [2].

Strong contributions to the backscattered waveforms due to these large subsurface inhomogeneities has been found to cause the average scattered waveform for the 13.5 GHz AAFE system to deviate significantly from the form predicted by the homogeneous scattering model [15]. Given this information it is not possible to determine *a priori* whether the effects of these inhomogeneities on the 36 GHz data will be similar to those observed at 13.5 GHz due to the different penetration depths of the two systems. For example, if the strong inhomogeneous scatterers of the percolation zone are located below the 36 GHz penetration depth, the homogeneous assumption may provide an adequate description of the scattering from this region.

The Dry-Snow Facies

Finally, the *dry-snow* facies includes all regions of the glacier above the dry-snow line and negligible melting occurs in it. Unlike the firn and saturation lines which are readily discernible from pit studies of the ice sheet, the dry-snow line is an ill-defined transition zone which is 10-20 miles wide [2]. Due to the lack of strong subsurface inhomogeneities such as those found in the percolation zone, it is expected that the scattering model will provide a more accurate description of the physical processes in this region of the ice sheet

than in the percolation zone. Deviations from the homogeneous scattering model result are still expected, however, due to the depth dependent densification of the snow which results from its own weight. This effect causes the density of the snow to increase with depth below the surface. It is expected that these depth-dependent inhomogeneous effects will be more significant for the AAFE system than for MARA due to its significantly larger penetration depth.

3.2 The Altimeter Systems

The altimeter data examined in this report was taken from archives of the MARA and AAFE systems. MARA data from September 18, 19 and 20, 1991 and AAFE data from September 18, 1991 are analyzed in the following sections. Both altimeters, along with NASA's AOL laser profilometer, operated simultaneously from the same aircraft platform over the Greenland ice sheet in September of 1991. Table 3.1 provides a comparison of the salient features of the MARA and AAFE altimeter systems. A more detailed discussion of these systems can be found elsewhere [15, 22, 24].

As mentioned above, the AAFE altimeter is a pulsewidth-limited, nadir-directed single antenna system. The beamwidth-limited MARA system has five beams, only one of which is directed in the nadir direction. The remaining four beams are directed at approximately 12° off-nadir in the forward, aft, left and right directions relative to the P-3 aircraft which housed the altimeter [22]. Unfortunately, the aft-looking beam of the MARA was not used during this experiment because of erratic behavior in its digitization hardware. It has also been determined that the data gathered by the nadir beam of the MARA system is unusable due to the higher than expected received power levels which saturated the receiver. This is illustrated in Figure 3.3 where the peak received power versus latitude along the flight line of Figure 3.2 is shown for the four operable beams on September 19, 1991. Thus, direct comparison of the MARA and AAFE nadir data is not possible. However, given that the altimeters operated simultaneously over a long section of ground track, it is expected that any variations in scattering parameters between the two systems (or between the various MARA beams) due to illumination of different areas of the ice sheet will not have a noticeable effect on the average parameter estimates.

In the following analysis and comparison of these altimeter systems it will be necessary to refer to various points along the flight line shown in Figure 3.2. The position of the aircraft varies both in latitude and longitude along the flight line. From the position of the flight line on the ice sheet, it is also known that the aircraft flew up the side of the glacier

Table 3.1. Summary of the MARA and AAFE system parameters. Values are taken from [24] for MARA and [15] for AAFE. The S/N ratios are calculated for $\sigma^o = -23$ dB. From [1].

Parameter	MARA	AAFE
frequency (GHz)	36.0	13.9
band	Ku	Ka
intermediate (IF) frequency (MHz)	600	1080
wavelength (mm)	8.33	21.6
peak power per channel (W)	200	0.1
nominal pulsewidth (ns)	6.5	2.7
bandwidth (MHz)	220	360
PRF (Hz)	100	750
E -plane beamwidth - nadir ($^\circ$)	0.6	15
- off-nadir ($^\circ$)	0.9	—
H -plane beamwidth ($^\circ$)	0.6	15.6
number of beams	5	1
antenna gain (dB)	46.0	21.6
illuminated diameter (nadir, $h = 500$ m) (m)	5.2	137.0
number of samples/waveform	48	101
sample increment (ns)	2.226	2.77
receiver noise figure (dB)	10	13.3
S/N (at 1 km altitude) - nadir (dB)	25	23.5
- off-nadir (dB)	17.5	—

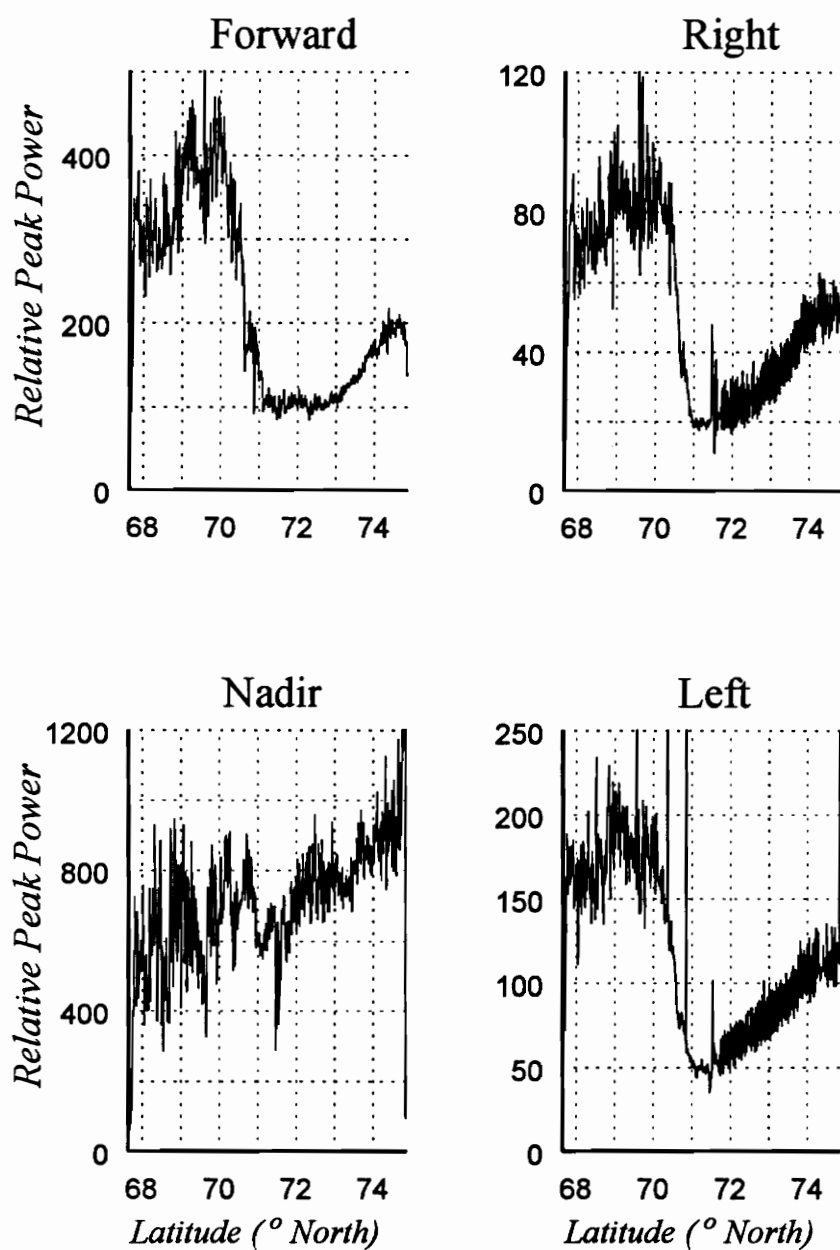


Figure 3.3. Relative peak power measured by the four beams of the MARA system on September 20, 1991.

at an angle [2]. That is, on the northeast-bound leg of the flight line the left antenna of the MARA altimeter points slightly downhill while the forward and right antennas point in a slightly uphill direction. The converse is true for the southwest-bound leg of the flight line. The change in the surface elevation of the ice sheet along the flight line is demonstrated in Figure 3.4. In the following discussion the aircraft's position along the flight line will be referenced only by its latitudinal location. The associated changes in longitude and elevation are implied. In addition, the aircraft's heading will be specified as north- (south-) bound when discussing data gathered while the aircraft was headed in a true northeast- (southwest-) bound direction.

3.3 Scattered Waveform Retracking

An important aspect of any altimeter system is its onboard tracker. Descriptions of tracker performance for aircraft and satellite borne altimeters can be found, for example, in *Ferraro* [15] and *Marth, et al.* [19]. The primary purpose of the onboard tracker is to keep the received scattered waveforms within the *range window* of the altimeter, and to provide an estimate of the distance from the radar platform to the mean scattering surface. MARA's range window consists of 48 digital samplers separated by 2.226 nanosecond intervals⁷. The effective length of the range window is thus

$$l = (47)(2.226 \text{ ns})(0.3 \text{ m/ns}) = 31.4 \text{ meters} \quad (3.1)$$

The onboard tracker is designed to coordinate the timing of the samplers such that the scattered pulses are centered within the range window. Returns which occur outside this 31.4 meter interval are not observed by the radar.

The tracker for the MARA system used an absolute threshold trigger to locate the scattered waveforms within the range window. This is illustrated in Figure 3.5(a) where the location of several waveforms tracked by the onboard tracker are shown within the range window. In addition to keeping the scattered waveforms centered in this window, the MARA tracker also estimates the range to the mean surface based on this absolute threshold track point. The actual, or untracked, location of the backscattered waveforms within the range window is shown in Figure 3.5(b).

While this threshold tracker works well to keep the MARA waveforms centered within the range window, the error in the threshold derived range estimates can be significant. This problem arises due to the severe intrapulse fading of the scattered waveforms, and

⁷See [15] for a discussion of the tracking algorithm used for the AAFE system.

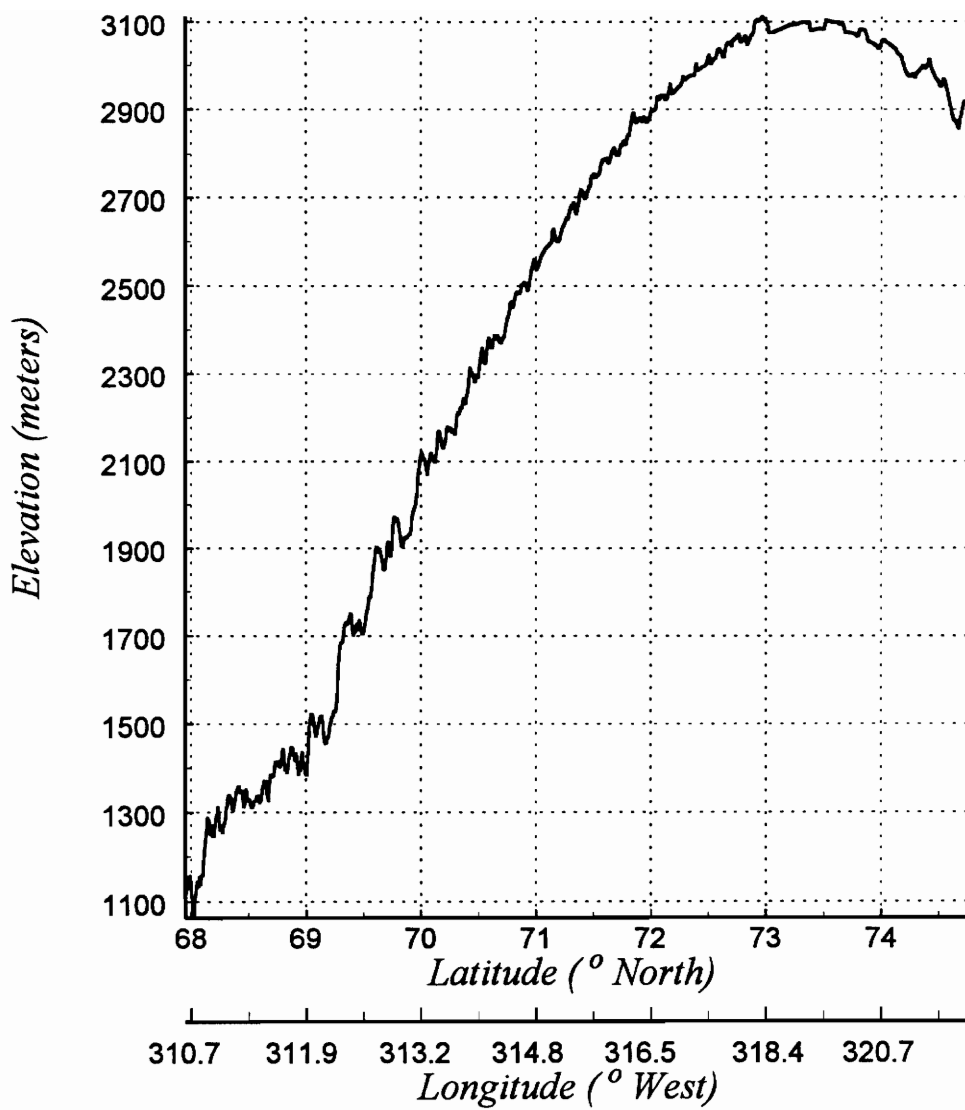
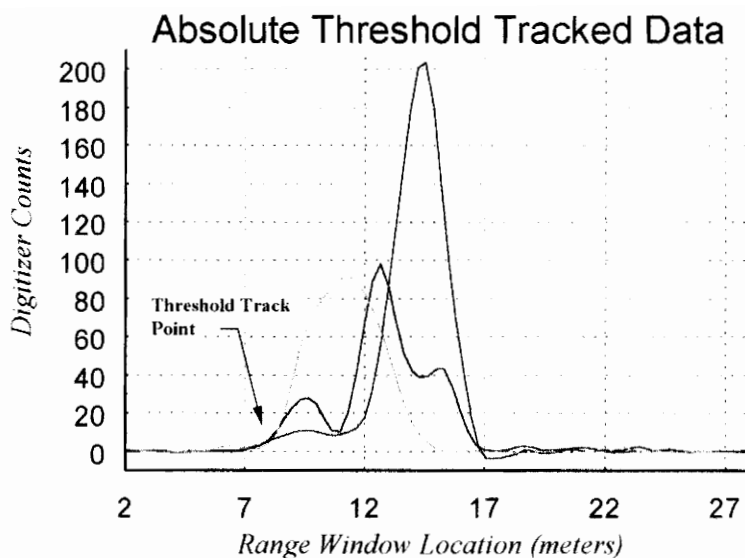
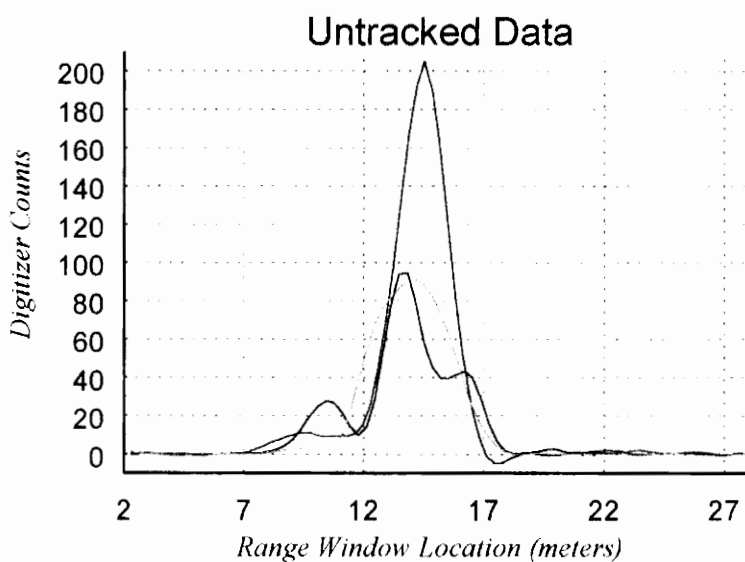


Figure 3.4. Elevation vs. latitude and longitude along the flight line shown in Figure 3.2.



(a)



(b)

Figure 3.5. Individual scattered MARA waveforms as tracked by the onboard tracker in (a) and as they actually arrived at the altimeter in (b). The corresponding range words for these pulses are different in (a) and have been adjusted such that they are all equal in (b).

because the arbitrarily chosen threshold level does not necessarily correspond to the point on the scattered waveform which represents the location of the mean scattering surface.

More accurate range estimates are obtained by retracking the scattered waveforms using the scattering model developed in Chapter 2. By fitting the model to an *average* scattered waveform, the point on the waveform which corresponds to the mean surface can be determined. This fitting process uses a knowledge of the average scattering process to effectively interpolate between the recorded points on the average waveform. This provides a range estimate which can exceed the pulsewidth resolution of the radar.

In addition to providing ranging data, this process also provides information on the average properties of the scattering medium through the parameters σ_h , k_e and η which are determined in fitting the model to the average scattered pulse. A drawback to this retracking technique, however, is that a large number of raw waveforms must be used to obtain a good approximation to the average waveform for fitting with the scattering model. This results in significantly reduced along-track surface resolution. As discussed below, this problem can be partially remedied for the AAFE and MARA systems by increasing the PRF of the respective radars.

Further difficulties arise in fitting the scattering model to measured data due to the assumptions made in deriving the model for the average scattered waveform. In the development of this model in Chapter 2, several random surface and volume variables were averaged over. The other variables in the problem (e.g., radar pointing angle and altitude) were held constant over this averaging period. In practice, the average scattered waveform is approximated by averaging several individual scattered waveforms obtained along a small section of the radar platform's flight line. Unlike the averaging process discussed for the model developed in Chapter 2, several variables in the problem can change over this averaging interval. The most significant of these are:

- 1) pitch and roll variations in the radar platform,
- 2) changes in the distance between the radar platform and the mean scattering surface due to movement of the radar platform and/or changes in the mean surface elevation,
- 3) nonstationary surface and near-surface statistics of the scattering terrain over the averaging period.

Since the distance over which both the AAFE and MARA returns were averaged was on the order of 100 meters, it has been assumed that the effect of nonstationary surface statistics on the average scattered waveform can be ignored.

The variation in the pitch and roll of the aircraft effectively produces a variation in the pointing angle ξ defined in Chapter 2. Changing the pointing angle for the MARA system is seen in Figure 3.6 to cause a significant change in the shape of the average scattered waveform. It is not clear how such effects can be removed from the individually scattered pulses in obtaining the average waveform. This problem is avoided by choosing the averaging period to be sufficiently short so that the change in the radar's pointing angle is small over the averaging interval. Thus, variations in the individual scattered waveforms due to pointing angle effects are avoided.

The variations in the location of the radar platform and changes in the mean surface elevation each have similar effects on the scattered waveforms. These effects are illustrated in Figure 3.7. For small height fluctuations (relative to the platform's altitude) the location of the scattered waveform within the range window changes. However, the shape of the scattered waveform does not change. Thus it is possible to remove this effect in obtaining the average scattered waveform by shifting the waveforms in the range window. The shifting of the pulse is accounted for by adjusting the range word associated with the pulse by an amount corresponding to the magnitude and direction the pulse is shifted within the range window.

The difficulty in removing this variability in the distance from the mean surface to the radar platform lies in knowing how much to shift the individual scattered pulses. That is, we desire to shift the pulse by an amount equal and opposite to the change in the distance from the platform to the mean surface without actually knowing this value. One way to approximately accomplish this is to align them based on the shape of the scattered waveform, under the assumption that this shape does not change significantly along a small section of the ground track. To this end, several alignment methods including half-power, peak and centroid techniques were evaluated and found to perform inadequately (the alignment methods are discussed below). The reason for their poor performance lies in the random nature of the scattered waveforms. As illustrated in Figure 3.5, the shape of the raw scattered waveforms changes significantly from pulse to pulse.

The variation in the distance from the radar platform to the mean surface over the averaging interval is instead removed in two steps. First, the effect of MARA's onboard tracker is removed from a small number of scattered waveforms (ten for all MARA data

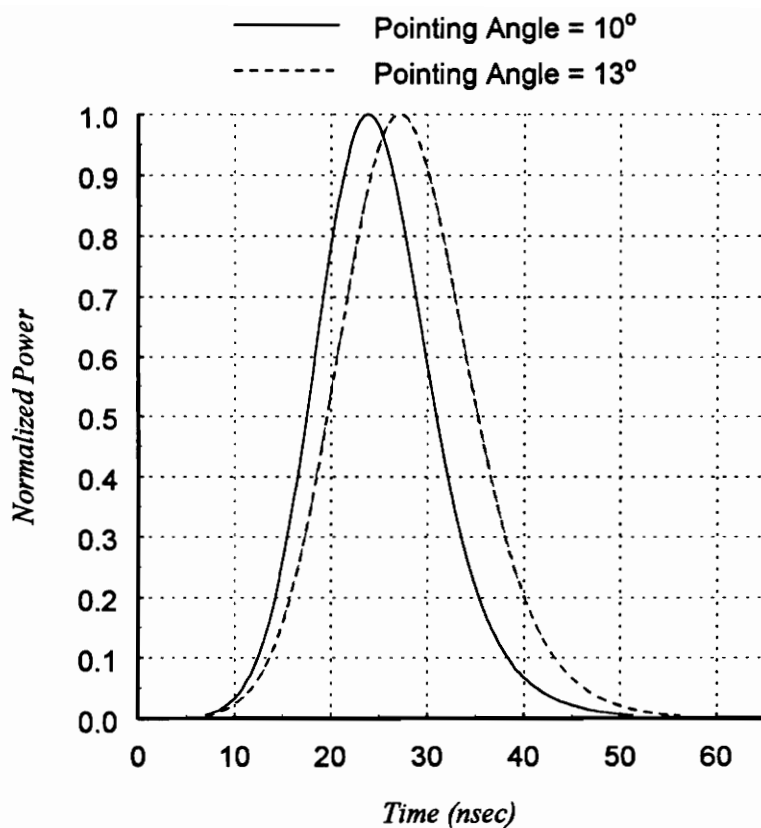


Figure 3.6. Example of the effect of a pointing angle change on the average scattered MARA waveform. The range displacement has been removed so only the waveform shapes are compared.

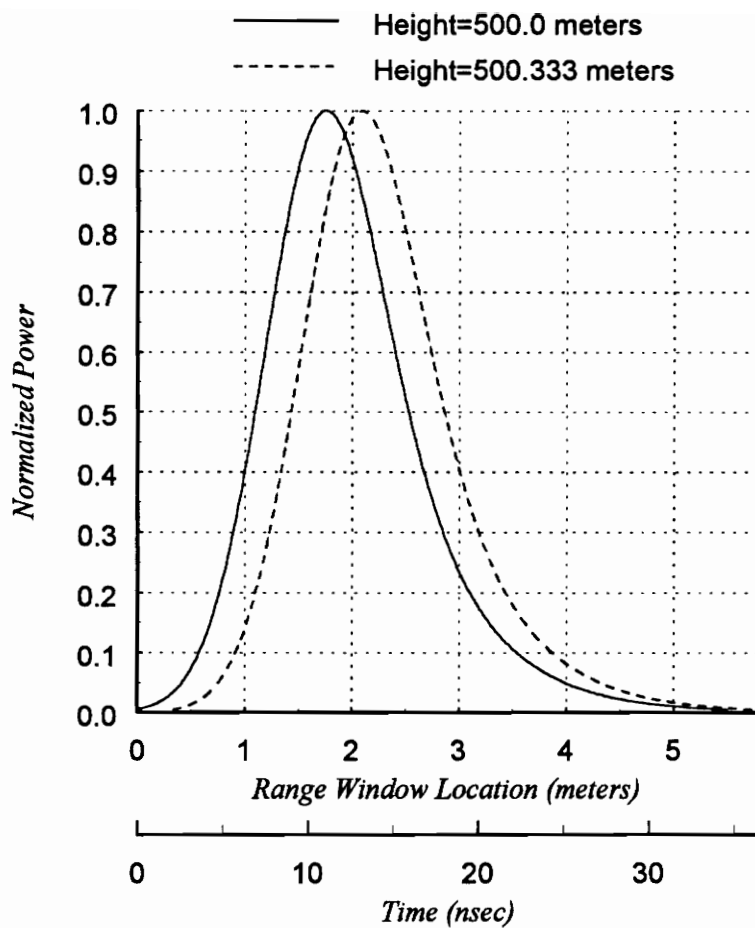


Figure 3.7. Model MARA waveforms for radar platform heights of 500 and 500.333 meters above the mean surface. The only difference is in the location of the waveform in the range window.

analyzed in this report). This is accomplished by selecting a small group of waveforms and changing the range values for all the waveforms to the range value of the first waveform. This change in the range word is then accounted for by shifting the pulses within the range window by an amount corresponding to the difference between the original range word and the new range word. This process is illustrated in Figure 3.5(b). This small group of pulses is then averaged at their untracked location within the range window.

In this process it is assumed that the change in the range to the surface is small over the section of the flight line corresponding to this small number of scattered pulses. For MARA with a PRF of 100 Hz and a nominal ground speed of 100 m/s, this sub-averaging interval corresponds to approximately ten meters along the ground track of the altimeter. The change in the location of the average received pulse due to a 0.333 meter change in the distance from the radar platform to the mean surface is shown in Figure 3.7. This sensitivity to small changes in the distance from the radar platform to the surface is due to the narrow width of the scattered pulses. This is a result of the beamwidth-limited nature of the MARA system and effectively limits the number of waveforms which can be aligned in this manner. Since a better approximation to the average scattered waveform than that provided by only one of these sub-averaged waveforms is needed for comparison with the scattering model developed in Chapter 2, it is further necessary to average several of these sub-averaged waveforms.

Fortunately, due to their more stable nature, it is possible to align the sub-averaged waveforms based on their shapes by using a centroid alignment technique. The centroid x_c of the sub-average waveform is defined as the first moment of the waveform divided by its mass, i.e.

$$x_c = \frac{\sum_{n=1}^{48} n\Delta t \cdot S(n\Delta t)}{\sum_{n=1}^{48} S(n\Delta t)} \quad (3-2)$$

where $S(n\Delta t)$ is the n^{th} sample of the waveform recorded by the altimeter and $\Delta t = 2.226 \text{ ns}$ is the sample interval of the MARA receiver. The summations are performed over the 48 points in the range window of the MARA receiver.

Having thus determined the centroid, the waveform is subsequently splined and the spline function evaluated at 47 new points such that one of the new points corresponds exactly to the centroid location of the waveform. This procedure is repeated for ten of the

sub-averaged waveforms. The resultant waveforms are then aligned at their centroid location and averaged as shown in Figure 3.8. The final average waveform is thus the average of 100 individually scattered pulses - an average of ten sub-averaged waveforms, with each of the sub-averaged waveforms itself the average of ten untracked waveforms. A diagram of the alignment process used for the MARA data is shown in Figure 3.9.

Other waveform epoch alignment methods were evaluated for alignment of the sub-average waveforms. These techniques included half-power and peak alignment techniques. The half-power technique consists of aligning the sub-average waveforms at the half-power point on the leading edge of the waveform. In the peak alignment method, the sub-average waveforms are aligned at their maximum value. The parameter estimates derived by fitting the model developed in Chapter 2 to MARA data aligned using these techniques are compared to those derived from the centroid alignment technique in Figures 3.10–3.12. Note that using threshold alignment produces smaller estimates of σ_h than the other two techniques. This is a feature of the alignment technique that was observed consistently for the MARA system.

The graph of the volume/surface ratio η in Figure 3.12 also shows the effect of using peak alignment on five groups of the sub-averaged waveforms derived from 20 raw pulses. Although the use of peak alignment of ten groups of sub-averaged waveforms based on ten pulses produces significantly different estimates than the centroid and threshold alignment techniques, peak-aligning five groups of sub-averaged waveforms derived from 20 pulses results in estimates for η similar to those obtained using the centroid and threshold alignment schemes. This suggests that the true peak of the average scattered waveform is not well approximated using only ten raw waveforms to form the sub-averaged waveforms.

Due to the more robust nature of the centroid alignment technique relative to the other techniques discussed above for the MARA system, this method is used to align the groups of sub-averaged waveforms in obtaining all average scattered waveforms analyzed in this report. The sensitivity of this choice to the number of waveforms used to form the sub-average waveforms is illustrated in Figure 3.13–3.15. While small differences are apparent, agreement is generally quite good. The variability in the parameter values shown in these figures provides an estimate of the reliability of the parameter estimates derived from the MARA system.

Notice also from Figures 3.11 and 3.14 that the effective extinction coefficient k_e is relatively insensitive to the choice of alignment technique, something consistently observed

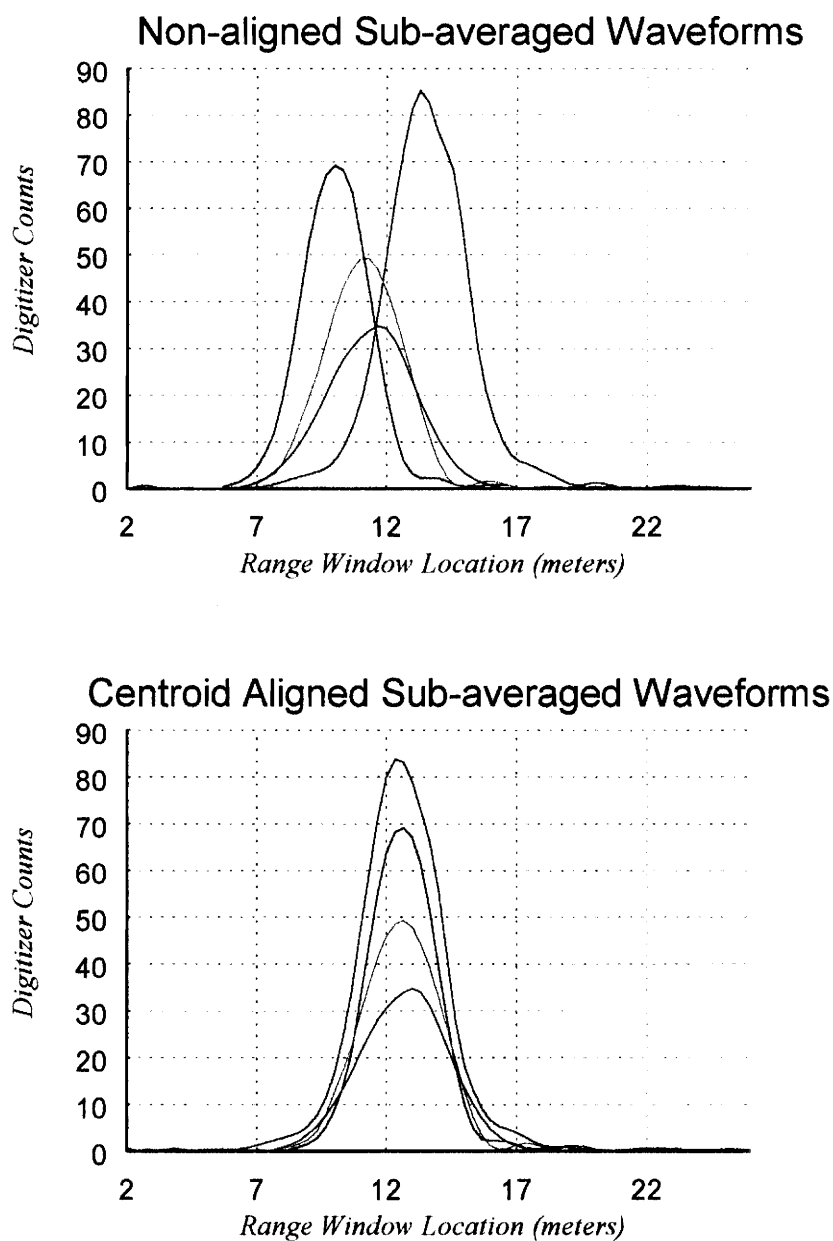


Figure 3.8. Non-aligned and centroid aligned sub-average waveforms.

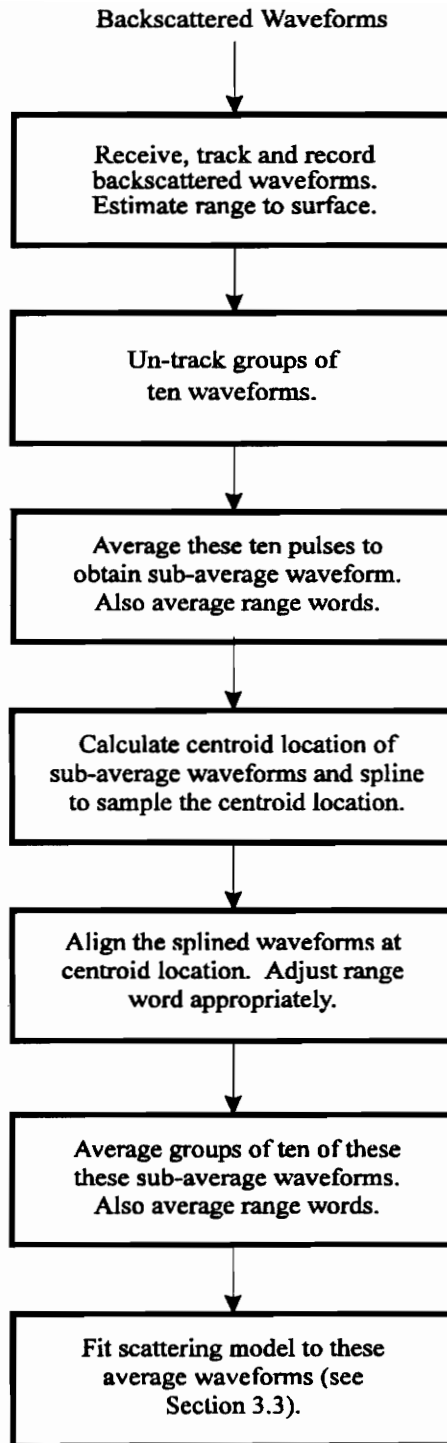


Figure 3.9. Block diagram indicating waveform averaging procedure used for all MARA data contained in this report.

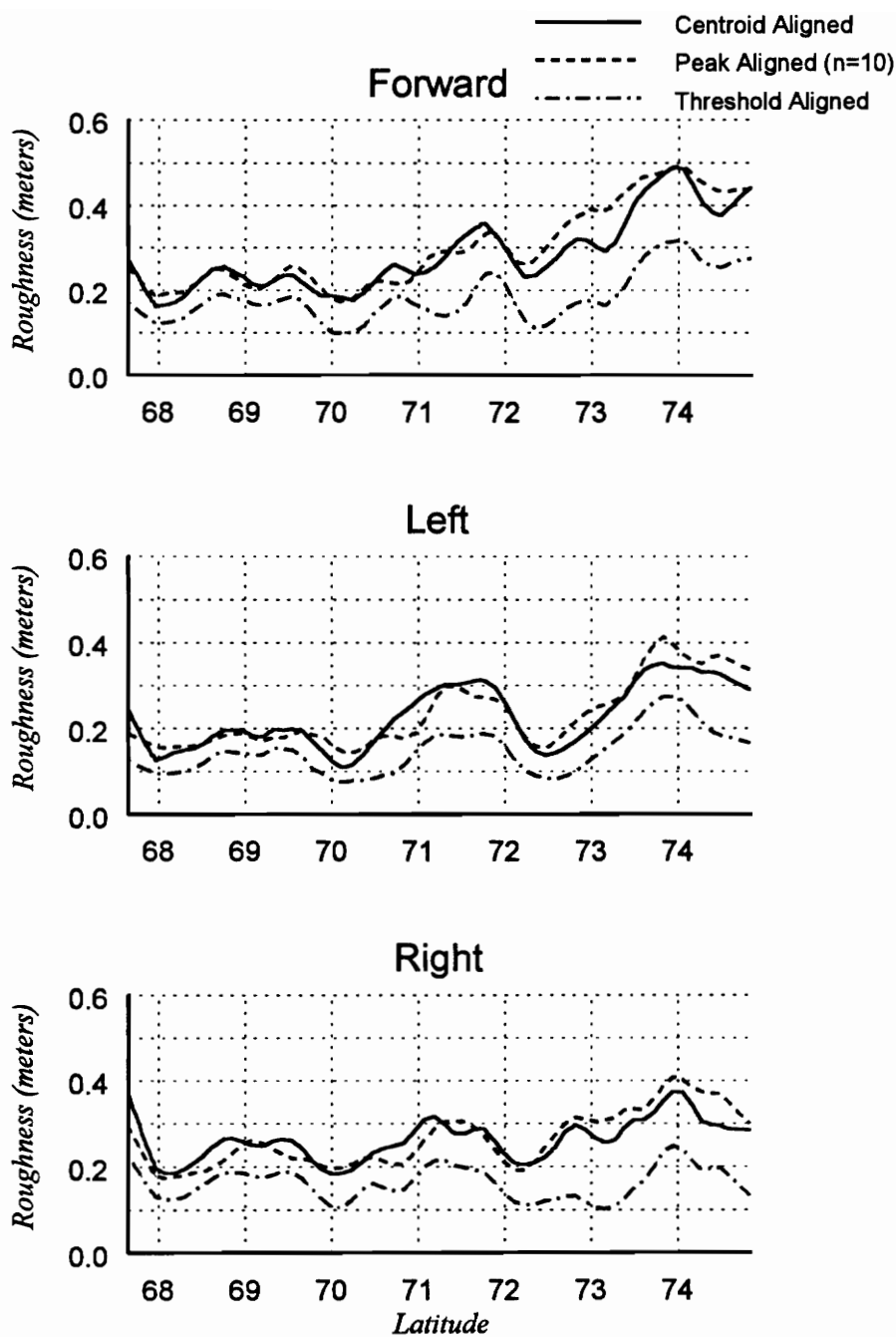


Figure 3.10. rms surface roughness estimates obtained using various alignment techniques. The threshold aligned data were aligned at the half-power point on the leading edge of the sub-average waveforms.

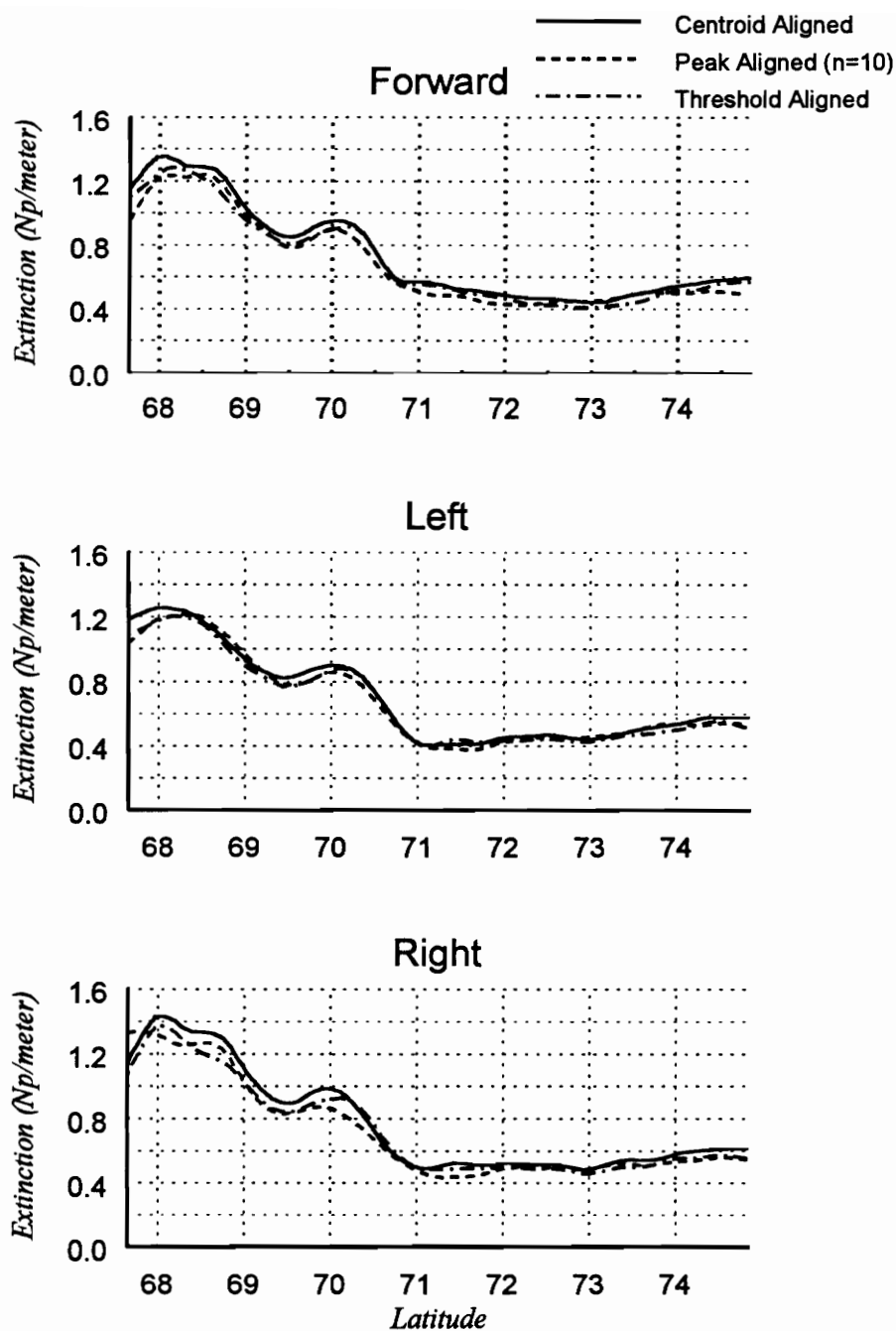


Figure 3.11. Extinction coefficient estimates obtained using various alignment techniques. The threshold aligned data were aligned at the half-power point on the leading edge of the sub-average waveforms.

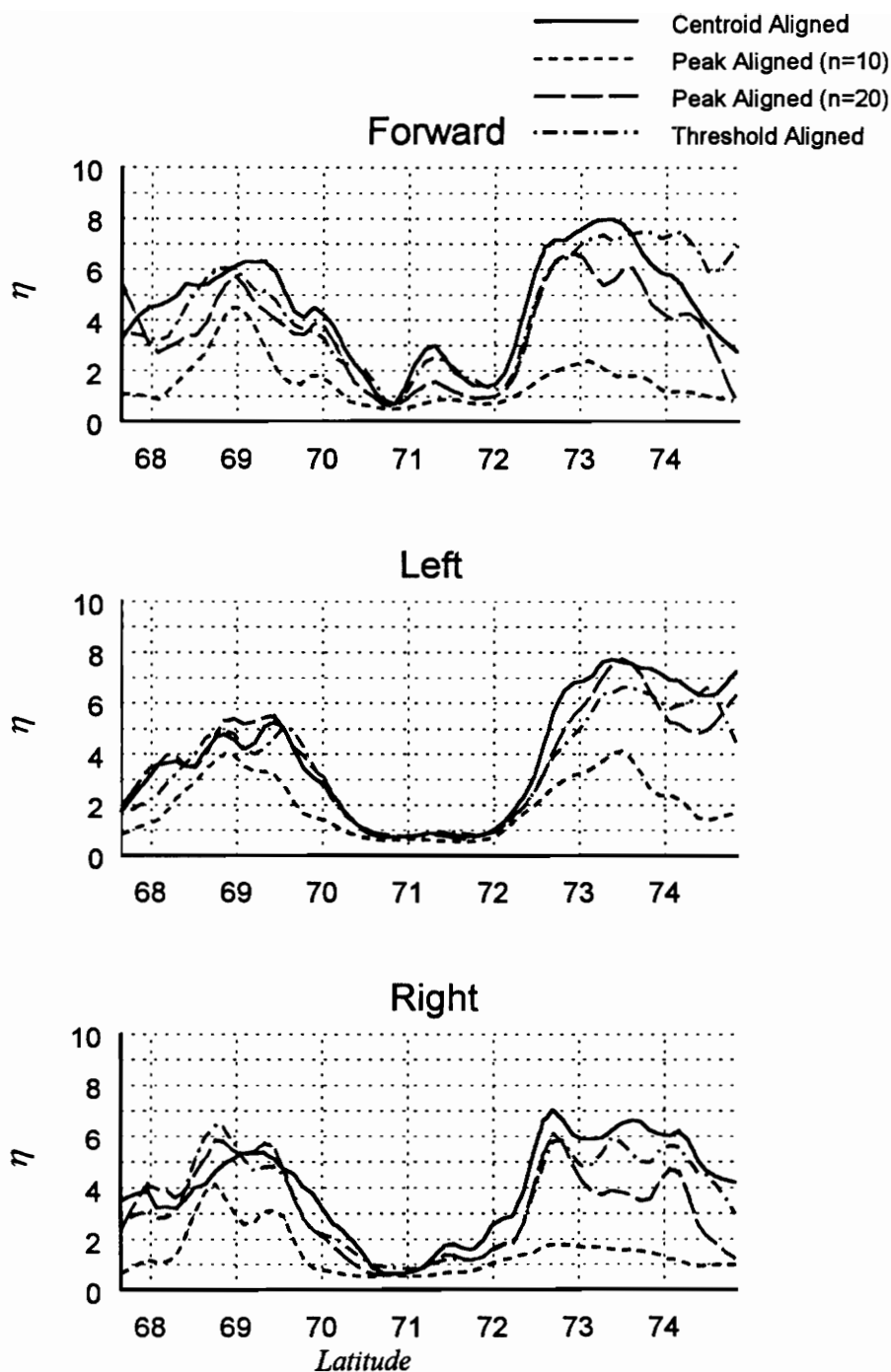


Figure 3.12. Volume/surface ratio estimates obtained using various alignment techniques. The threshold aligned data were aligned at the half-power point on the leading edge of the sub-average waveforms.

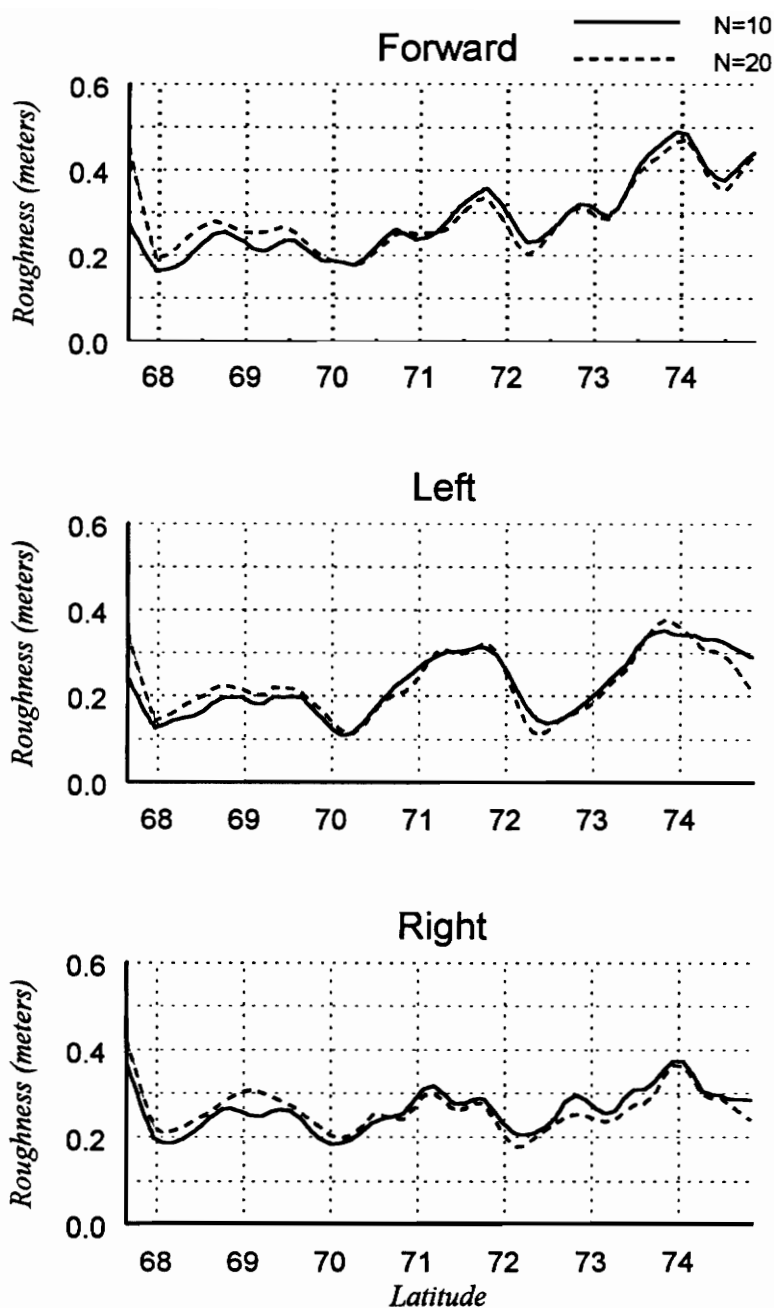


Figure 3.13. rms roughness for centroid aligned sub-average waveforms. The sub-average waveforms were obtained using 10 and 20 individual MARA pulses. Respective groups of 10 and 5 of these sub-average waveforms were averaged to obtain the data points in these figures. Each point is thus the average of 100 raw waveforms.

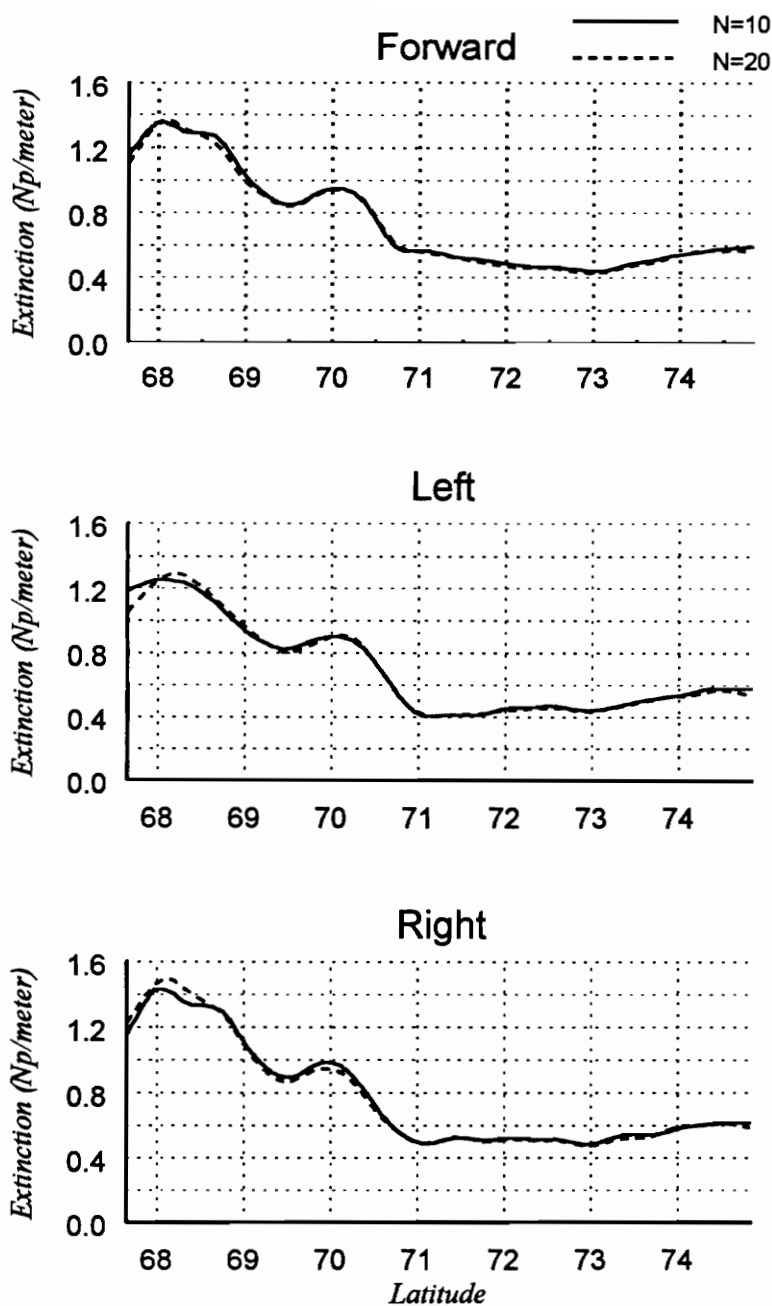


Figure 3.14. Extinction coefficient for centroid aligned sub-average waveforms. The sub-average waveforms were obtained using 10 and 20 individual MARA pulses. Respective groups of 10 and 5 of these sub-average waveforms were averaged to obtain the data points in these figures. Each point is thus the average of 100 raw waveforms.

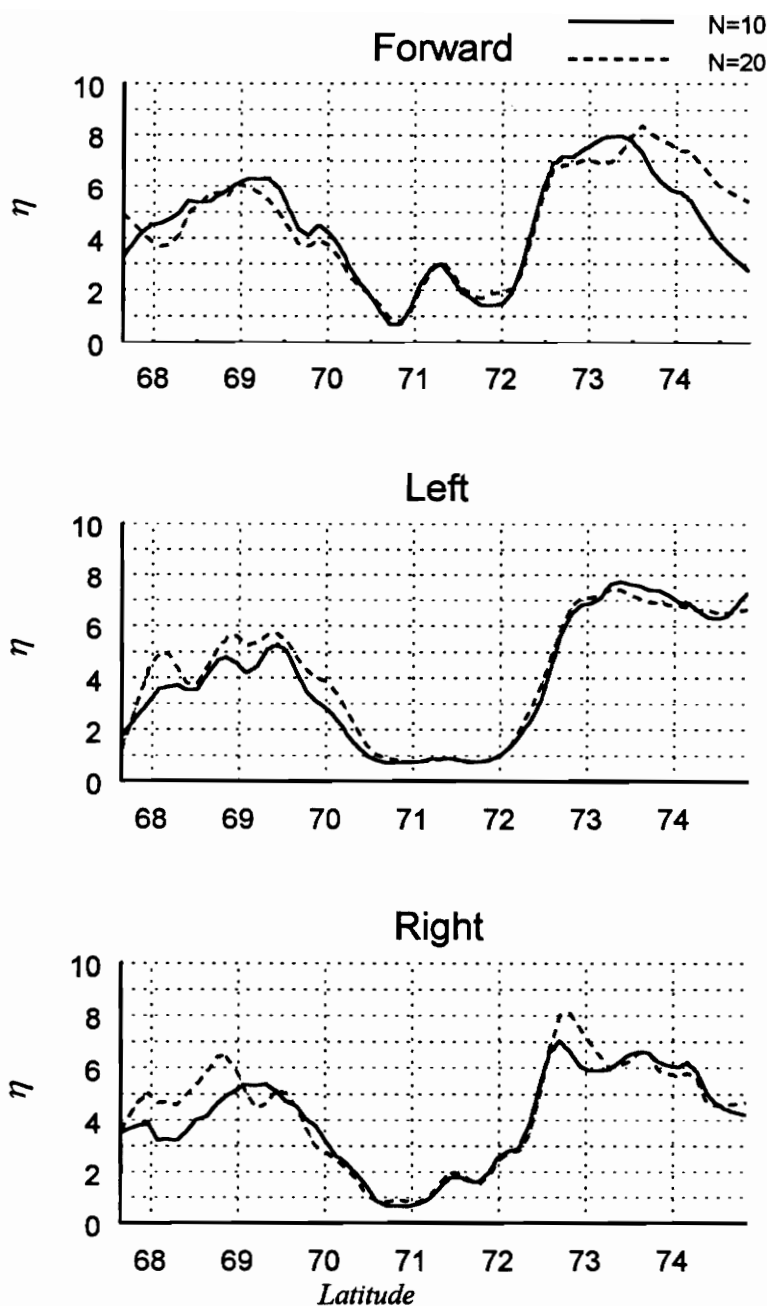


Figure 3.15. Volume/surface ratio for centroid aligned sub-average waveforms. The sub-average waveforms were obtained using 10 and 20 individual MARA pulses. Respective groups of 10 and 5 of these sub-average waveforms were averaged to obtain the data points in these figures. Each point is thus the average of 100 raw waveforms.

in the analysis of the MARA data. This is fortunate since it will be seen in Section 3.4 that k_e is a robust parameter which can be used to identify the various geophysical regions of the ice sheet.

Finally, the alignment problems discussed in this section can be avoided in future altimeter missions by increasing the radar's pulse repetition frequency (PRF) so that more pulses can be used to form the sub-average waveforms. The practical upper limit of the PRF is partially determined by the radar's need for decorrelated samples in the averaging process. If the incident pulses are transmitted so rapidly that the returns are strongly correlated, no new information is obtained.

An estimate of when pulses scattered from random surfaces are decorrelated can be obtained using the van Cittert-Zernike (VCZ) theorem [3]. This theorem states that the degree of coherence between two points in a plane in the far-field of a source is equal to the absolute value of the normalized Fourier transform of the intensity function of the source. Assuming a uniformly illuminated circular section of the ice sheet, the degree of coherence μ is

$$\mu = \text{abs} \left\{ \frac{2J_1(v)}{v} \right\} \quad (3-3)$$

where J_1 is a Bessel function of the first kind and order one and

$$v = \frac{2\pi\rho}{\lambda h} |P_1 - P_2| \quad (3-4)$$

where ρ is the diameter of the illuminated surface area, h is the height of the radar above the mean scattering surface and P_1 and P_2 are two points along the aircraft's flight line.

The first point of complete incoherence occurs when $\mu = 0$. This occurs for $v \approx 3.83$. Hence, two points along the radar's flight line are completely decorrelated when their separation satisfies

$$|P_1 - P_2| \approx \frac{3.83\lambda h}{2\pi\rho} \approx 0.61 \frac{\lambda h}{\rho} \quad (3-5)$$

Using MARA's two-way half power beamwidth for 12° off-nadir of 0.42° [24], an altitude of 500 meters and the corresponding illuminated radius of 1.92 meters, equation (3-5) predicts complete incoherence when the separation distance is 1.32 meters.

However, it has been noted that this value should be divided by two to account for the altimeter's two-way illumination path [34]. Using the aircraft's nominal velocity of 100 m/s this estimates the maximum PRF for complete decorrelation of returns to be 151 Hz.

For an incoherence factor of 0.5 between returns, the constant in equation (3-5) becomes 0.353 and the maximum PRF is then 261 Hz. This suggests for the MARA system that the ground track resolution of the altimeter could be increased by a factor of at least 2.6 while maintaining an incoherence factor of 0.5. Even higher PRF rates may be useful, however, since the VCZ theorem neglects certain factors which serve to decrease the decorrelation distance in altimeter applications. Foremost among these is that the volume component of the total backscattered waveform may decorrelate more quickly than the surface component. In this case it may be beneficial to increase the PRF above the maximum value predicted by the VCZ theorem.

This fact can be explained in the following manner. In order to accurately retrack the backscattered waveforms a good approximation to the average power waveform is needed. Assuming that the volume and surface components are independent, the variance in the approximation to the average power waveform is

$$\sigma_{t,N}^2(t) = \frac{\sigma_t^2(t)}{\sqrt{N}} = \frac{\sigma_s^2(t) + \sigma_v^2(t)}{\sqrt{N}} \quad (3-6)$$

where $\sigma_{t,N}^2$ is the variance in the power of the estimate of the average backscattered waveform obtained from N individual returns. σ_t^2 , σ_s^2 and σ_v^2 respectively represent the variance of the total waveform, and the surface and volume components of the total waveform. In determining the maximum PRF using the VCZ theorem, only the decorrelation distance for the surface scattered component was considered. However, since the volume component is scattered from a region which has random variations in all three dimensions, it is reasonable to postulate that the decorrelation distance for this component of the backscattered waveform will be smaller than the decorrelation distance for the surface component. Hence, increasing the PRF above the point at which the surface returns are decorrelated may provide a lower variance estimate of the total scattered waveform.

As an example consider the case in which the decorrelation distance for the volume scattered waveform approaches zero while the decorrelation distance for the surface component remains unchanged. For a sufficiently large PRF we then have

$$\sigma_{t,N}^2(t) \approx \frac{\sigma_s^2(t)}{\sqrt{N}} \quad (3-7)$$

where N is the number of decorrelation lengths along the ground track from which the returns are obtained. Thus, by increasing the PRF beyond the point where the surface returns are decorrelated, the variance of the received waveform is decreased. However, as indicated by (3-7), the variance approaches a limit below which it does not decrease. This floor is the variance in the surface component of the scattered waveform.

As a point of comparison the maximum useful PRF for the AAFE system is also considered here. The AAFE system is a pulsewidth limited altimeter with a beamwidth of 15° . The maximum useful PRF for this type of system has been determined to satisfy [8]

$$PRF_m = 4 \frac{V}{\lambda} \sqrt{\frac{c_o T}{h}} \quad (3-8)$$

where V is the velocity of the aircraft housing the altimeter, T is the transmitted pulsewidth, h is the height of the altimeter, λ is the carrier wavelength, and c_o is the speed of light in free space. Inserting the appropriate values for the AAFE system [15] the maximum PRF is found to be 25 kHz. This significantly larger value of the maximum PRF relative to the value obtained above for MARA is due to the significantly larger area illuminated by the AAFE altimeter.

This implies that a much higher surface resolution can be obtained with the AAFE system than with MARA due to AAFE's illumination of a much larger section of the ice sheet. Thus, the along track surface resolution of the ice sheet can be increased by using a larger beamwidth altimeter. This may be useful if more detailed topographic information on the ice sheet is desired.

3.4 Parameter Estimation

One of the primary goals of the research discussed in this report is the determination of the parameters which describe the scattering medium and its interface with free space. These parameters are the surface roughness σ_h , the effective volume extinction coefficient k_e , and the volume-to-surface peak amplitude ratio η . Before proceeding with an analysis of the parameter estimates derived from the MARA and AAFE data sets, however, a brief discussion of the parameter estimation scheme used in this process will be presented.

The method used to estimate the parameters from the scattering data is a straightforward, “brute-force” technique. In the combined scattering model, the surface and volume components of the scattered waveforms are assumed to be *separable*. That is, each is calculated independently of the other. The volume/surface ratio η determines the relative contributions of the volume component to the total scattered waveform. This separable nature of the scattering model, coupled with a new form of the volume scattered waveform model which is computationally inexpensive to evaluate, permit the use of a “brute-force” method to find the parameters that best fit the altimeter data. For this application, the “best fit” is defined as the combined waveform and parameters which yield the minimum of a function defining the error in fitting the model and parameters to average scattering data.

For the problem at hand, the function chosen to define this error is the cumulative square of the difference between the averaged altimeter data and the combined scattered waveform model. Mathematically, this function is

$$F(\sigma_h, k_e, \eta) = \frac{1}{N} \sum_{i=1}^N |D(\tau_i) - C(\tau_i; \sigma_h, k_e, \eta)|^2. \quad (3-9)$$

In this expression, $D(\tau_i)$ represents N discrete time values of the averaged waveform data that exceed some minimum threshold value. A threshold is used to avoid having the model forced to fit the data in regions which are inherently noisy. $C(\tau_i; \sigma_h, k_e, \eta)$ is a discrete time representation of the combined waveform model given in (2-64). The $1/N$ factor provides a normalization in the sense that the values of F can be compared independently of how many data points are used to compute (3-9). This is most important when comparing F values for different waveform shapes, such as those for nadir and off-nadir waveforms which can have a different number of sample points that exceed some threshold value.

The two functions $D(\tau_i)$ and $C(\tau_i; \sigma_h, k_e, \eta)$ must also be aligned before (3-9) can be computed. This must be done because the altimeter records the waveform samples within a range window that is not necessarily time-referenced to the same time as the waveform model. The range window is usually referenced to a threshold value on the waveform because of the use of a threshold tracker in the altimeter system. In general the relationship between the threshold value and absolute time is not directly known, especially for the off-nadir MARA returns. The alignment is instead done by simply searching through both the model and the data to find the time of their respective peaks.

The waveforms are then aligned by the time of their peaks and the function $F(\sigma_h, k_e, \eta)$ is computed. The waveform data comprise discrete points of a continuous curve, so quite often the peak value of the data does not coincide with the true peak of the waveform it represents. To circumvent this difficulty, the data is splined to find an estimated peak location and that value is used to align the model to the data. The function evaluation in (3-9) is done only with the original N data points and the corresponding values of the aligned model waveform.

The minimization algorithm that was used in this research is a brute-force search method. As the name implies, it is not an elegant algorithm, but a reliable global minimization technique is needed for the altimeter system discussed herein. This is in contrast to fitting techniques used by others in analyzing a similar problem for satellite altimeter platforms [10]. In the present case, the need for a robust global minimization algorithm arises because the specific configuration of the altimeter systems, as well as the effects of subsurface inhomogeneities on the average scattered waveform, create several local minima in the fitting procedure. While other global minimization algorithms are available (e.g., genetic algorithms), recent improvements to the volume scattering model have made the model numerically fast and the brute-force technique is a reasonable approach.

The brute-force technique consists of sampling the three-dimensional parameter space (σ_h, k_e, η) at appropriately spaced locations and comparing the corresponding model waveform to the average altimeter waveform using the function $F(\sigma_h, k_e, \eta)$ defined in equation (3-1). As the model parameters can theoretically assume values on the semi-infinite interval $[0, \infty)$, it is necessary to determine reasonable limits for these parameters in the optimization scheme.

For the roughness parameter σ_h , this was accomplished empirically by setting bounds on this parameter which included the range of values observed by others in studying the Greenland ice sheet [2,15]. The initial lower limit for the parameter k_e was similarly obtained and subsequently raised based on the analysis of a large number of radar returns. The upper limit for k_e , as well as the limits for η , were set at values beyond which the corresponding change to the model waveform was not significant. Using these bounds for the model parameters, the function $F(\sigma_h, k_e, \eta)$ was calculated at each point in the truncated parameter space. The coordinates of the minimum value of $F(\sigma_h, k_e, \eta)$ in the three-dimensional parameter space were taken to define the best-fit model waveform.

A total of approximately 10 million raw waveforms derived from data obtained on September 18, 19 and 20, 1991 by the MARA system were analyzed using the brute-force technique to obtain parameter estimates along the flight line shown in Figure 3.2. Approximately 60,000 raw⁸ waveforms obtained on September 18, 1991 by the AAFE system on the north-bound portion of the flight line were similarly analyzed. The following subsections provide an analysis of these parameter estimates, as well as a two frequency comparison of the scattering parameters derived from the 36 GHz MARA and 13.5 GHz AAFE data sets for September 18, 1991.

3.4.1 Analysis of North- vs. South-Bound MARA Parameter Estimates

Using altimeter data obtained from the MARA system on September 18, 19 and 20, 1991, the brute-force fitting scheme was used to obtain parameter estimates for the Greenland ice sheet. The filtered⁹ parameter estimates obtained on September 19, 1991 are shown in Figures 3.16-3.19¹⁰. Figure 3.16 shows the rms roughness σ_h in meters derived from the three working beams of the MARA system. Figure 3.17 displays the extinction coefficient k_e with units Nepers/meter. Figures 3.18 and 3.19 show the volume/surface ratio η and fit-error, respectively. The fit-error is the minimum value of the function $F(\sigma_h, k_e, \eta)$ determined for the best-fit parameter estimates. Each subplot in these figures contains approximately 12,000 points with each point being the result of fitting the new scattering model to the average of 100 raw waveforms.

The cyan colored parameter estimates in these figures were obtained by analyzing altimeter data recorded while heading north along the flight line shown in Figure 3.2. The magenta colored parameter estimates were obtained by analyzing data taken on the south-bound leg of the same flight after the turn at the top of the flight line. The north- and south-bound tracks of the flight were both determined using a GPS receiver and therefore presented the altimeter with approximately the same track along the ice sheet for both legs of the flight. Each figure contains three subplots titled "Forward", "Left" and "Right"

⁸Each "raw" AAFE waveform is actually the result of on-board averaging of approximately 64 individual returns [15].

⁹The best-fit parameters obtained using the brute-force fitting procedure were filtered with a 19-point sliding average filter to produce all parameter estimates in this report for both the AAFE and MARA systems.

¹⁰The parameters obtained for September 18 and 20 are similar to those obtained on September 19. All notable differences are discussed in Section 3.4.2.

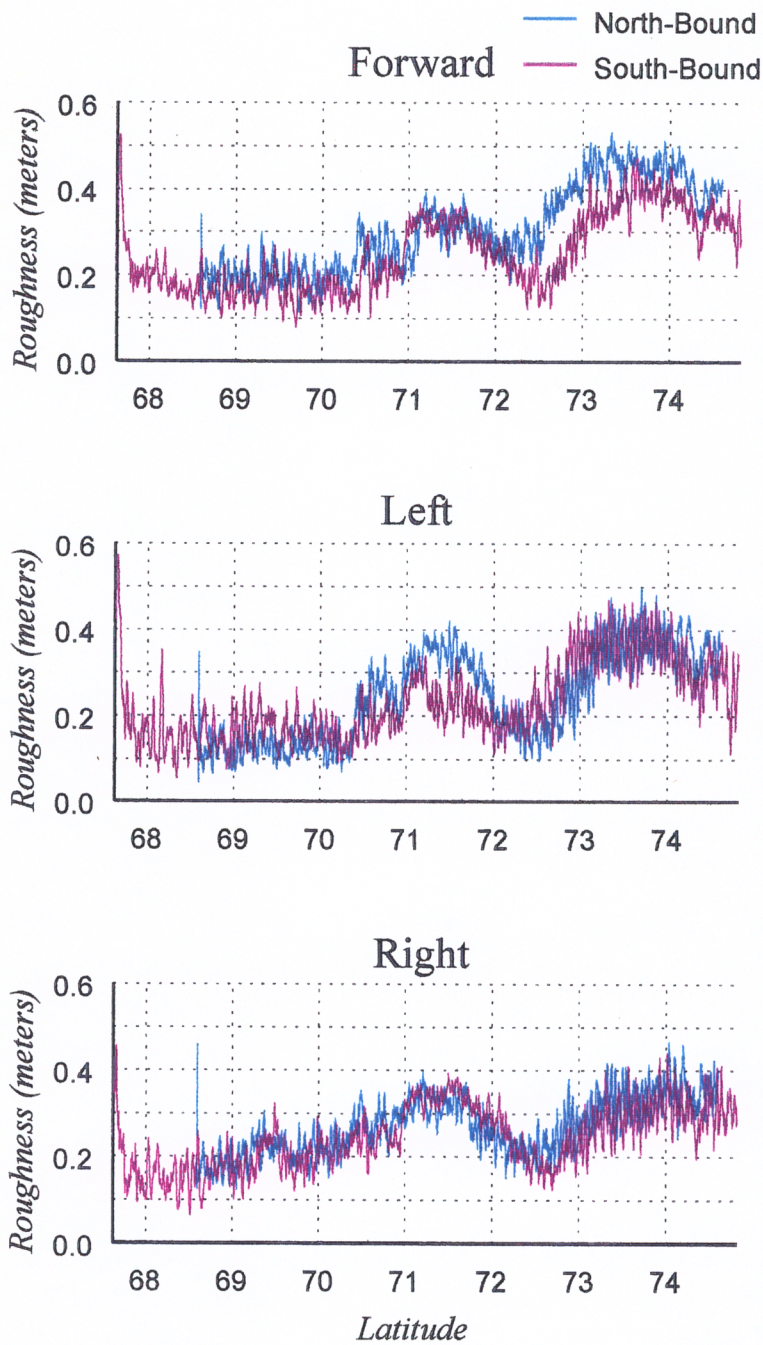


Figure 3.16. The rms surface roughness vs. latitude on September 19, 1991.

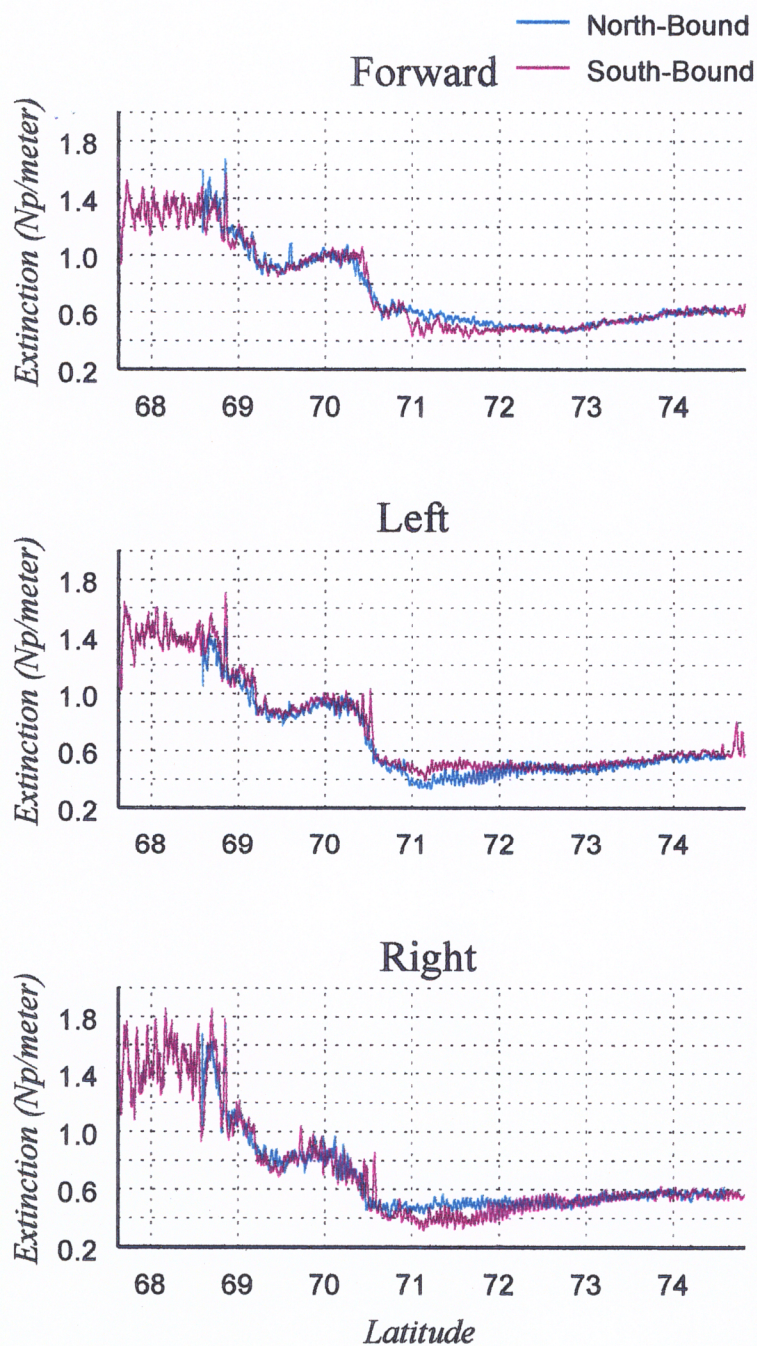


Figure 3.17. Extinction coefficient vs. latitude on September 19, 1991.

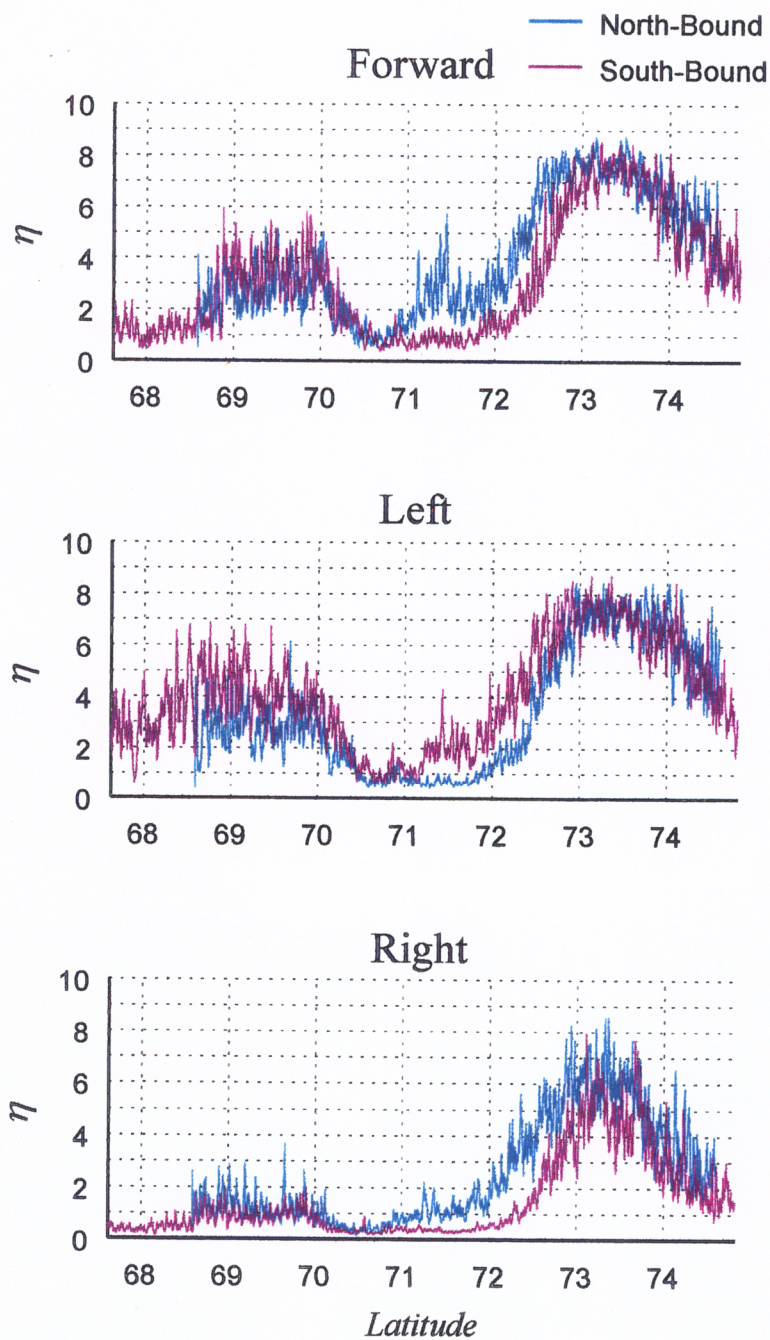


Figure 3.18. Volume/Surface ratio vs. latitude on September 19, 1991.

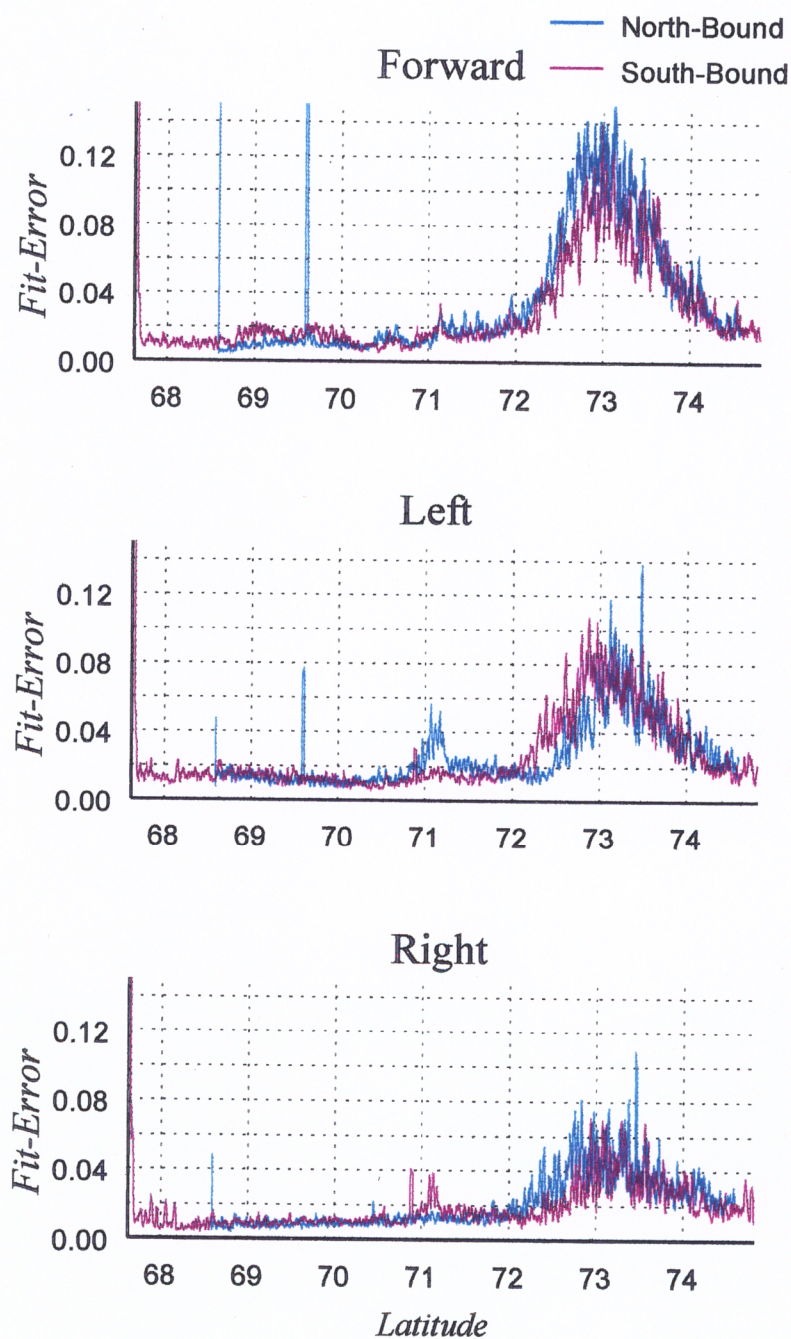


Figure 3.19. Fit-error vs. latitude on September 19, 1991.

corresponding to the three beams of the MARA system which produced useful data.

Several things are apparent from these figures. First, it is clear that while the three different beams of the altimeter display the same trends in the parameter estimates, the magnitudes of these estimates vary between the beams, particularly in Figures 3.18 and 3.19. This is not unexpected, however, since the MARA system was not properly calibrated and is known to have operated in a nonlinear portion of its detector characteristic [22]. These unquantifiable effects directly affect the parameter estimation process by distorting the shape of the average waveform which is used to derive the model fit.

As discussed in [22], the nonlinear input-to-output power relation was measured for only one of the detectors flown with the MARA system prior to operation over the Greenland ice sheet. This power relation was used to obtain the input power for all three of the MARA beams analyzed in this report. Thus, if the actual power relations varied between the beams, the resultant parameter estimates can also be expected to vary between the beams.

The following discussion contains analysis of the salient features of the parameter estimates and fit-error shown in these figures.

rms Surface Roughness, σ_h

In Figure 3.16 there are two regions for which the north- and south-bound parameter estimates are noticeably different. The first of these regions occurs in the forward beam between approximately 72°–74° latitude. This effect is explained by observing in Figure 3.19 that the fit-error is relatively large over this region. This suggests that the scattering model is not valid over this region of the ice sheet and that the derived parameter estimates are not accurate.

As an example of this, consider Figure 3.20. This figure shows three average scattered waveforms obtained from the MARA system over widely separated sections of the Greenland ice sheet, along with the best-fit waveforms derived using the fitting algorithm. Notice that for the waveforms from 68.2° and 74.6° latitude, the fit is so good that the model waveform cannot be easily distinguished from the average measured waveform. However, the fit to the waveform at 72.9° is not as good and the “bump” on the trailing edge of this waveform indicates that it was obtained over a region where the statistics of

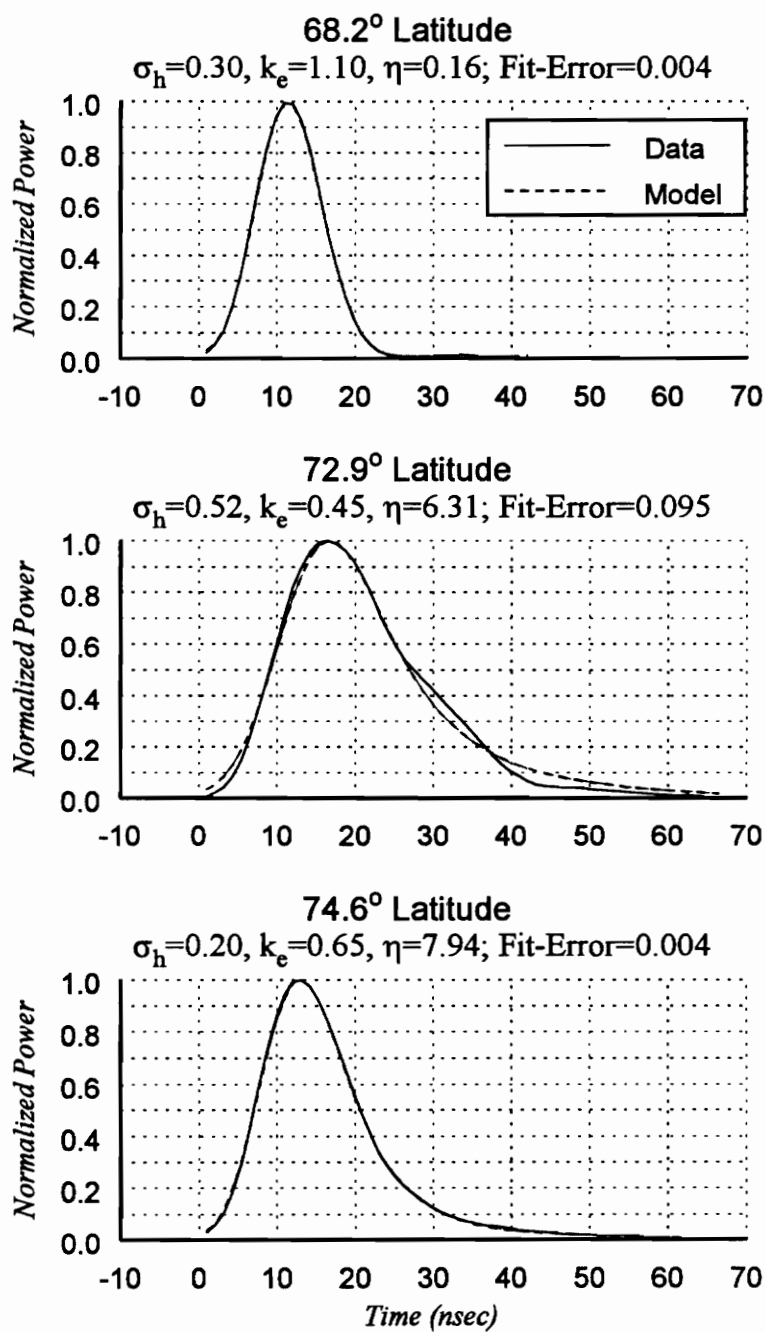


Figure 3.20. Examples of model fits to averaged MARA waveforms obtained from three different sections of the flight line shown in Figure 3.2.

the subsurface scattering mechanisms are nonhomogeneous – in violation of the assumptions of the homogeneous scattering model. This is not surprising since this waveform was obtained near the percolation facies of the ice sheet where inhomogeneous scattering effects are expected.

This in turn implies that the rms surface roughness estimate associated with the corresponding best-fit model waveform is not a valid indicator of the actual surface roughness. Instead, it is the value which produced the minimum value of the function (3-9) in a region where the homogeneous scattering model is a poor approximation to the actual scattering process. To analyze the scattering in these regions more accurately, and thus derive more realistic geophysical parameter estimates, it is necessary to employ a model which accounts for scattering from nonhomogeneous media. This will be the subject of future research.

The second region of Figure 3.16 for which the north- and south-bound flight lines produced significantly different roughness estimates is in the left beam between 71° – 72° latitude. The reason for this difference is not readily apparent and it is noted that the flights on September 18 and 20 did not exhibit this same difference between the north- and south-bound flight lines.

Extinction Coefficient, k_e

The extinction coefficient is shown versus latitude in Figure 3.17. The most outstanding features of this plot are the three different plateaus and associated transitions observed in the regions 67.7° – 69° , 69° – 70.5° , and 70.5° to the North end of the flight line by all three beams of the altimeter. It is well known that at 36 GHz the extinction coefficient for dry snow is dominated by scattering effects [30, p.1606]. Since the values of the extinction coefficient at 70.5° and 74.5° latitude are approximately equal and the ice sheet is known to consist of dry snow at 74.5° latitude on the flight line [2], it is reasonable to assume that the extinction coefficient from 70.5° to the top of the flight line is dominated by scattering effects (i.e., that absorption effects are small). This assumption is supported by the fact that the temperature at 72.6° N latitude, 38.5° W longitude was below -29°C on each of the three days being considered [33].

The larger extinction coefficient observed at the lower latitudes is thus due to either a change in the mean particle size or due to the presence of absorption effects in these lower

latitudes. As discussed in Section 3.4.2, it is expected that this larger extinction coefficient is primarily due to the presence of moisture in the near surface region of the ice sheet in the lower latitudes. This prevents the determination of differences in the average relative particle sizes between the various regions of the ice sheet. Such data would have to be obtained from altimeter flights during the colder part of the year when absorptive effects can be neglected over the entire ice sheet.

Also note that the maximum value of the extinction coefficient is approximately 1.6 m^{-1} in the lower latitudes where surface scattering is expected to dominate. This indicates a penetration depth of greater than 0.6 meters. As discussed below, this larger-than-expected value for the extinction coefficient is a result of the altimeter's inability to distinguish between surface and volume scattering contributions when the penetration depth is small.

Since it took the aircraft from approximately 12:30 p.m. to 4:30 p.m. (local time) to traverse the flight line on each of the three days considered here, it was thought that a temporal variation may be present in the parameter estimates due to diurnal temperature variations. From Figure 3.17 it is clear that the extinction coefficient on the north- and south-bound legs of the flight does not indicate such a dependence. Similar conclusions were drawn from the extinction coefficient estimates derived from the September 18 and 20 data sets.

Volume/Surface Ratio, η

The volume/surface scattering ratio is shown in Figure 3.18. The general trend in this parameter is as expected, showing a transition from surface scattering at the low latitudes to volume scattering in the upper latitudes. However, this trend is not monotonic as there are two regions between approximately 68.5° – 70° , and 72° – 74° latitude where the parameter increases significantly and then decreases. The first of these (68.5° – 70°) is discussed below in Section 3.4.2.

From a comparison with Figure 3.2, it is clear that the second significant fluctuation in η (72° – 74°) occurs well into the percolation facies of the ice sheet. Comparing Figure 3.18 with Figure 3.19, this second rapid change in the volume/surface ratio is seen to be concurrent with a similar fluctuation in the fit-error. Thus, the variation in the volume/surface ratio in this region does not necessarily indicate a rapid fluctuation in the volume scattering component of the scattered waveform. Rather, it is a manifestation of the fact that the scattering model is invalid in this area. Examples of average waveforms

from this region of the ice sheet are shown in Figure 3.21. The “bump” seen on the trailing edge of these waveforms is indicative of scattering from a nonhomogeneous volume. A similar effect has been observed in analyzing backscattered waveforms measured over the percolation facies by the AAFE system [15].

Finally, a peculiar anomaly occurs in Figure 3.18 from approximately 70.5° – 73° latitude. The forward and right beams of the MARA system indicate a smaller value of η on the south-bound leg of the flight than on the north-bound leg. This would seem to indicate a temporal dependence for this parameter. However, the left beam shows the opposite trend, with η larger on the south-bound leg than on the north-bound leg. This same phenomenon was observed in the parameter estimates for September 18 and 20. While an explanation cannot be absolutely determined, several factors indicate that this effect is due to a subsurface anisotropic scattering effect which is dependent on the slope of the ice sheet in this region.

First, it is important to observe that this phenomenon is not likely the result of climatic variations over the duration of the flight. As mentioned earlier, the temperature at 72.6° N latitude, 38.5° W longitude was below -29°C with no significant snowfall during the aircraft flight [33].

Furthermore, notice that the trends observed between the forward and right beams agree and are the opposite of the trend observed by the left beam of the altimeter. Since the aircraft is known to have been flying up the side of the glacier at an angle with the forward and right beams facing slightly uphill (downhill) and the left beam facing slightly downhill (uphill) on the north- (south-) bound leg of the flight line, it is suspected that the observed differences in the volume/surface ratio arise due to some type of an average, surface slope dependent, anisotropic arrangement of the subsurface scatterers in this region of the ice sheet.

This hypothesis is further supported by observing that this discrepancy between the north- and south-bound legs of the flight line disappears for latitudes near and above 73° latitude. As shown in Figure 3.4, the slope of the ice sheet gradually decreases to zero at 73° latitude, further suggesting that the north/south discrepancy is due to the effect of the surface slope on the scattering properties of the ice sheet. It is suspected that this effect is not observed in the lower latitudes where the surface slope is also large because the penetration depth in these latitudes is small.

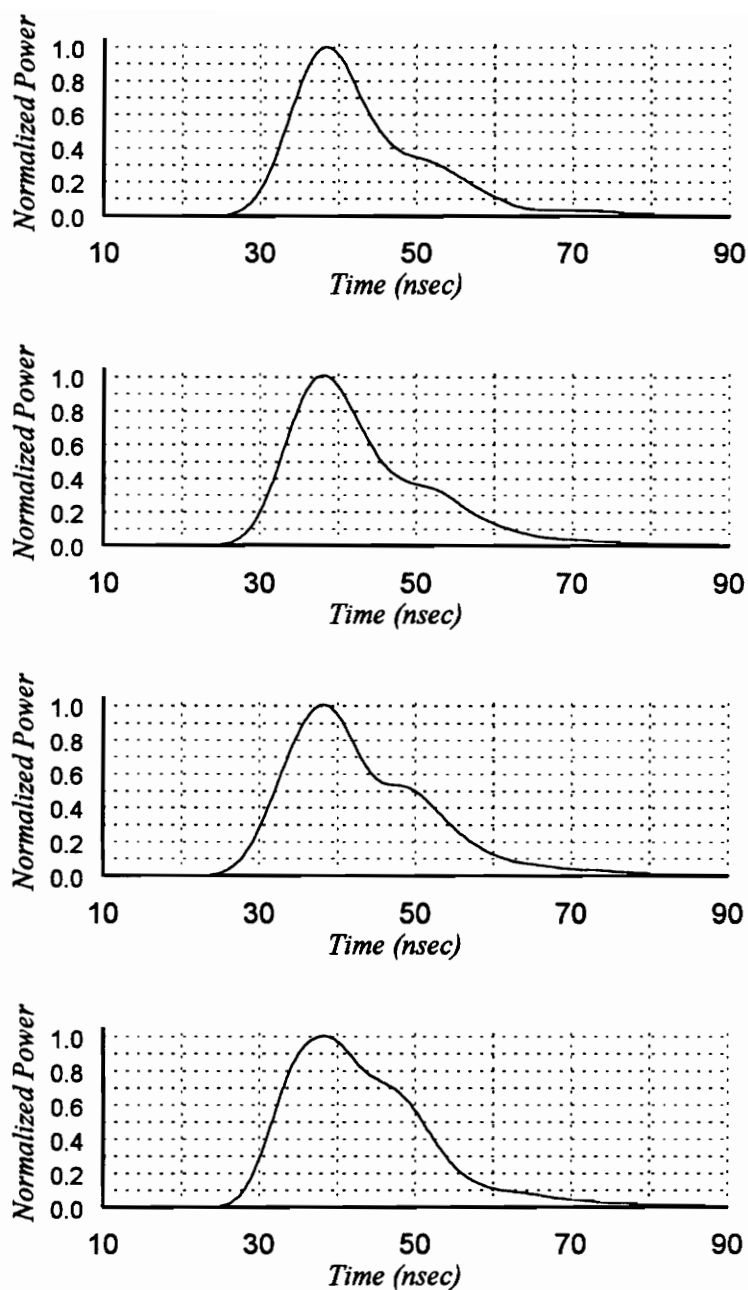


Figure 3.21. Average scattered waveforms recorded by MARA over the percolation zone. “Bumps” on the trailing edge indicate scattering from strong subsurface inhomogeneities.

Fit-Error

The fit-error is shown in Figure 3.19. As mentioned above, the fit-error is the value of the function which was minimized in an effort to obtain a best-fit of the scattering model to an average measured waveform. Thus, the relative magnitude of the fit-error provides an estimate of the validity of the scattering model in various regions of the ice sheet. This in turn indicates the validity of the parameters derived from the model. From the figure, it is clear that the scattering model provides a good approximation of the scattering process for the MARA system along the entire flight line except for the section from 72°–74° latitude. Typical fits to average scattered waveforms and the associated fit error are shown in Figure 3.20.

Several examples of average measured waveforms from this section of the flight line are shown in Figure 3.21. The “bumps” on the trailing edges of these waveforms are indicative of scattering from a nonhomogeneous volume, for which the homogeneous scattering model is not expected to produce good results. Although the scattering model is not valid in this region of the ice sheet, comparing these results with parameter estimates obtained from the AAFE system will be seen to provide information on the average location of these subsurface inhomogeneities (see Section 3.4.3).

At latitudes above approximately 74°, the fit-error approaches the values observed at the lower latitudes, indicating that the homogeneous scattering assumption is more adequate in this region of the ice sheet. This is expected since in the higher latitudes the air temperature is always below freezing and physical conditions rarely occur which are capable of producing strong subsurface inhomogeneities like those present in the percolation zone [2].

3.4.2 Analysis of Day-to-Day Variations in MARA Parameter Estimates

Figures 3.22-3.25 show the parameter estimates for September 18, 19 and 20 on the north-bound part of the flight trajectory shown in Figure 3.2. As noted above, the aircraft was guided by GPS-controlled auto pilot so that the ground track was repeated from day-to-day. In general, very good agreement is obtained in the parameter estimates for the three subsequent days, demonstrating the strong repeatability of the system and the potential for monitoring long-term variations in the properties of the ice sheet.

Figure 3.24 indicates a significant increase in the volume component of the scattered waveform from 68°–70.5° on September 19 and 20 relative to the flight of the previous

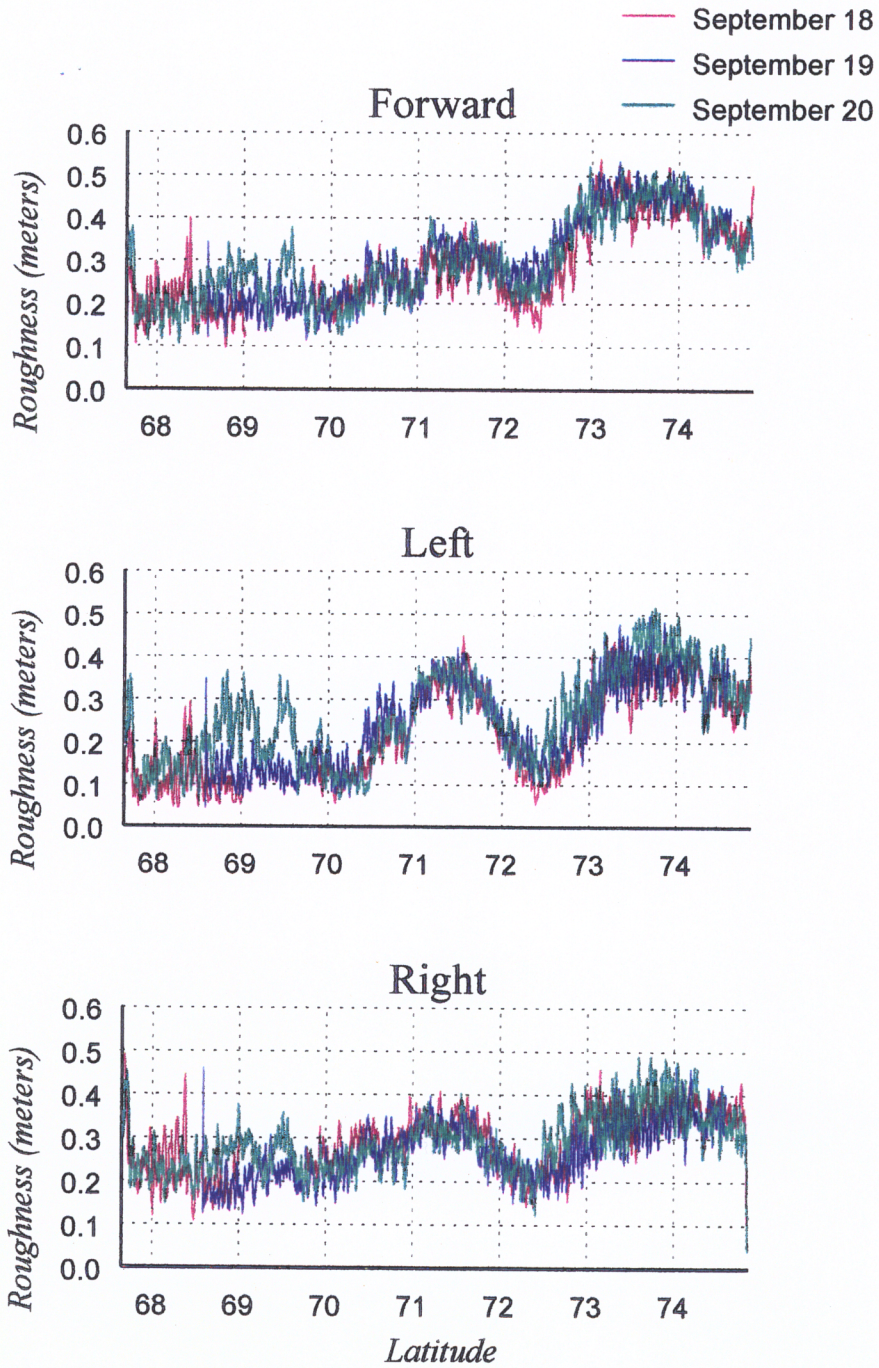


Figure 3.22. MARA rms surface roughness estimates on the north-bound leg of the flight line on September 18, 19 and 20, 1991.

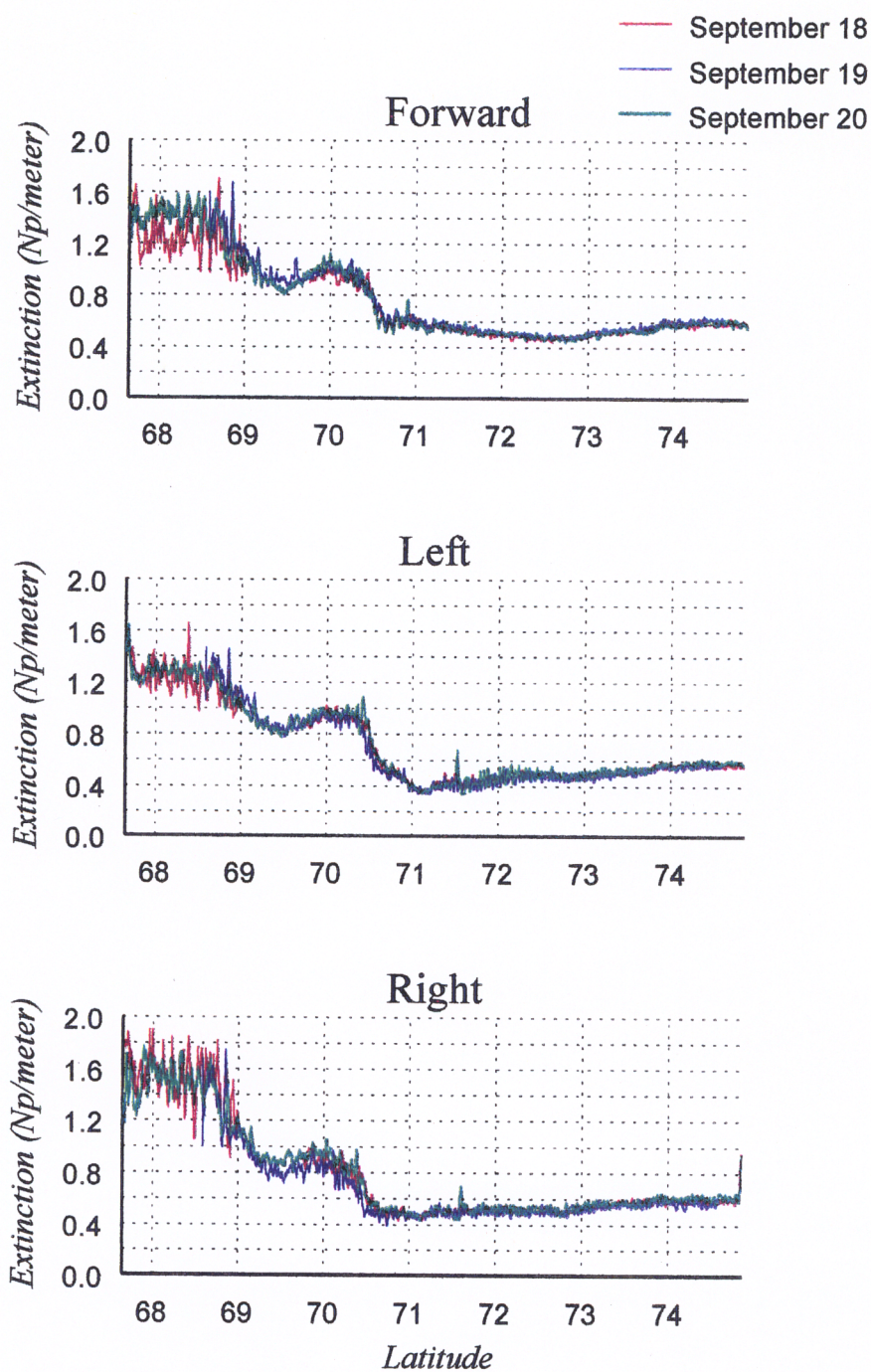


Figure 3.23. MARA extinction coefficient estimates on the north-bound leg of the flight line on September 18, 19 and 20, 1991.

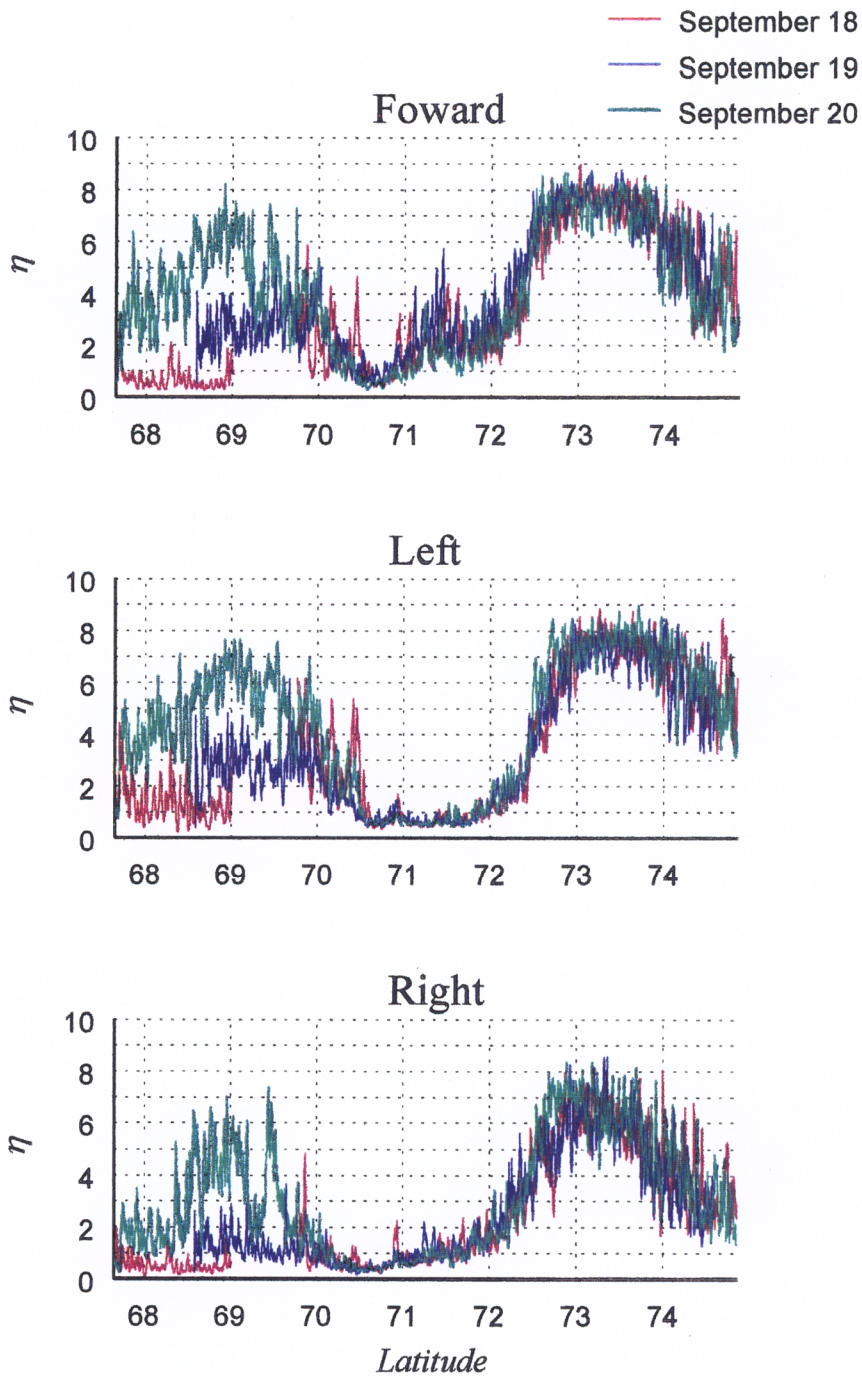


Figure 3.24. MARA volume/surface ratio estimates on the north-bound leg of the flight line on September 18, 19 and 20, 1991.

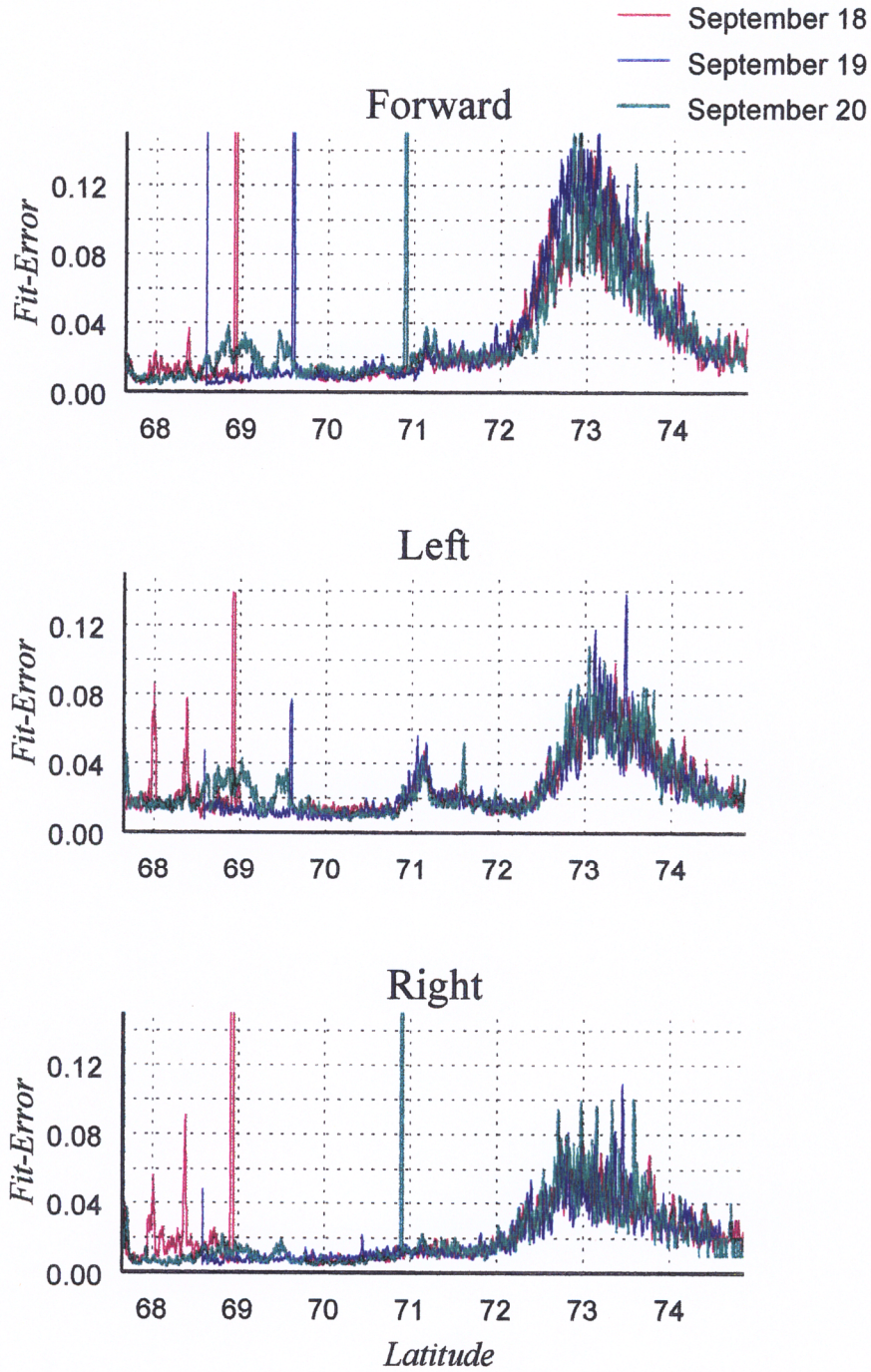


Figure 3.25. MARA fit-error on the north-bound leg of the flight line on September 18, 19 and 20, 1991.

day. Given the strong repeatability of the system over other regions of the flight line, this suggests that there was a change in the physical properties of the ice sheet in this region over these three days. Temperature readings taken at 72.6° N latitude, 38.5° W longitude were -29.6, -33.8 and -38.0 °C on September 18, 19 and 20, respectively [33]. While this location is more than 200 km from the observed change in η , these temperature readings corroborate the parameter estimates derived from the MARA altimeter system which indicate a physical change in the ice sheet during this period. Furthermore, since there was no significant snowfall during the aircraft flights on these three days [33], the observed increase in the volume scattered component of the received waveform in the lower latitudes is most likely due to a falling temperature on the ice sheet.

This hypothesis is further supported in that the boundary above which η did not vary is coincident with the boundary which separates the soaked and percolation facies of the ice sheet (70.5°N latitude). Since melting in the percolation region is generally restricted to localized percolation channels, the majority of the snow in this region remains at subfreezing temperatures. A falling temperature would therefore not be expected to significantly alter the scattering from this region of the ice sheet. However, the near surface region in the soaked and ablated facies of the ice sheet are characterized by significant amounts of moisture throughout so that a falling temperature could significantly affect volume scattering effects in this region of the ice sheet.

Although the estimates of η indicate a significant increase in volume scattering from September 18–20, the increase is larger than is expected to result from a reduction in temperature. In addition, on September 20 η is larger in this low latitude region than in the dry-snow region in the upper latitudes. This apparent anomaly results from the inability of the scattering model to separate surface and volume scattering effects in regions of the ice sheet where the penetration depth is small. As illustrated in Figure 3.26, when the extinction coefficient is small, the surface and volume scattered waveforms are easily distinguished. However, for larger values of k_e , the surface and volume components of the scattering model are not as easily distinguished.

Figure 3.27 contains representative examples of model waveforms obtained using the parameter estimates shown in Figures 3.22–3.24 for the 68°–70.5° section of the flight line being considered. From these figures it is clear that, although the parameter η changed significantly between the three days under consideration, the actual change in the shape of

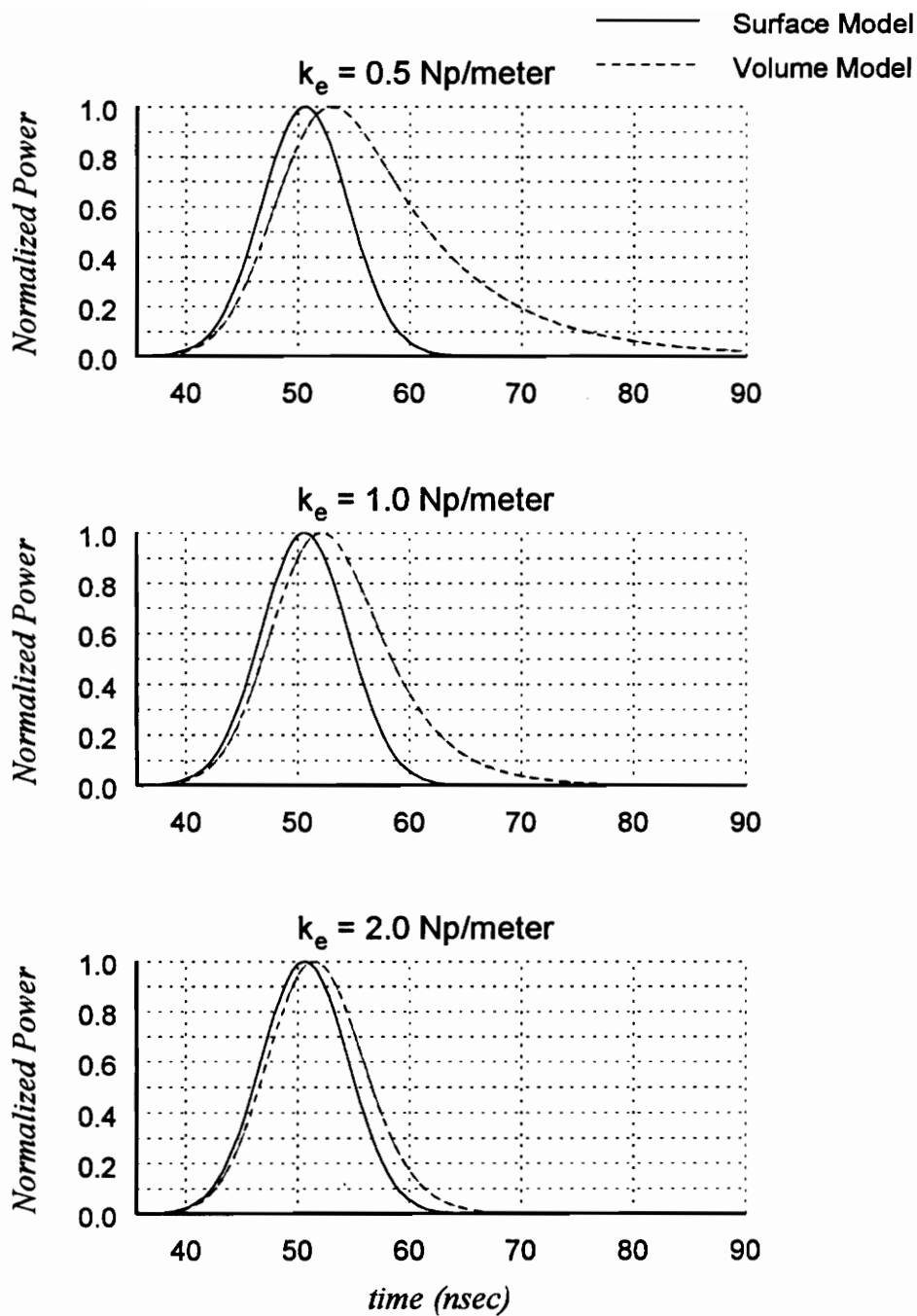


Figure 3.26. Modeled surface and volume waveforms. As the extinction coefficient increases the surface and volume scattered waveforms become more similar.

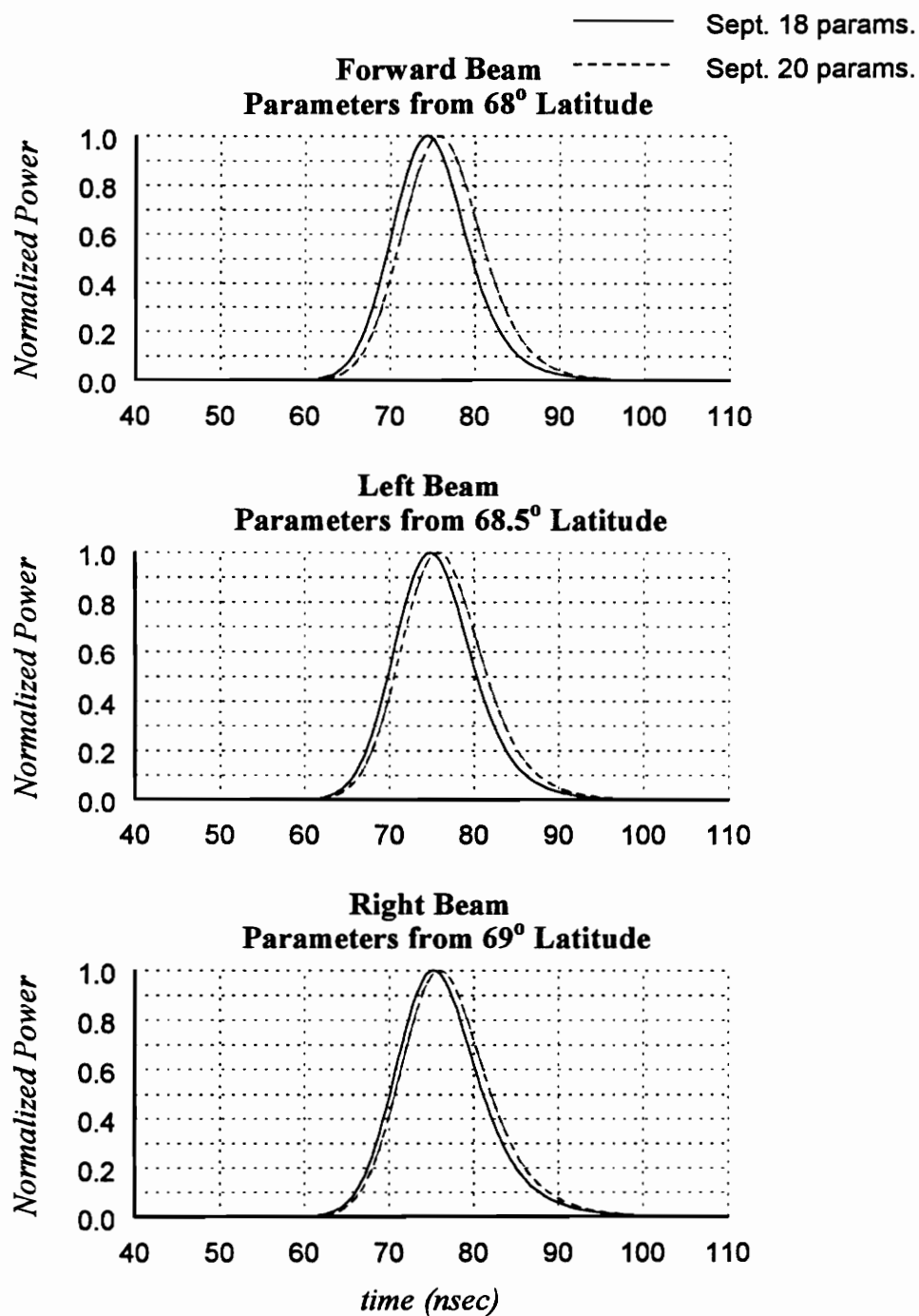


Figure 3.27. Comparison of best-fit model waveforms on September 18 and September 20.

the model waveforms is small. This in turn implies that the change in the shape of the average scattered waveform was also small, as illustrated in Figure 3.28.

Thus, although there was a physical change in the scattering properties of the ice sheet from September 18–20 which most likely was the result of a decrease in the moisture content of the ice sheet due to a falling temperature, the scattering model overestimates the change in the parameter η . This occurs because the model is insensitive to changes in this parameter when the volume scattering effects are confined to regions near the air/snow interface (i.e., when k_e is large). Small changes in the average scattered waveform caused by scattering effects not included in the model can therefore produce large, misleading changes in the volume/surface scattering ratio η .

Although not able to easily distinguish surface and volume effects in this region, the scattering model still provides useful information about the ice sheet. First observe that the model is able to identify the surface roughness on all three days. This is due to the inclusion of surface roughness in the volume component of the new scattering model. Also observe that the extinction coefficient remains relatively unchanged over the three days being considered while the volume scattered contribution to the composite waveform increases. This suggests that the extinction coefficient is a robust parameter which can be used to identify the various geophysical regions of the ice sheet independently of day-to-day changes in the ice sheet resulting from temperature changes.

Also note that although the value of the parameter η is inaccurate in the lower latitude regions of the ice sheet, the altimeter system is quite sensitive to changes in the surface of the ice sheet which give rise to increased volume scattering effects. This is in spite of the fact that these physical changes in the ice sheet produce only a small change in the average scattered waveform.

3.4.3 Two Frequency Comparison: MARA and AAFE

A plot of the parameters σ , k_e and η along with the fit-error derived from data obtained over the Greenland ice sheet by the AAFE altimeter on the north-bound leg of the flight on September 18, 1991 is shown in Figure 3.29¹¹. Figures 3.30–3.33 contain comparisons of the AAFE and MARA derived parameter estimates for the same day. This two frequency comparison provides a unique look at the scattering properties of the ice sheet in that the MARA and AAFE systems operated at significantly different frequencies

¹¹All AAFE data analyzed in this report was averaged using the half-power alignment technique discussed in Section 3.3.

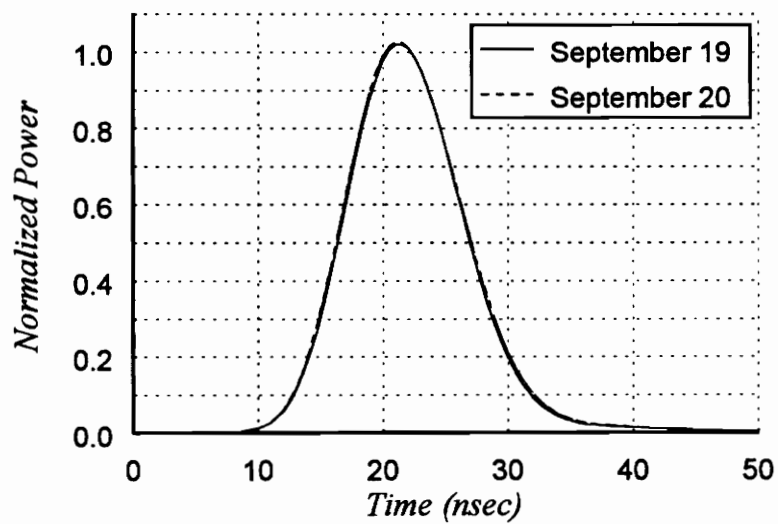
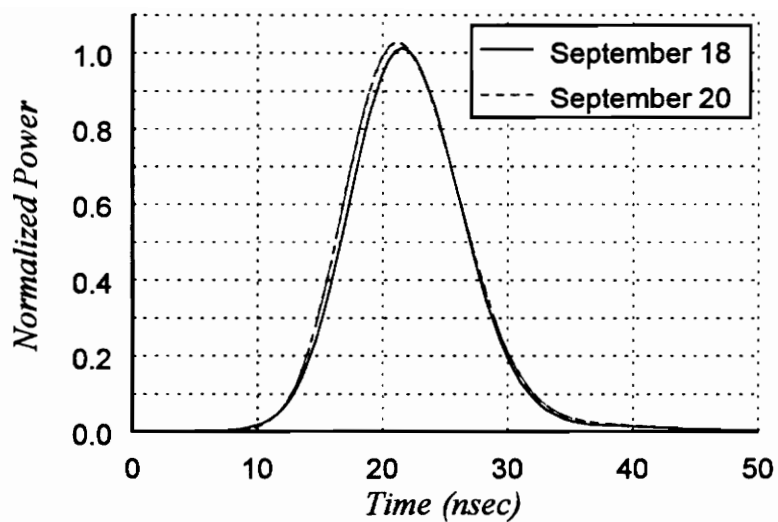


Figure 3.28. Comparison of average scattered waveforms. These waveforms were obtained by averaging all right beam data from 67.7° – 69° on each of the three days considered.

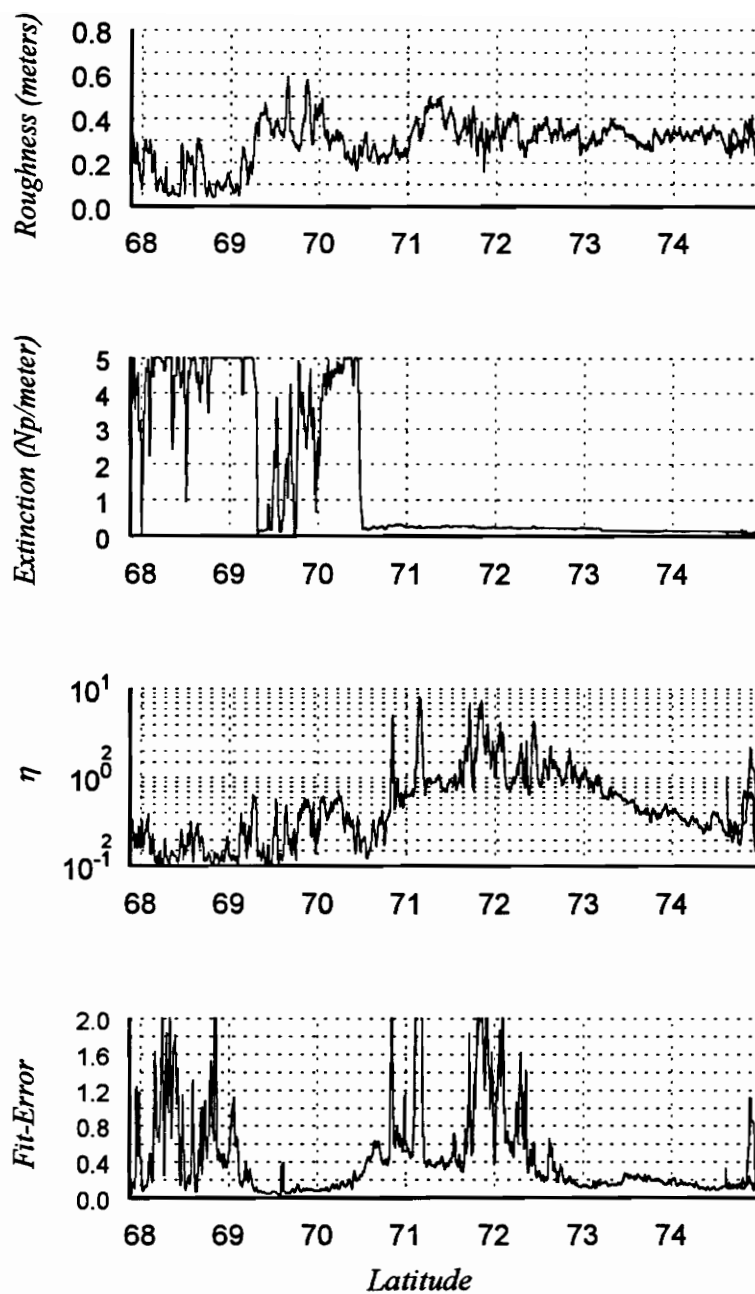


Figure 3.29. Parameter estimates for data obtained by the AAFE system on September 18, 1991 over the Greenland ice sheet.

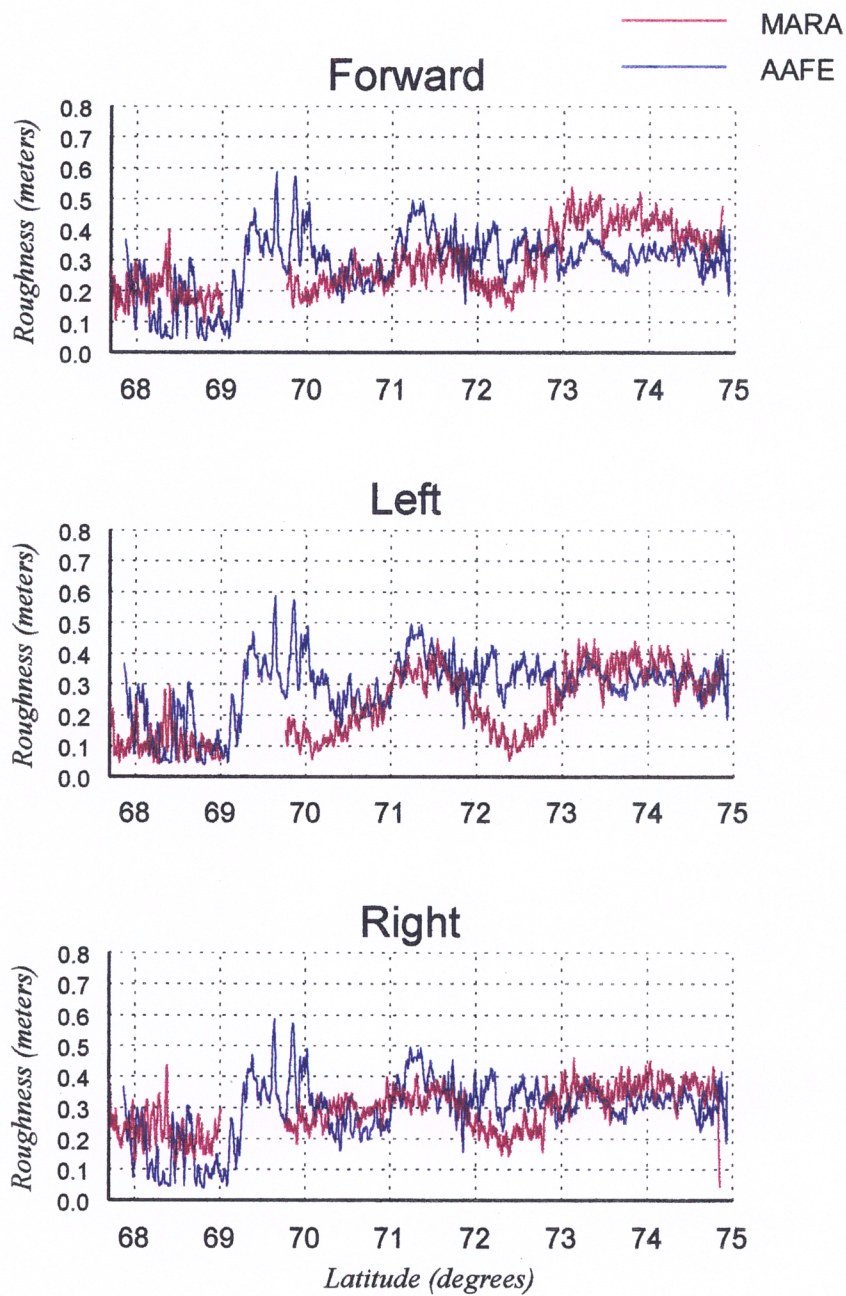


Figure 3.30. Comparison of rms surface roughness estimates derived from data obtained by the MARA and AAFE altimeters on September 18, 1991.

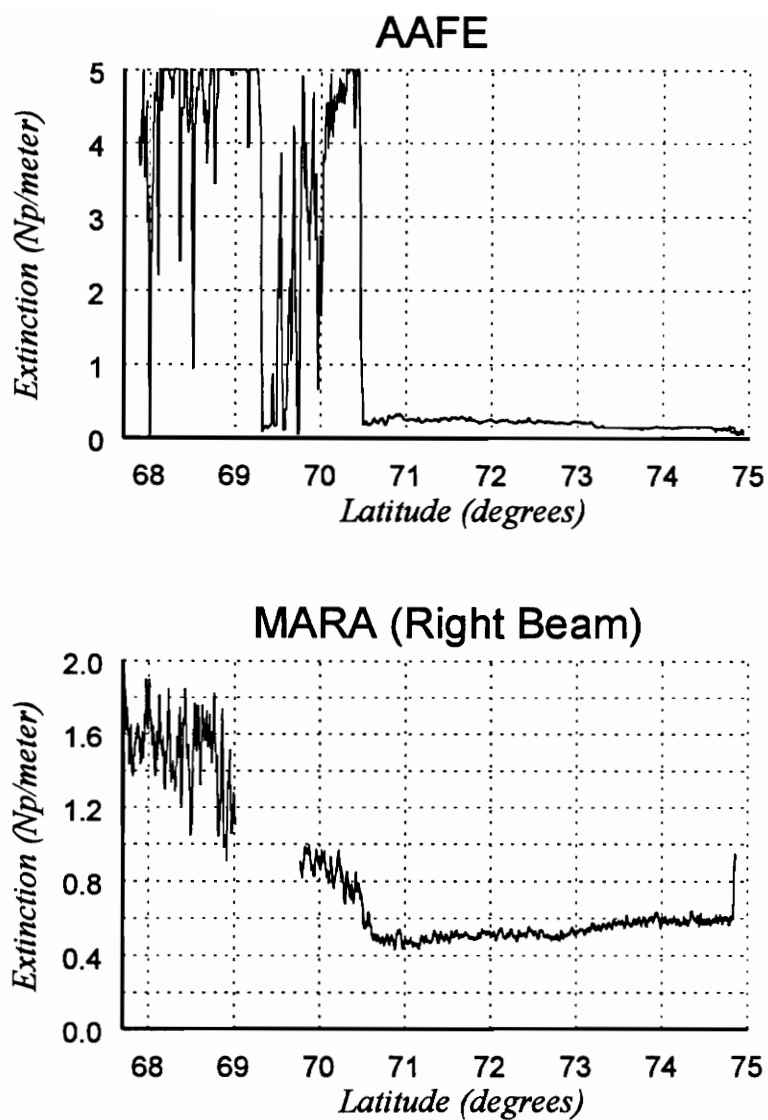


Figure 3.31. Comparison of extinction coefficient estimates derived from data obtained by the MARA and AAFE altimeters on September 18, 1991.

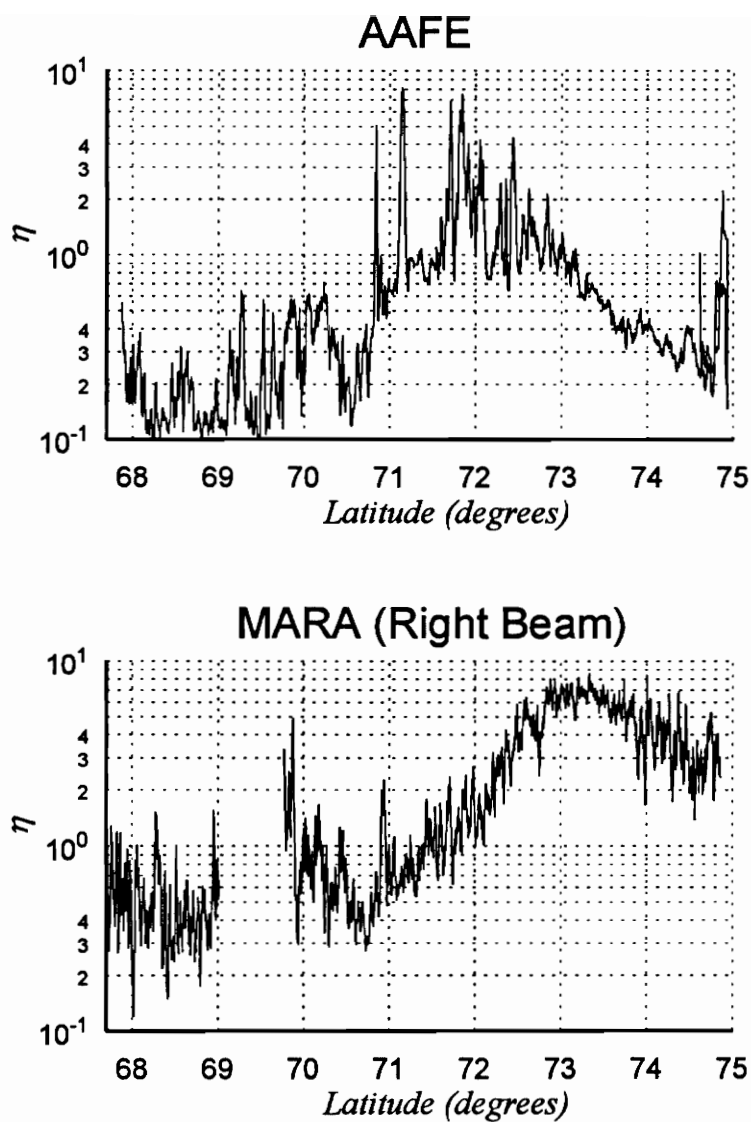


Figure 3.32. Comparison of volume/surface ratio estimates derived from data obtained by the MARA and AAFE altimeters on September 18, 1991.

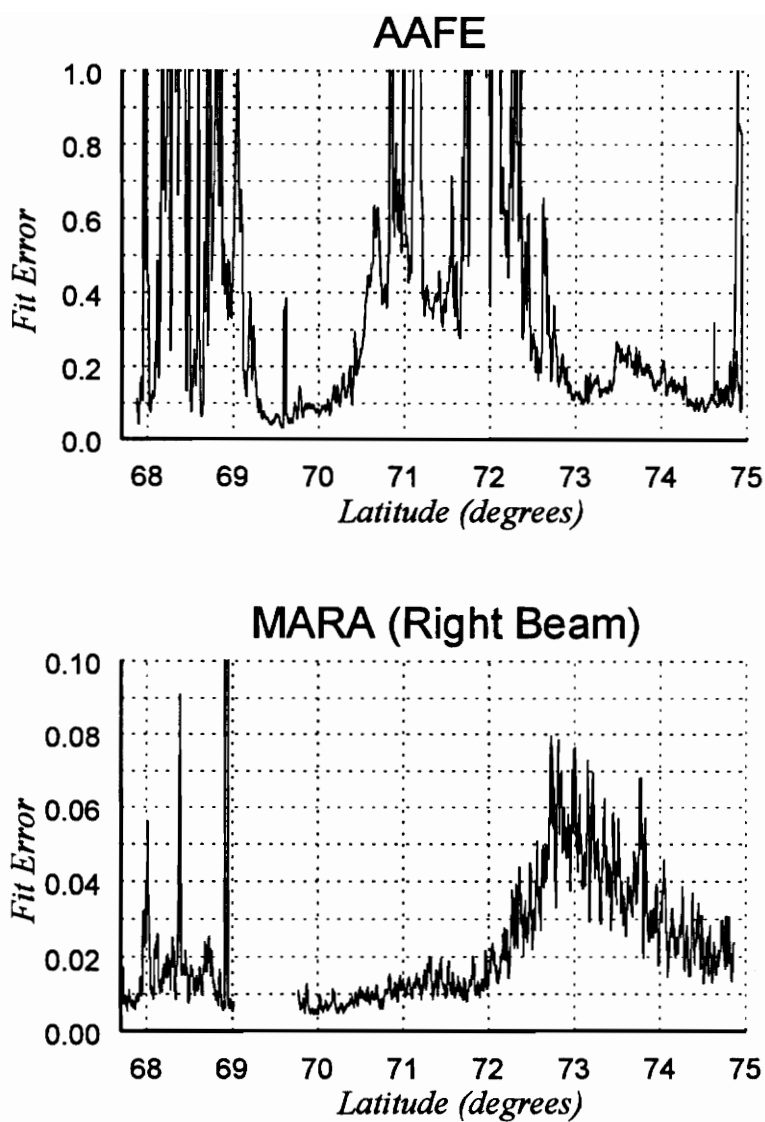


Figure 3.33. Comparison of fit-error obtained in fitting composite scattering model to data obtained by the MARA and AAFE altimeters on September 18, 1991.

from the same aircraft platform.

An example of the difference in the scattering responses of the two systems is illustrated in Figure 3.34. The average scattered waveforms in this figure were recorded by both systems on September 18 in the percolation zone at 71.43° latitude. From the figure it is clear that the AAFE system is significantly more sensitive to subsurface scattering effects than the MARA system. While this enables the 13.9 GHz AAFE to observe subsurface features of the ice sheet more readily than the 36 GHz MARA, it also makes application of the homogeneous scattering model less valid for analyzing the AAFE data set. This fact is manifested in the significantly larger values of the fit-error which result for the AAFE system as compared to the MARA system (Figure 3.33). Furthermore, the AAFE altimeter is probably too sensitive to subsurface features if topographic measurements are what is really desired.

rms Surface Roughness: A Frequency Independent Parameter

Figure 3.30 shows a plot of the surface roughness parameter derived from the MARA and AAFE systems on the north-bound leg of the September 18 flight. The break in the MARA data between 69°–69.8° is the result of a calibration performed on the radar. While the other parameters derived from the scattering model (k_e and η) are known to be frequency dependent, the rms roughness is a physical parameter which should be independent of the observation frequency (provided that the quasi-specular scattering assumption of the surface model is valid for both systems). However, several factors prevent such a direct comparison of the AAFE and MARA estimates of the rms surface roughness.

Foremost is the fact that the footprint of the AAFE system is over 26 times wider than the corresponding footprint of the MARA system (Table 3.1). The AAFE system is capable of measuring surface roughness features with wavelengths on the order of 130 meters while the MARA system is only sensitive to those surface features which occur on a scale of 5 meters or less. In addition, reliable data is only available for the off-nadir MARA beams while AAFE is a nadir-directed system. The small roughness values observed over the ice sheet, in addition to the lack of calibration of the altimeters over a well-known scattering surface such as the ocean, also calls into question the absolute accuracy of the actual roughness values obtained from these systems.

Finally, the limited portions of the flight line for which the homogeneous scattering model is valid for the AAFE system (due to its large penetration depth) provides a limited

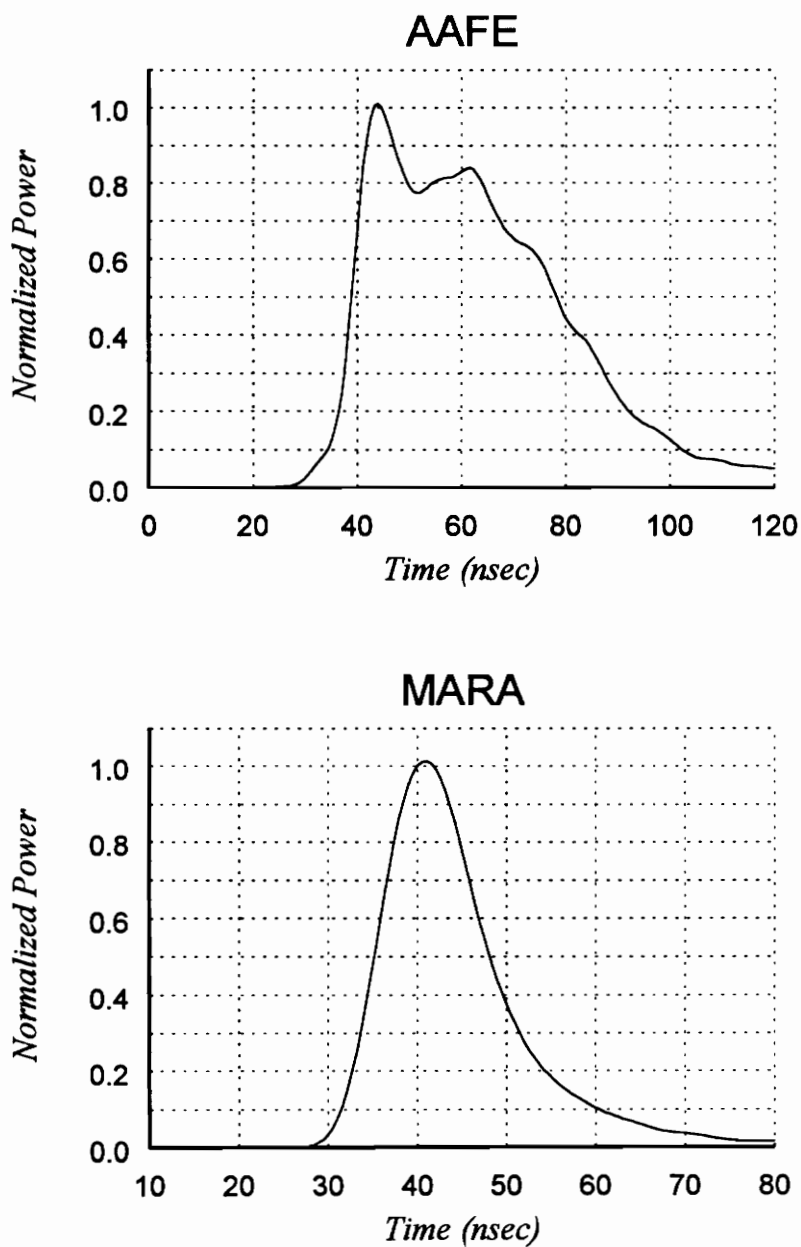


Figure 3.34. Averaged MARA and AAFE waveforms at 71.43° . The effect of strong subsurface scatterers is clear in the AAFE waveform but is not apparent in the MARA waveform.

region where roughness comparisons can be made. From the fit-error values for both systems shown in Figure 3.33, the overlapping regions for which the scattering model developed in Section 2.3 best models the scattered waveforms for both systems occurs from approximately 69°–70.5° and from 74° to the north end of the flight line. In the 69°–70.5° region it is apparent that the AAFE system observed a somewhat larger surface roughness than the MARA system, indicating the presence of large-scale surface roughness features in this region. In the dry snow region extending from 74° to the end of the flight line, both systems see approximately the same surface roughness. This implies that the majority of the surface roughness features in the upper latitude portions of the flight line have wavelengths on the order of five meters while larger wavelength surface roughness features are present in the lower latitudes.

Frequency Dependent Parameters: k_e and η

While the small rms surface roughness coupled with system differences prevents a definitive comparison of the values of σ_h between the two systems, the widely separated frequencies of the two systems provides a unique comparison of the volume scattering properties of the ice sheet as seen by the two altimeters.

Figures 3.31–33 respectively contain plots of the extinction coefficient, volume/surface ratio and fit-error for the two systems on the north-bound leg of the flight line on September 18, 1991. By comparing these plots it is possible to define four electromagnetically distinct regions of the ice sheet as observed by the MARA and AAFE altimeters. An attempt has been made to correlate these regions of the ice sheet to those defined in [2] and illustrated in Figure 3.2. Unfortunately, no ground truth is available for the three days of observation and the association of the different scattering regions observed by the altimeters to physical regions of the ice sheet is only approximate.

This does not imply that the instruments are unable to definitively identify various regions of the ice sheet. Rather, it cannot be absolutely determined if the distinct borders between the various regions as observed by the altimeters correspond to those boundaries derived from pit studies of the ice sheet. This is particularly true in the soaked and ablated regions of the ice sheet. While it is known that the scattering in this region is dominated by surface scattering effects, the limited knowledge of the surface properties in this region of the ice sheet prevents direct association of changes in the average scattered waveforms to changes in geographic location. For this reason the electromagnetically distinguished portions of the flight line, which are dominated by surface scattering and labeled *Region 1*

and *Region 2* below, have not been associated with the particular facies of the ice sheet where surface scattering is expected to dominate (i.e., the soaked and ablation facies).

Region 1 (67.8°–69°)

From Figures 3.30–3.33, as well as Figures 3.16–3.19, it is apparent that this region is easily distinguished from other portions of the flight line by the MARA system. Scattering from region 1 is seen to be characterized by large values of extinction and small volume/surface ratios, indicating a dominance of the surface scattering component of the scattered waveform.

For the AAFE system, this region is distinguished from others by large extinction values concurrent with large values of the fit-error derived from the parameter estimation scheme. This implies that the surface scattering model is not valid in region 1 for the AAFE system. This is in contrast to the MARA system for which the fit-error is seen to be similar to the fit-error obtained for other regions of the ice sheet. This difference is likely due to the different beamwidths of the two systems (0.6° for MARA, 15.6° for AAFE) and the possible presence of large rms surface slopes in this region. However, the absence of ground truth precludes a definitive determination of the cause of this discrepancy.

Finally, Figure 3.35 contains a plot of the peak received power observed by these two systems along the flight line (the MARA data in this plot has been taken from September 19 due to the hole in the MARA data resulting from radar calibration on September 18). From this figure it can be seen that region 1 of the ice sheet is further distinguishable from the other portions of the flight line by the peak received power for the MARA system.

Region 2 (69°–70.5°)

For both MARA and AAFE this region is distinguished from region 1 by an increase in the volume scattered component of the average waveform relative to scattering in region 1. It is further distinguished for the MARA system by a plateau in the extinction coefficient between the abrupt changes at 69° and 70.5° latitude as well as by an increase in the peak scattered power shown in Figure 3.35. Notice also that the fit-error for both altimeters is small in this region, indicating the validity of the scattering model in this region of the ice sheet.

As discussed in Section 3.4.2, region 1 and region 2 are the sections of the flight line over which the volume scattered component of the received waveform was observed to

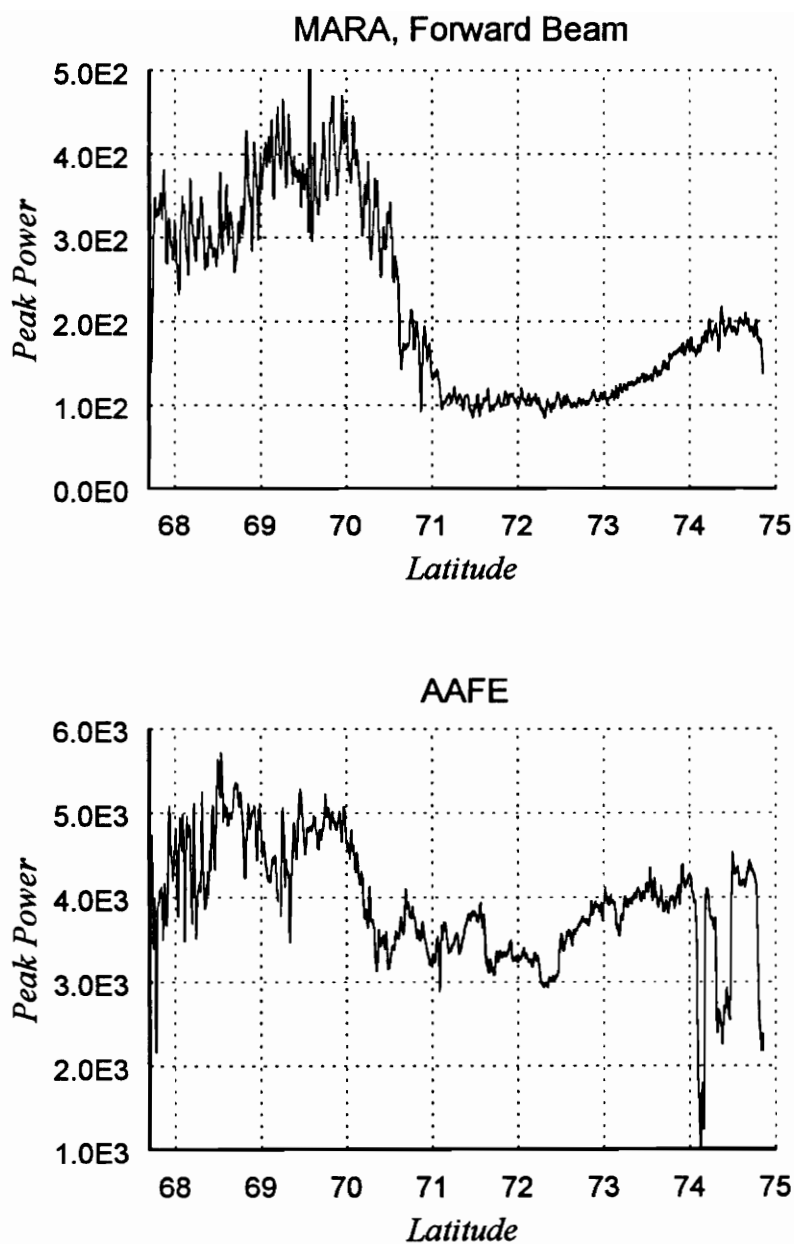


Figure 3.35. Peak power observed along the flight line for the MARA and AAFE altimeters. The MARA data is from September 19 while the AAFE data is from September 18, 1991.

increase from September 18 to September 20 for the MARA system. The higher latitude portions of the flight line did not exhibit any measurable variations in scattering properties from September 18–20. This is consistent with the parameters derived from both the AAFE and MARA systems which indicate a rapid transition in the physical properties of the ice sheet at 70.5° latitude.

Percolation Zone (70.5°–73°)

As discussed in Section 3.1, scattering in this region of the ice sheet is expected to deviate significantly from that predicted by the homogeneous model due to the presence of strong subsurface scatterers. It has been observed that these scatterers cause the brute-force minimization scheme to produce large values of the volume/surface ratio η concurrent with large values of the fit-error. While the presence of these strong subsurface scatterers significantly increases the fraction of received energy attributable to volume scattering, the inability of the homogeneous volume scattering model to account for these effects prevents the derivation of quantifiable estimates of the magnitude of the volume scattering process in this region.

Although the AAFE and MARA systems are individually able to identify a section of the flight line which behaves like the percolation zone, the location of the regions thus identified are frequency dependent and demonstrate the importance of considering the frequency dependence of the sensors in interpreting scattering data. With a knowledge of these frequency dependent effects it will be demonstrated that it is possible to infer the subsurface characteristics of the ice sheet in this region where the homogeneous scattering model is not valid.

As shown in Figure 3.32, the volume/surface ratio η for AAFE appears to significantly increase to a peak near 72° latitude and subsequently decrease. However, as discussed above for the MARA system, by comparing the plot of η with the fit-error shown in Figure 3.33, it is clear that the change in η is concurrent with an increase in the fit-error, indicating that the scattering model is not valid over this region of the ice sheet. This is illustrated in Figure 3.36 where the average scattered waveforms from 70.16°–70.74° are shown. The transition from surface to volume scattering is evident in the trailing edge of these scattered waveforms. Due to the inability of the homogeneous scattering model to account for these effects the fit-error increases significantly over this region.

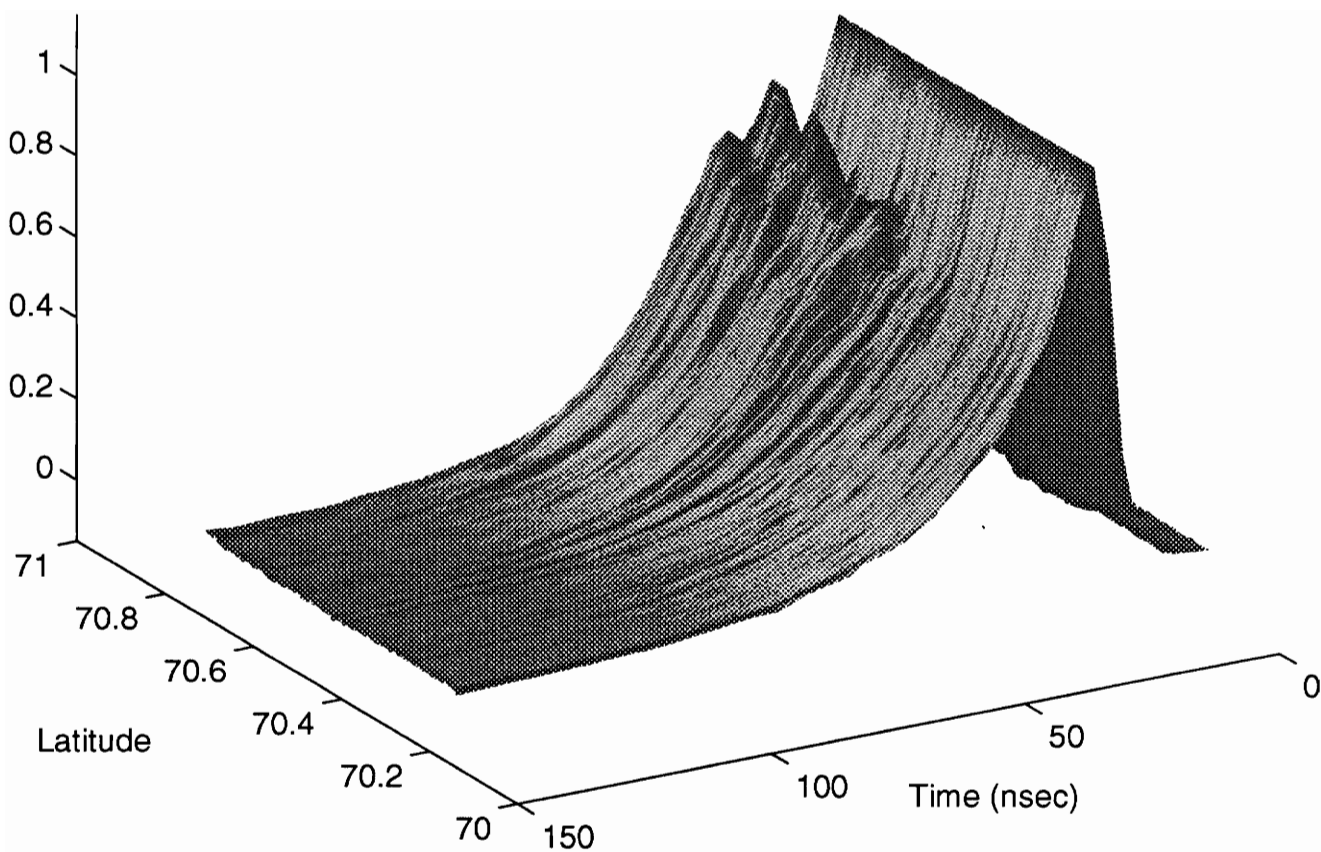


Figure 3.36. AAFE scattered waveforms from 70.16° – 70.74° . Transition from the lower latitudes where surface dominated scattering occurs to the upper latitudes where surface and volume effects are both significant can be seen in the trailing edge of these waveforms.

Also notice that the fit-error for the AAFE system rapidly decreases between 72° – 73° . This indicates that the strong subsurface inhomogeneities present from 70.5° – 72° are not present above 73° . It is for this reason that 73° N latitude is chosen to define the upper boundary of the percolation zone along the flight line.

A similar analysis of the 36 GHz MARA data indicates that the strong subsurface inhomogeneities which cause the homogeneous model to be invalid for the AAFE system from 70.5° – 73° are not seen by the MARA system from 70.5° – 72° along the flight line. This implies that the majority of these subsurface inhomogeneities are below MARA's penetration depth of approximately two meters in this region. It is also interesting to observe that the volume/surface ratio and fit-error for the MARA data set rapidly increases from 72° – 73° while the AAFE fit-error rapidly decreases over the same section of the flight line. The fact that the MARA fit-error is increasing over this region of the flight line indicates that the presence of subsurface inhomogeneities within the upper two meters of the ice sheet is increasing from 72° – 73° . The simultaneous decrease in the AAFE fit-error implies that, although there are inhomogeneous scatterers within the upper few meters of the ice sheet, they do not scatter as strongly at 13.5 GHz as those subsurface scatterers observed by the AAFE system from 70.5° – 72° .

In summary, we see that the primary subsurface scatterers in the percolation zone are located well below the two meter penetration depth of the MARA altimeter from 70.5° – 72° . This information is based on the fact that the AAFE fit-error is large over this region (indicating the invalidity of the homogeneous assumption of the scattering model) while the MARA fit-error is small over this same section of the flight line. From 72° – 73° it appears that the average depth of these nonhomogeneous subsurface scatterers gradually increases to within the upper two meters of the ice sheet. This is apparent from the increasing value of the fit-error for the MARA system over this section of the flight line. Furthermore, the fact that the AAFE fit-error decreases while the MARA system experiences increasing contributions from subsurface scatterers implies that the strength of these scatterers also decreases from 72° – 73° . This may be due, for example, to a decrease in the size and frequency of these subsurface scatterers as a result of the decreasing mean annual temperature with latitude.

Region 4: Dry-Snow Zone ($\sim 73^{\circ}$)

Scattering in the dry-snow zone is expected to be dominated by primarily homogeneous volume scattering effects and should be identifiable from plots of the extinction coefficient, volume/surface ratio and the fit-error. It is expected that in this region of the ice sheet the extinction coefficient and fit-error should both be small and the value of η should be larger than in the lower latitudes. Small deviations from the homogeneous scattering model may result from the known depth dependence of the density of the ice sheet [2].

From the parameter estimates shown in Figures 3.31–3.33 it is apparent that the dry-snow line which divides the percolation and dry-snow zones is not well defined. Rather, the transition from the percolation facies to the dry snow facies along the flight line appears to be a gradual transition occurring between 73° and 75° N latitude. This is in contrast to the boundaries observed above between regions 1 and 2 and region 2 and the percolation zone. However, this is in agreement with observations of an ill-defined boundary between the percolation zone and the dry snow zone previously made by others based on pit studies of the ice sheet [2].

The gradual transition from the percolation facies to the dry-snow facies is also consistent with the observed transition in the percolation zone from 72° – 73° . It appears that the upward migration and decrease in strength of the subsurface scatterers with latitude from 72° – 73° is followed in the dry-snow facies above 73° by a gradual decrease in the strength and number of these subsurface scatterers as suggested in Figure 3.1.

3.4.4 Parameter Estimation: Capabilities and Limitations

The preceding analysis of the parameter estimates derived from the AAFE and MARA data sets provide a unique view of a small portion of the Greenland ice sheet as well as an important part of an assessment of the ability of airborne altimeters to provide useful information on the near surface properties of the ice sheet.

It has been demonstrated that the 36 GHz MARA altimeter is capable of reliably identifying the various facies of the ice sheet while also providing the ability to monitor day-to-day variations in the near surface properties of the ice sheet due to temperature variations. Perhaps most notable is the fact that both AAFE and MARA were able to observe essentially the same locations for the boundaries which separate electromagnetically distinct regions of the ice sheet. This is in spite of the fact that the

two systems operated with significantly different configurations at widely separated frequencies. These results suggest that the altimeter may provide a useful means for monitoring long term variations in the location of these physical boundaries.

The two frequency nature of the September 18 data set has also demonstrated the ability of the altimeter to measure the average locations of subsurface scatterers in the percolation zone of the ice sheet. Application of the nonhomogeneous form of the newly developed scattering model may provide the same information using only a single frequency altimeter. It is also expected that the new model may also be useful in determining the average depth dependent scattering properties in the dry-snow facies of the ice sheet. Such information may be useful in determining the average depth-density and/or depth-particle size distributions. Such an application of the nonhomogeneous form of the scattering model has not yet been investigated and will be the subject of future research.

3.5 Range Estimate Performance

Although the scattering parameters derived from fitting the composite average waveform model to scattering data provides significant information on the surface and subsurface properties of the ice sheet, it is also important that an altimeter be able to reliably determine the surface elevation of the ice sheet. To this end, the elevation estimates determined from the MARA and AAFE systems will be compared to estimates obtained by NASA's AOL laser profilometer. The AOL system is used as a reference because as an optical system it does not experience the same kind of pulse penetration effects as the radars. The AOL pulsewidth is also much narrower than the MARA and AAFE pulsewidths so that it is not necessary to use a scattering model to obtain precise elevation estimates. The rms error in the single-return AOL elevation estimates is approximately 8-10 cm [33]. The MARA and AAFE systems' ranging performances will be dissimilar because of the corresponding frequency and penetration differences.

To prepare for this comparison, the MARA range data must be preprocessed to put it in the proper form for comparison with AOL data. This involves manipulating the range data for each of MARA's beams into a format that can be accepted by existing AOL elevation comparison programs [33]. The AAFE system's performance has previously been evaluated relative to AOL in a similar manner [15], so the three systems will be readily intercomparable.

Having the MARA data in a form compatible with the existing AOL software, the MARA range estimates are first converted into absolute coordinates on the surface of the ice sheet. The elevation of the ice sheet is determined by differencing the MARA derived estimate of the range from the aircraft to the surface with the differential GPS absolute measurement of the height of the aircraft above the geoid. This is expressed analytically as

$$z_{Surf\ Elev} = z_{GPS} - z_{MARA} \quad (3-10)$$

where $z_{Surf\ Elev}$ is the height of the ice sheet above the geoid, z_{GPS} is the height of the aircraft's GPS receiver above the geoid and z_{MARA} is the MARA derived range estimate to the surface. The absolute coordinates (latitude, longitude) of the point on the surface illuminated by the MARA system are determined using right triangle trigonometry and a knowledge of $z_{Surf\ Elev}$, the GPS receiver location and the pointing angle of the appropriate MARA beam. The AOL range-to-surface estimates have been similarly converted to an absolute (latitude, longitude, elevation) format and are archived at NASA's Wallops Flight Facility.

Having both data sets in this form, a direct comparison between the MARA and AOL derived elevation estimates can be obtained. In making such a comparison it is important to recognize that each MARA elevation estimate represents the average of 100 raw range estimates. As discussed in Section 3.2, these 100 raw waveforms correspond to a 100 meter distance along the aircraft's flight line. Since the diameter of the footprint of the three MARA beams under consideration from an altitude of 500 meters is approximately five meters in the *E*-plane and eight meters in the *H*-plane (see Table 3.1), each MARA derived range estimate roughly corresponds to a 8×100 meter section of the ice sheet. The AOL footprint from an altitude of 500 meters is slightly over one meter [33]. The AOL beam was swept in an elliptical pattern along the aircraft's ground track. Thus it is necessary to average all AOL elevation estimates within roughly a 8×100 meter section of ground track defined by the MARA system to obtain the average AOL elevation estimate for comparison with the corresponding MARA derived values. There are approximately 80 AOL range estimates within an 8×100 meter section of the flight track. Thus the noise of the average AOL surface elevation estimates used in the following comparisons is approximately 0.89 cm.

The differences between the AOL and MARA elevation estimates derived in this manner are plotted versus latitude in Figure 3.37 for the forward beam of the MARA system on September 20, 1991. Largely similar differences between MARA and AOL

elevation estimates were obtained for all beams on all the three days considered in this report¹². The differenced data shown in this figure has been centered such that the mean is zero. This has been done because insufficient information is available to determine an absolute elevation estimate from the MARA data. As indicated in the figure, three different surface tracking techniques were used to determine the point on the waveform corresponding to the mean surface location. In the centroid (half-power) tracking method, the centroid (half-power) point on the waveform is taken to correspond to the mean scattering surface. In the model tracking method, the mean scattering surface is determined using the scattering model by first fitting the model to the average scattered waveform as discussed in Section 3.4. The point on the measured waveform corresponding to the mean surface is then determined from the mean surface location of the model waveform.

The standard deviations across the entire flight line for the elevation differences shown in Figure 3.37 are 33.3, 25.8 and 15.8 centimeters for centroid, model and half-power tracked MARA data, respectively. The half-power tracker produces optimal results. In performing a similar analysis of the AAFE system, it has also been determined that the minimum standard deviation between the AAFE and AOL elevation estimates is obtained using a half-power tracking technique. For the AAFE system this yielded a standard deviation across the flight line of 24 centimeters [15].

Given that the forward beam of the MARA system used in this comparison nominally operated at a pointing angle of 12° off-nadir, it is remarkable that the standard deviation of the half-power MARA-AOL elevation estimate is significantly smaller than the similarly derived value for the nadir directed AAFE system. This is attributable to the beamwidth-limited nature of the MARA system, its higher carrier frequency, less penetration, the retracking algorithm used (Section 3.3), and the precision with which the MARA pointing angle was measured. Assuming an altitude of 500 meters and respective nominal pointing angles of 0° and 12°, the range errors due to a 0.05° error in pointing angle measurement for AAFE and MARA are,

$$\begin{aligned} \text{AAFE: } \Delta r &= 500[\sec(0.05^\circ) - \sec(0^\circ)] = 0.00019 \text{ meters} \\ \text{MARA: } \Delta r &= 500[\sec(12.05^\circ) - \sec(12^\circ)] = 0.19 \text{ meters} \end{aligned} \quad (3-11)$$

The range errors resulting from small pointing errors for the MARA system are thus

¹²Slightly larger variations occurred from 69.8°-70.7° on September 18 and from 73.3°-74.5° on September 19. The cause of these isolated cases of anomalous increases in the standard deviation of the elevations estimates has not been determined.

several orders of magnitude larger than the corresponding errors for the AAFE system. This illustrates the necessity of having accurate pointing angle information in order to obtain precise range estimates from an off-nadir altimeter.

Finally, we consider the qualitative aspects of the surface tracking techniques used to obtain the MARA - AOL elevation differences shown in Figure 3.37. It is apparent that the model and half-power tracking techniques shown in the figure do a relatively good job of tracking the mean surface. The centroid tracking method does not track the mean surface, however, and is seen to be highly sensitive to the pulse penetration effects present in the percolation and dry snow zones of the ice sheet.

While the model and half-power tracking technique both track the mean surface reasonably well across the entire flight line, the model derived elevation estimates contain significantly more noise than the half-power tracked estimates. This noise in the model tracked estimates is a result of the noise in the parameter estimates derived in fitting the model to the average MARA scattered waveforms.

In the fitting process, changes in the model parameters directly result in changes in the point on the waveform corresponding to the distance to the mean surface. Thus, scattering phenomena not included in the scattering model (such as those discussed for the percolation zone) cause the parameter estimates to change from the correct values to values which produce a waveform which minimizes the fitting function. This incorrect choice of fitting parameters causes the mean surface location also to be incorrect. This is illustrated in Figure 3.37 where the noise for the elevation estimates derived using the model tracked MARA data is seen to be larger in the upper latitudes where penetration effects are important. The standard deviation of the MARA - AOL differences from 68.7° to 71° is 21 cm while the standard deviation from 71° to 74.6° is 28 cm. Thus, the standard deviation is significantly smaller in the region of the ice sheet where surface scattering effects dominate the contributions to the average scattered waveform.

MARA (forward beam) - AOL elevation estimates

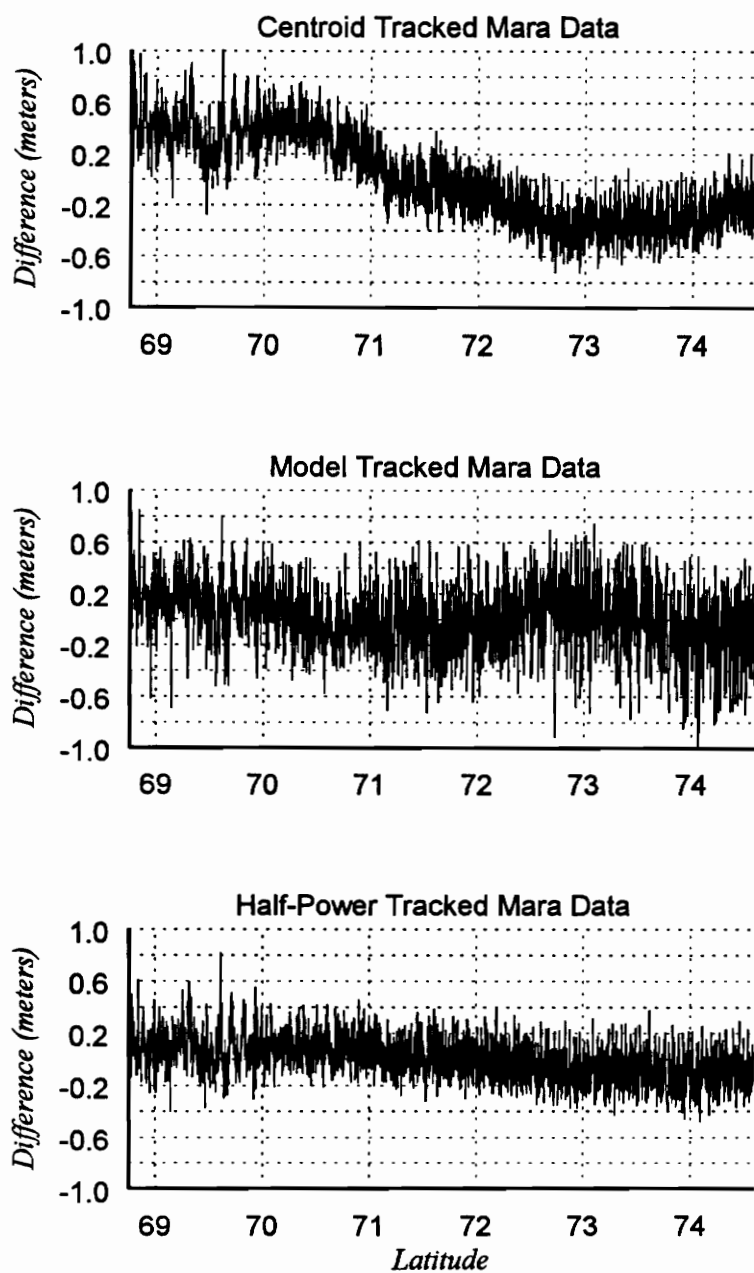


Figure 3.37. Difference between MARA and AOL elevation estimates ($z_{MARA} - z_{AOL}$) along the flight line on September 20, 1991.

Chapter 4

Conclusions

In this report a new incoherent, short pulse volume scattering model was developed from the scalar equation of transfer. The new model extends previous models by incorporating the effects of a rough interface and layering on the volume scattered waveform. Parameter estimates derived by fitting a homogeneous form of the new model to measured scattering data have been shown to differ from those derived using previous models. The model has also been shown to be significantly faster than another comparable model. This is important since it allows for the analysis of large amounts of scattering data in a reasonable amount of time.

A two component scattering model was obtained by combining the new volume scattering model with a previously developed surface model. The composite scattering model has been used to analyze nadir and off-nadir backscattered waveforms recorded by the AAFE and MARA altimeters on a joint mission over a section of the Greenland ice sheet in 1991. The data recorded by the altimeters includes scattering from all four diagenetic facies of the ice sheet: the ablated, soaked, percolation and dry-snow zones.

Estimates of the composite model's parameters σ_h , k_e and η were obtained in all four diagenetic facies of the ice sheet by using a brute-force algorithm to fit the scattering model to average measured waveforms. Analysis of parameter estimates derived from data obtained on September 18, 19 and 20, 1991 by the MARA altimeter has demonstrated the altimeter's ability to accurately determine the boundary between the various diagenetic facies of the ice sheet as well as the strong diurnal and day-to-day repeatability of the altimeter derived parameter estimates. The ability of the altimeter to measure small day-to-day variations in the scattering properties of the ablated and soaked regions of the ice sheet due to temperature changes has also been observed. These results indicate that the MARA system may be useful for monitoring both long and short term changes in the properties of the ice sheet.

The frequency dependence of the composite model's parameters were investigated by comparing AAFE (13.9 GHz) and MARA (36 GHz) derived estimates. A comparison of these parameters demonstrated that both altimeters observe four distinct regions of the ice sheet which correspond to the diagenetic facies defined by others. However, the location of the boundary between the percolation and dry-snow facies was observed to be ill-defined. This observation is consistent with observations made by others in studying the ice sheet. Using the frequency dependence of the MARA and AAFE sensors it was possible to determine the average depth and strength of the nonhomogeneous scatterers throughout the percolation and dry-snow facies.

Finally, the ability of the AAFE and MARA altimeters to accurately measure the surface elevation of the ice sheet has been determined through intercomparison with surface elevation estimates derived from the AOL laser profilometer. The rms error in surface elevation estimates derived from the off-nadir beams of the MARA system are less than 16 cm. This has been seen to exceed the performance of the nadir directed AAFE system.

The ability of the radar altimeter to precisely profile the earth's oceans while simultaneously providing useful information on sea state is well known. In this report it has been demonstrated that the altimeter is also capable of similarly profiling the surface of the Greenland ice sheet while providing information on the surface and *subsurface* properties of the ice sheet.

The ability of the altimeter to obtain precise elevation estimates using off-nadir beams implies that larger coverage of the ice sheet is attainable from aircraft platforms using multibeam altimetry techniques. The altimeter's ability to accurately locate transitions between the various facies of the ice sheet provides a technique useful for monitoring secular climatic changes in the ice sheet [2]. It has also been suggested that, through the use of multifrequency instruments and/or the application of the nonhomogeneous form of the new scattering model developed herein, it should be possible to monitor the location of subsurface scatterers in the percolation and dry-snow regions of the ice sheet. Such information may provide another means of monitoring variations in the climate of the ice sheet.

Chapter 5

References

- [1] Adams, R. J., M. H. Newkirk and G. S. Brown, "Analysis of Multifrequency Radar Altimeter Data from the Greenland Ice Sheet," Report No. EMIL-95-1, ElectroMagnetic Interactions Laboratory, Virginia Polytechnic Institute and State University, Blacksburg, VA, 1995.
- [2] Benson, C. S., *Stratigraphic studies in the snow and firn of the Greenland ice sheet*, U. S. Army Snow Ice and Permafrost Research Establishment (SIPRE), Research Report 70, 1962.
- [3] Born, M. and E. Wolf, *Principles of Optics, Sixth Edition*, Pergamon Press, London, pp. 508-511, 1959.
- [4] Brigham, E. O., *The Fast Fourier Transform*, Prentice-Hall, Englewood Cliffs, NJ, 1974.
- [5] Brown, G. S., "The Average Impulse Response of a Rough Surface and its Applications," *IEEE Trans. Antennas and Propagation*, vol. 25, pp. 67-74, 1977.
- [6] Brown, G. S., "A Useful Approximation for the Flat Surface Impulse Response," *IEEE Trans. Antennas and Propagation*, vol. 37, pp. 764-767, 1989.
- [7] Brown, G. S., "Quasi-Specular Scattering from the Air-Sea Interface," *Surface Waves and Fluxes, Volume 2*, eds. G. L. Geernaert and W. J. Plant, Kluwer Academic Publishers, The Netherlands, 1990.
- [8] Brown, G. S., "Pulse to Pulse Decorrelation for Radar Altimetry Design," EMIL internal document, Bradley Department of Electrical Engineering, Virginia Tech, 1995.
- [9] Davis, C. H., "Satellite Radar Altimetry," *IEEE Trans. Microwave Theory and Techniques*, vol. 40, no. 6, 1992.
- [10] Davis, C. H. and R. K. Moore, "A Combined Surface and Volume Scattering Model for Ice Sheet Radar Altimetry," *J. Glaciology*, vol. 34, pp. 675-818, 1993.

- [11] Davis, C. H., "A surface and volume scattering retracking algorithm for ice sheet satellite retracking," *IEEE Trans. Geosci. Remote Sensing*, vol. 31, pp. 811-818, 1993.
- [12] Davis, C. H. and H. J. Zwally, "Geographic and seasonal variations in the surface properties of the ice sheets by satellite radar altimetry," *J. Glaciology*, vol. 39, pp. 687-697, 1993.
- [13] Davis, C. H. and V. I. Poznyak, "The depth of penetration in Antarctic firm at 10 GHz," *IEEE Trans. Geosci. Remote Sensing*, vol. 31, pp. 1107-1111, 1993.
- [14] Davis, C. H., "Surface elevation change of the Greenland ice sheet from an analysis of Seasat and Geosat altimeter data," *Int. Geosci. Remote Sensing Symposium*, Pasadena, CA, 1994.
- [15] Ferraro, E. J., "Analysis of Airborne Radar Altimetry Measurements of the Greenland Ice Sheet," *Ph.D. Dissertation*, University of Massachusetts at Amherst, MA, 1994.
- [16] Kapp, D. A. and G. S. Brown, "A New Numerical Method for Rough Surface Scattering Calculations," submitted for publication to *IEEE Trans. Antennas and Propagation*, 1995.
- [17] Kodis, R. D., "A note on the theory of scattering from an irregular surface," *IEEE Trans. Antennas and Propagation*, vol. AP-14, no. 1, pp. 77-82, 1966.
- [18] Le Vine, D. M., R. H. Lang and Y. Lin, "Transient response of a layer of discrete random media over a dielectric half space," *IEEE Trans. Geosci. Remote Sensing*, vol. 30, no. 5, pp. 1034-1045, 1992.
- [19] Marth, P., J. Jenson, C. Kilgus, J. Perschy, J. MacArthur, D. Hancock, G. Hayne, C. Purdy, L. Rossi and C. Koblinsky, "Prelaunch Performance of the NASA Altimeter for the TOPEX/POSEIDON Project," *IEEE Trans. Geoscience and Remote Sensing*, vol. 31, pp. 315-331, 1993.
- [20] McGoogan, J. T., L. S. Miller, G. S. Brown and G. S. Hayne, "The S-193 Radar Altimeter," *Proceedings of the IEEE*, vol. 62, no. 6, pp. 793-803, 1974.
- [21] Newkirk, M. H. and G. S. Brown, "Issues Related to Waveform Computations for Radar Altimeter Applications," *IEEE Trans. Antennas and Propagation*, vol. 40, pp. 1478-1488, 1992.

- [22] Newkirk, M. H., *An Altimeter Waveform Model for Combined Surface and Volume Scattering*, Ph.D. dissertation, Virginia Polytechnic Institute and State University, Blacksburg, VA, 1994.
- [23] Newkirk, M. H. and G. S. Brown, "A Waveform Model for Surface and Volume Scattering from Ice and Snow," in press, *IEEE Trans. Geoscience and Remote Sensing*, 1995
- [24] Parsons, C. L., ed., *MARA System Documentation, Volume I - MARA System Requirements Document*, NASA Reference Publication 1226, 1989.
- [25] Partington, K. C., W. Cudlip and G. C. Rapley, "An assessment of the capability of the satellite radar altimeter for measuring ice sheet topographic change," *Int. J. Remote Sensing*, vol. 12, pp. 585-609, 1991.
- [26] Ridley, J. K. and K. C. Partington, "A Model of Satellite Radar Altimeter Returns from Ice Sheets," *Int. J. Remote Sensing*, vol. 9, pp. 601-624, 1988.
- [27] Thomas, G. B., and R. L. Finney, *Calculus and Analytic Geometry*, Addison-Wesley, Reading, MA, 1988.
- [28] Thomas, R. H., R. A. Bindshadler, R. L. Cameron, F. D. Carsey, B. Holt, T. J. Hughes, C. W. M. Swithinbank, I. M. Whillans, H. J. Zwally, "Satellite remote sensing for ice sheet research," *NASA Technical Memorandum 86233*, 1985.
- [29] Tsang, L., J. Kong and R. T. Shin, *Theory of Microwave Remote Sensing*, John Wiley & Sons, New York, 1985.
- [30] Ulaby, F. T., R. K. Moore and A. K. Fung, *Microwave Remote Sensing - Active and Passive, Vols. I-III*, Addison-Wesley, Reading, MA, 1982.
- [31] Ulaby, F. T., T. F. Haddock, R. T. Austin and Y. Kuga, "Millimeter-wave radar scattering from snow; 1. Radiative transfer model," *Radio Science*, vol. 26, pp. 329-341, 1991.
- [32] Ulaby, F. T., T. F. Haddock, R. T. Austin and Y. Kuga, "Millimeter-wave radar scattering from snow; 2. Comparison of theory with experimental observations," *Radio Science*, vol. 26, pp. 343-351, 1991.
- [33] Vandemark, D. C., Private Communications, 1995.
- [34] Walsh, E. J., "Analysis of experimental NRL radar altimeter data," *Radio Science*, vol. 9, nos. 8&9, pp. 711-722, 1974.
- [35] Zwally, H. J. "Growth of the Greenland ice sheet: interpretation," *Science*, no. 246, pp. 1589-1591, 1989.

Appendix A

Scattering Model Assumptions

In developing an analytical expression for the volume scattered waveform from the scalar equation of transfer, it was necessary to approximate the scattering source term J_s given by equation (2-14)

$$J_s(\hat{\mathbf{r}}; r, \theta, \phi, t) = \frac{k_s(r, \theta, \phi)}{4\pi} \int \int_{4\pi} \psi(\hat{\mathbf{r}}, \hat{\mathbf{r}}_i; r, \theta, \phi, t) I(\hat{\mathbf{r}}_i; r, \theta, \phi, t) d\Omega_i \quad (2-14)$$

When considering the downwelling intensity the approximation (2-17) was made,

$$J_s(\hat{\mathbf{r}}; r, \theta, \phi, t) \approx \sigma_f(r, \theta, \phi) I(\hat{\mathbf{r}}; r, \theta, \phi, t) \quad (2-17)$$

Similarly, the equation for the upwelling intensity was solved using the approximation (2-23),

$$J_s(-\hat{\mathbf{r}}; r, \theta, \phi, t) \approx \sigma_f(r, \theta, \phi) I(-\hat{\mathbf{r}}; r, \theta, \phi, t) + \sigma_b(r, \theta, \phi) I(\hat{\mathbf{r}}; r, \theta, \phi, t) \quad (2-23)$$

The assumptions inherent to these two equations are similar. However, they differ depending on the type of medium being considered. The cases of sparse and dense media are addressed below to illustrate these differences.

Sparse Media

In the case of a sparse medium (i.e., a medium in which the volume fraction of particles is small) the effects of multiple interactions between particles is small and the average particle separation is large. This allows the far-field form of the scattering phase function, ψ_{ff} , to be used in equation (2-14),

$$\psi(\hat{\mathbf{r}}, \hat{\mathbf{r}}_i; r, \theta, \phi, t) \Rightarrow \psi_{ff}(\hat{\mathbf{r}}, \hat{\mathbf{r}}_i; r, \theta, \phi, t) \quad (A-1)$$

Furthermore, the incident intensity dominates the contributions to the integral in (2-14). Thus,

$$\begin{aligned} J_s(\hat{\mathbf{r}}; r, \theta, \phi, t) &\approx \frac{k_s(r, \theta, \phi)}{4\pi} \psi_{ff}(\hat{\mathbf{r}}, \hat{\mathbf{r}}; r, \theta, \phi, t) I(\hat{\mathbf{r}}; r, \theta, \phi, t) \\ &\equiv \sigma_f(r, \theta, \phi) I(\hat{\mathbf{r}}; r, \theta, \phi, t) \end{aligned} \quad (A-2)$$

where $I(\hat{\mathbf{r}})$ has been assumed to be δ -distributed with respect to incidence angle at the point (r, θ, ϕ) in the medium.

A form of the approximation (2-23) is similarly obtained in the case of sparse media by recognizing that the dominant contribution to the scattering source term in the upwelling direction, $J_s(-\hat{r})$, arises from backscattering of the downwelling intensity at the point (r, θ, ϕ) ,

$$\begin{aligned} J_s(\hat{r}; r, \theta, \phi, t) &\approx \frac{k_s(r, \theta, \phi)}{4\pi} \psi_{ff}(-\hat{r}, \hat{r}; r, \theta, \phi, t) I(\hat{r}; r, \theta, \phi, t) \\ &= \sigma_b(r, \theta, \phi) I(\hat{r}; r, \theta, \phi, t) \end{aligned} \quad (\text{A-3})$$

The term resulting from forward scattering of the upwelling intensity which is present in (2-23), $\sigma_f I(-\hat{r})$, has been neglected here since this is a multiple scattering effect and, in the case of a sparse medium, will be small compared to backscattering of the downwelling intensity. Thus, for a sparse medium of small particles we have

$$\begin{aligned} \sigma_f(r, \theta, \phi) &\equiv \frac{k_s(r, \theta, \phi)}{4\pi} \psi_{ff}(\hat{r}, \hat{r}; r, \theta, \phi, t) \\ \sigma_b(r, \theta, \phi) &\equiv \frac{k_s(r, \theta, \phi)}{4\pi} \psi_{ff}(-\hat{r}, \hat{r}; r, \theta, \phi, t) \end{aligned} \quad (\text{A-4})$$

Provided that the medium is simple enough (e.g., spherical scatterers) the model parameters in this equation can be related to physical quantities.

Dense Media

In the case of sparse media, the approximations (2-17) and (2-23) make good physical sense and the parameters derived from these approximations to the scattering source term can be related to physical quantities through ψ_{ff} and k_s . However, the extension of these approximations to the case of dense media raises questions as to their validity and their physical meaning.

Considering equation (2-16) for the downwelling intensity, it is clear that the approximation (2-17) for the scattering source term $J_s(+\hat{r})$ cannot be justified in the same manner in which it was for sparse media. This is because, for dense media, it is not clear that the dominant contribution to the integral in equation (2-14) for $J_s(+\hat{r})$ is dominated by contributions from the $+\hat{r}$ direction except perhaps at points very near the free-space/scattering-medium interface.

To obtain a better understanding of the approximation (2-17) in this case, consider the steady state form of this equation. Since J_s and I are time-independent in this case, the approximation (2-17) becomes exact for some σ_f ,

$$J_s(\hat{r}; r, \theta, \phi) = \sigma_f(r, \theta, \phi) I(\hat{r}; r, \theta, \phi) \quad (\text{A-5})$$

In the case of an incident *pulse* the functions J_s and I are time varying. To obtain an expression similar to (A-5) for the time-dependent problem under consideration, σ_f must also be time varying,

$$\sigma_f(r, \theta, \phi, t) = \frac{J_s(\hat{r}; r, \theta, \phi, t)}{I(\hat{r}; r, \theta, \phi, t)} \quad (\text{A-6})$$

Thus, in using (2-17) where σ_f is taken to be time-independent for the time varying problem, an approximation has been made which results from the finite width of the incident pulse. This implies that only short range (on the scale of the incident pulsewidth) multiple scattering effects are included in (2-17). As the pulsewidth becomes larger the approximation improves, becoming exact in the steady state limit. The types of scattering not included in this approximation are those interactions which occur over large distances (on the scale of the pulsewidth) as illustrated in Figure A.1. These long range interactions can cause σ_f to vary significantly with time.

The scattering effects included in the approximation (2-23) for the case of dense media include those effects just discussed for (2-17) plus an additional component due to backscattering of the downwelling intensity ($\sigma_f I(-\hat{r})$). It is necessary to retain both of these terms in approximating the scattering source term in the upwelling direction because the upwelling and downwelling intensities at a point in the medium are not necessarily proportional due to the finite width of the incident pulse.

Although (2-17) and (2-23) have been used to approximate the scattering source term in the cases of both sparse and dense media, it is important to note the significantly different meanings of σ_f and σ_b for the two cases. As mentioned above for the sparse medium case, these parameters can be directly related to the average physical properties of the medium. This is useful in that it allows the values of σ_f and σ_b derived from a parameter estimation study to be easily related to the physical properties of the scattering medium. In the case of dense media, however, σ_f and σ_b are effective quantities and it is very difficult to relate these to the physical properties of the scattering medium.

It is also interesting to note that the approximations made to obtain the upwelling intensity at the free-space/medium interface are analogous to those used by others to obtain an approximate solution to the magnetic field integral equation [16]. That is, the model first obtains the downwelling intensity by accounting for the cumulative effects of forward scattering (which includes localized multiple scattering effects). This

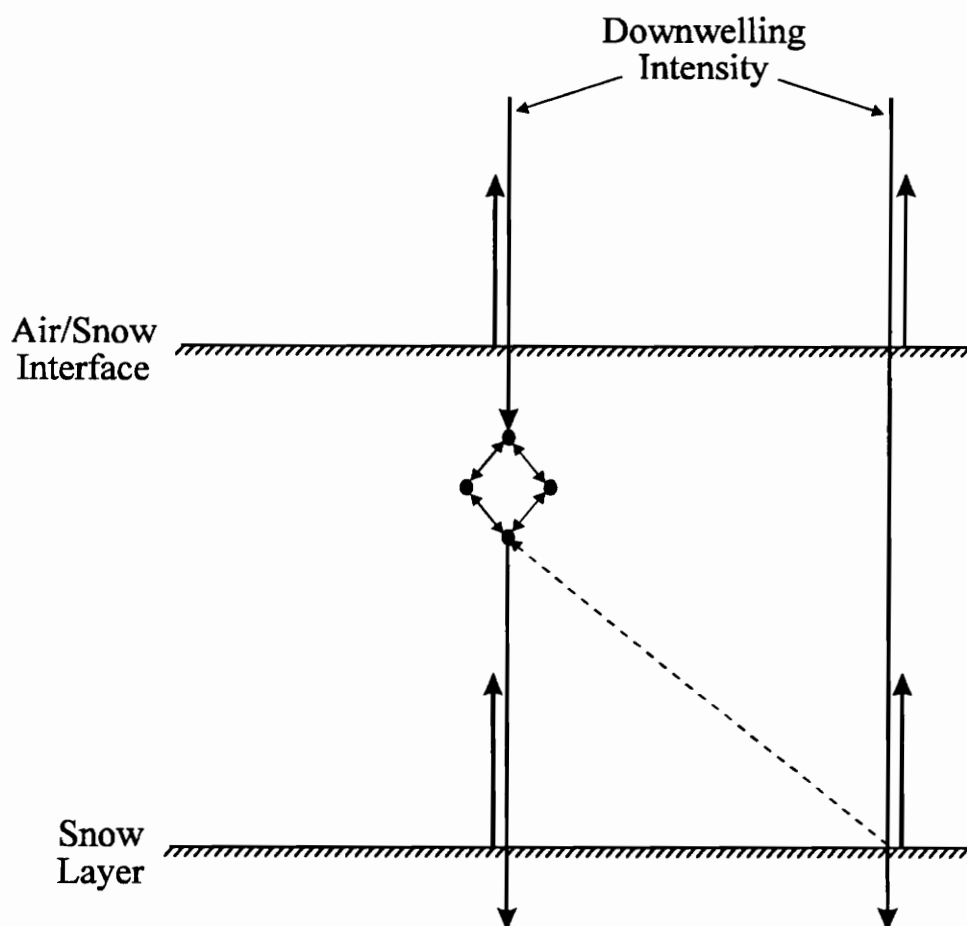


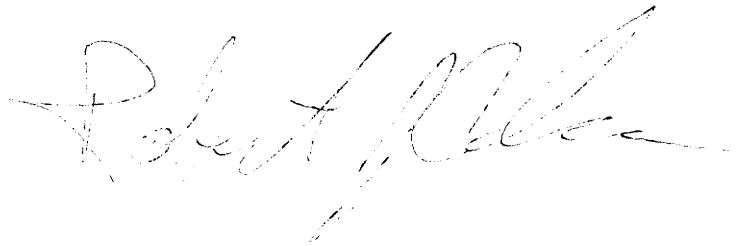
Figure A.1. Those scattering effects which are included in the new model discussed in this report are indicated by solid lines (the small circular scatterers are assumed to be close to one another on the scale of a pulsewidth). An illustration of the type of long range scattering not included in the new model is indicated by the dashed line.

downwelling intensity is next used as a source for the upwelling intensity through the effective backscattering coefficient σ_b . The upwelling intensity at the free-space/medium interface is finally determined by allowing this upwelling intensity to forward scatter back to the surface. Thus the model accounts for forward scattering of the incident intensity to a point in the scattering volume, one order of interaction between the downwelling and upwelling intensities, and forward scattering of the upwelling intensity back to the surface. A more complete model would incorporate *all* orders of interaction. However, losses in the medium may cause such interactions to quickly die out.

Vita

Robert John Adams was born August 21, 1970 in Green Bay, Wisconsin. He graduated from Green Bay's Preble High School in May of 1988. Rob was awarded a Bachelor of Science in Electrical Engineering from the Michigan Technological University in May of 1993. He began graduate work in August of 1993 at the Virginia Polytechnic Institute and State University and began working for Dr. Gary S. Brown in the ElectroMagnetic Interactions Laboratory at Virginia Tech in January of 1994.

Upon fulfillment of the requirements for the Master of Science Degree in Electrical Engineering Rob intends to pursue the Doctor of Philosophy Degree in Electrical Engineering at Virginia Tech and has research interests in the areas of electromagnetic theory, propagation and scattering. His education will be supported by the Bradley Fellowship.

A handwritten signature in cursive script, appearing to read "Robert Adams", written in dark ink.